SYMMETRY-GUIDED DESIGN OF ADVANCED POROUS MATERIALS WITH ANTICIPATED POROSITIES AND FUNCTIONALITIES

A Dissertation

by

MUWEI ZHANG

Submitted to the Office of Graduate and Professional Studies of
Texas A&M University
in partial fulfillment of the requirements for the degree of

DOCTOR OF PHILOSOPHY

Chair of Committee,	Hong-Cai Zhou
Committee Members,	Abraham Clearfield
	David P. Barondeau
	Perla B. Balbuena
Head of Department,	David H. Russell

December 2014

Major Subject: Chemistry

ABSTRACT

For the past few decades, advanced porous materials (APMs) have attracted a tremendous amount of attention due to their fascinating structures and diverse applications. Metal-organic frameworks (MOFs), metal-organic polyhedra (MOPs) and porous polymer networks (PPNs) are important categories of APMs. By unravelling their structure-property relationships and employing the principles of group theory and topochemistry, this dissertation will focus on the rational design of these APMs with anticipated structures, porosities and properties. The vast majority of this dissertation will rely on the utilization of the tetrahedral building blocks in the construction of MOFs and PPNs. A few representative examples of MOMs with biomimetic features will also be presented.

The first part of this dissertation introduces background knowledge for the chemistry of APMs. In addition to their definition and potential applications, it provides a systematic overview of different methods for the rational design of APMs.

The second part illustrates the structures and gas storage applications of a series of MOFs constructed from a synthetically-accessible tetrahedral ligand.

The study of symmetry-guided design of MOFs includes further exploration of tetrahedral ligands. The third part elucidates how the employment of topochemistry can lead to the discovery of a MOF with the largest porosity among all MOFs made from tetrahedral linkers.

The symmetry-guided strategy can also be applied to the synthesis of PPNs. The fourth part describes the rational design, preparation and characterization of a commercially affordable PPN for highly efficient CO_2 capture.

Tetrahedral building units are also highly attractive for constructing mixed-ligand MOFs. In the next part is a close examination of the symmetry elements in Bravais lattices seen in MOFs, which has led to the discovery of a series of highly porous mixed-ligand MOFs.

The sixth part discusses the design and synthesis two nucleobase-incorporated MOMs. It also briefly covers the rational design of MOMs with biomimetic features.

In summary, a wide variety of APMs with anticipated structures and properties are rationally designed, based on a close examination of the symmetry elements of their basic building blocks. This work also offers a general perspective on the rational design of APMs with desired porosities and functionalities.

DEDICATION

This work is dedicated to my beloved family for their love and constant support.

ACKNOWLEDGEMENTS

First, I would like to take this opportunity to express my deepest gratitude to my research advisor, Prof. Hong-Cai Zhou, for his guidance, patience and encouragement throughout the past five years. He has been a great mentor not only for my research, but also for my life. I believe the knowledge, skills, insights, and characteristics that I have developed under his guidance will greatly benefit me over my future career and entire life. I am exceptionally grateful for his insightful guidance and generous support.

I would like to thank my committee members, Prof. Clearfield, Prof. Barondeau and Prof. Balbuena, for their guidance and patience throughout my research. The courses taught by Prof. Clearfield and Prof. Barondeau have illuminated the principles of crystallography and bioinorganic chemistry, which have played a significant role in my subsequent research. Prof. Balbuena's research has provided some insightful ideas for my ensuing work on CO_2 capture. In addition, Prof. Clearfield has provided me some valuable suggestions and generous help in my job searching process. I feel extremely grateful to my committee members for their support.

I am thankful to all the group members. I would like to express my special appreciation to Ms. Ying-Pin Chen and Mr. Mathieu Bosch, for their valuable collaboration and precious friendship. My thanks are also extended to everyone with whom I have collaborated, including Dr. Jian-Rong Li, Dr. Daqiang Yuan, Dr. Dan Zhao, Dr. Zhi-Yuan Gu, Dr. Weigang Lu, Dr. Jinhee Park, Dr. Dahuan Liu, Dr. Tian-Fu Liu,

Mr. Thomas Gentle III, Mr. Zachary Perry, Mr. Stephen A. Fordham, Ms. Lanfang Zou and Ms. Hao Li.

I would also like to extend my gratitude to all my friends, colleagues, and the department faculty and staff, for making my time at Texas A&M University a valuable and enjoyable experience.

Finally, my family deserves my greatest appreciation. My parents have provided their unselfish love, support and patience for the past 26 years. This is the ultimate motivation for me to strive for success.

NOMENCLATURE

APM	Advanced Porous Material
BET	Brunauer–Emmett–Teller (surface area)
CCDC	Cambridge Crystallographic Data Centre
CCP	Cubic Close Packing
CCS	Carbon Capture and Sequestration
COF	Covalent Organic Framework
DFT	Density Functional Theory
FTIR	Fourier Transform Infrared Spectroscopy
IAST	Ideal Adsorbed Solution Theory (selectivity)
IUPAC	International Union of Pure and Applied Chemistry
MOF	Metal-Organic Framework
MOM	Metal-Organic Material
MOP	Metal-Organic Polyhedron
NMR	Nuclear Magnetic Resonance
PCN	Porous Coordination Network
PCP	Porous Coordination Polymer
POP	Porous Organic Polymer
PPN	Porous Polymer Network
PSM	Post-Synthetic Modification
PXRD	Powder X-ray Diffraction

RCSR	Reticular Chemistry Structure Resource
SBU	Secondary Building Unit
TGA	Thermogravimetric analysis
TMOP	Thymine-incorporated Metal-Organic Polyhedron
UMC	Unsaturated Metal Center
XRD	X-ray Diffraction

Abbreviations of Selected Chemicals

ATC	1,3,5,7-Adamantane tetracarboxylate
BDC	1,4-Benzenedicarboxylate
BPDC	Biphenyl-4,4'-dicarboxylate
BDA	1,4-Benzenediacrylate
DEF	*N*,*N*-Diethylformamide
DMA	*N*,*N*-Dimethylacetamide
DME	Dimethoxyethane
DMF	*N*,*N*-Dimethylformamide
DMSO	Dimethyl sulfoxide
MDPI	5-((5-methyl-2,4-dioxo-3,4-dihydropyrimidin-1(2H)-yl) methyl)isophthalate
MEA	Monoethanolamine
MTBA	Methanetetra(4-benzoate)
MTBC	4',4'',4''',4''''-Methanetetrayltetrabiphenyl-4-carboxylate

NDC	Naphthalenedicarboxylate
$Ni(cod)_2$	Bis(cyclooctadiene)nickel
NMP	*N*-Methyl-2-pyrrolidone
$Pd(PPh_3)_4$	Tetrakis(triphenylphosphine)palladium(0)
TATB	4,4',4''-s-triazine-2,4,6-triyl-tribenzte
TCPS	4,4',4'',4'''-Tetrakiscarboxyphenylsilane
THF	Tetrahydrofuran
TTPM	Tetrakis(4-tetrazolylphenyl)methane

TABLE OF CONTENTS

Page

LIST OF FIGURES

FIGURE Page

FIGURE Page

FIGURE Page

LIST OF SCHEMES

LIST OF TABLES

CHAPTER I

INTRODUCTION TO ADVANCED POROUS MATERIALS: DEFINITION, APPLICATION AND RATIONAL DESIGN [*†]

For the past few decades, porous materials have been extensively investigated in scientific and technological research due to their capability to adsorb and interact with atoms, ions and molecules throughout the bulk of the material. [1] In particular, the study of advanced porous materials (APMs), including metal-organic materials (MOMs) [2, 3] and porous organic polymers (POPs) [4, 5], has been one of the most rapidly developing areas across chemical science. MOMs are an emerging category of porous materials that typically exist as polymeric or discrete supramolecular coordination assemblies that consist of both metal-containing units and organic linkers. POPs, on the other hand, are highly crosslinked organic polymers that typically possess enhanced stability but reduced crystallinity compared to MOMs. Different from the traditional porous materials (such as carbon-based materials [6], porous silica [7, 8] or zeolites [9, 10]), these novel materials offer a vast diversity of chemical architectures that generally possess significantly enlarged porosities and chemically modifiable structures. The majority of this dissertation will be focused on the rational design, preparation, characterization and

[*] Reproduced in part with permission from "Rational Design of Metal-Organic Frameworks with Anticipated Porosities and Functionalities", by Zhang, M.; Bosch, M.; Gentle, T.; Zhou, H.-C., *CrystEngComm*, **2014**, *16*, 4069-4083, copyright 2014 by Royal Society of Chemistry.

[†] Reproduced in part with permission from "Tuning the Structure and Function of Metal–Organic Frameworks via Linker Design", by Lu, W.; Wei, Z.; Gu, Z.-Y.; Liu, T.-F.; Park, J.; Park, J.; Tian, J.; Zhang, M.; Zhang, Q.; Gentle, T.; Bosch, M.; Zhou, H.-C.; *Chem. Soc. Rev.*, **2014**, *43*, 5561-5593, copyright 2014 by Royal Society of Chemistry.

applications of metal-organic frameworks (MOFs), along with some selected examples of metal-organic polyhedra (MOPs) and porous polymer networks (PPNs).

1.1 Metal-Organic Frameworks (MOFs): Definition, Applications and Rational Design

Metal-organic frameworks (MOFs), also known as porous coordination polymers (PCPs), are an important category of crystalline materials that exist as well-defined supramolecular architectures, in which the metal-containing units (also known as secondary building units, or SBUs) are coordinatively connected by ditopic or polytopic organic linkers to form a variety of infinite three dimensional networks. [11-13] Provided that the organic linkers possess a certain degree of rigidity, the resulting framework usually exhibits a permanent inner porosity (*i.e.* pores remain intact and accessible to guest molecules) upon the removal of the guest molecules in its pores. Figure I-1 illustrates two representative MOF examples, MOF-5 [14] and HKUST-1 [15] (HKUST represents "Hong Kong University of Science and Technology"), two of the earliest MOFs to be structurally characterized. For example, in MOF-5, its metal clusters (Zn_4O SBUs) connect with six carboxylates to form an octahedral unit. The rigid organic linker, 1, 4-benzenedicarboxylate (**BDC**), in combination with the SBU, generates large three-dimensional channels inside its structure, providing a channel with diameter of 8.0 Å. It is this potential inner porosity of the frameworks that provides a great variety of applications for MOFs. As a novel category of solid adsorbents, MOFs have overshadowed many traditional porous materials due to their chemically tunable

structures, extraordinarily large porosity and convenient functionalization procedures. MOFs are promising materials for many different applications, such as gas storage [16-18] and separation [19-21], carbon dioxide sequestration [22-24], environmental conservation [25, 26], heterogeneous catalysis [27, 28], enzyme immobilization [29, 30], luminescent materials [31, 32], magnetic materials [33], biomedical materials [34, 35] and others.

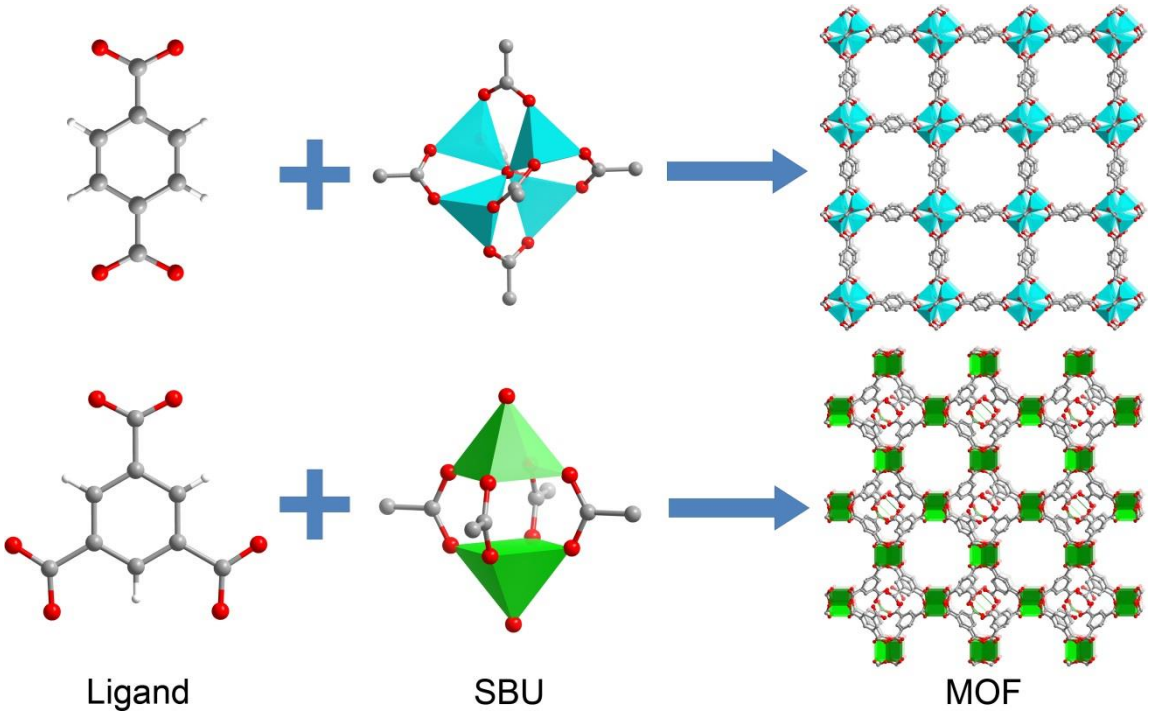

Figure I-1. A graphic illustration of the definition, components and porosity of metal-organic frameworks. Top: the structure of MOF-5 [14]; bottom: the structure of HKUST-1 [15]. (Color Scheme: C, gray; O, red; H, white; Zn, cyan; and Cu, green.)

In the past two decades, the exploration of MOFs has been one of the most rapidly developing areas in chemical science. Since the discovery of several early

examples of representative MOF compounds, more than 20,000 MOF structures were reported and studied to date. [36] Due to the extraordinarily large extent of variability of both metal-containing units and organic linkers, it appears that an inexhaustible amount of MOFs could theoretically be designed and synthesized. This, on the other hand, makes it more difficult for researchers to search for a rational way to design a framework with the properties exactly suitable for a specific use. In fact, the construction of highly-ordered porous materials with desirable porosities and functionalities and predictable properties has been a highly challenging yet stimulating task for chemists. [37] Since the emergence of MOFs, targeted syntheses of MOFs with desired framework cavities and customized framework functionalities have been a challenging problem. [38-40] It is highly desirable to rationally design a novel MOF whose properties can be predicted from its basic constructional units before the framework is synthesized.

The purpose of rational design of MOFs is to achieve accurate control of framework porosity and functionality from the molecular level for a customized interaction between the framework and its guest molecules. Though it is challenging, chemists have been searching for solutions to overcome the difficulties. Thanks to the tunable nature and convenient functionalization processes of MOFs, chemists have been looking for solutions to achieve this goal. Reticular synthesis [41, 42], introduced by the Yaghi and O'Keeffe groups, is a method in which, based on an existing MOF structure, the combination of an elongated organic linker with the same metal-containing secondary building units (SBUs) will possibly result in an isoreticular framework with the same topology but larger pore size. Designing ligands [43-45] with various geometries

and functional groups has enabled us to tentatively control the topology and functionality of the resulting framework. Post-synthetic modifications (PSMs) [46, 47] of MOFs, on the other hand, have assisted us in introducing desired functional groups into the framework in a convenient way. Symmetry-guided design [48], a more recent work from our group, suggests that the scrutiny of simple mineral structures can lead to the design and synthesis of significantly porous frameworks with desired topology and cavity size. In consideration of the rapidly growing research on this topic in the past few years, a highlight review on the recent progress of rational MOF design was published. [49]

It is widely accepted that MOFs are renowned for both their variety of captivating structures and their widespread potential applications. [11, 36] Herein, we would like to categorize the recent advances of rational MOF design into two different approaches: a structural approach and a functional approach. The structural approach includes the rational design of MOFs with expected structures, topologies and porosities, while the functional approach involves the rational design of MOFs with desired functionalities for a particular application. (Scheme I-1) This dissertation will primarily be focused on the symmetry-guided design of MOFs, which typically involves a judicious selection of metal building units and organic ligands that are symmetrically complementary to each other for the purpose of forming a three dimensional network with desired porosity, topology and properties.

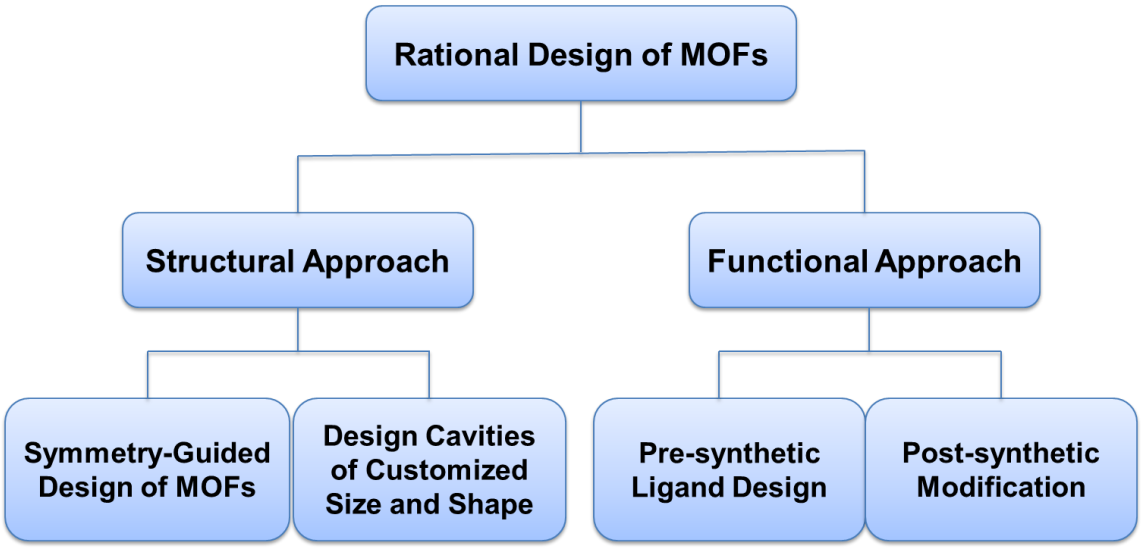

Scheme I-1. Recent efforts of rational design of MOFs can be categorized into two different catalogs: a structural approach and a functional approach. This dissertation will primarily be focused on the symmetry-guided design of MOFs. (Reprinted with permission from Ref. 49, copyright 2014 Royal Chemical Society)

Even though the composition of MOFs appears to be simple, that is, the organic linkers and metal-containing clusters (or SBUs), it is still rather difficult to accurately predict the structure, porosity, and topology of the resulting framework with a given organic linker and metal source. First, the organic ligands can adopt many different conformations, which, upon incorporation into the framework, will result in polymorphic MOFs with completely different structures and properties. [50, 51] Second, the metal ions can form different metal clusters, which will result in different MOF structures as well. [52, 53] Third, when an elongated ligand is utilized, the resulting MOF will, in many cases, suffer from undesirable and unpredictable framework interpenetration. [41, 54] It is still

quite problematic to control the framework interpenetration simply by tuning the solvothermal reaction conditions. [55-57] These limitations made it rather challenging to design MOFs with cavities that possess a desired size, shape, and function.

The introduction of framework topology has brought novel insights to the rational design of highly porous MOFs. [48] Based on a given topology, it is easy for one to tell many important properties of a framework, such as the connectivity of its nodes, the shape and potential size of its cavities, and the possibility of this framework to endure self-interpenetration. [58-61] Previous efforts on MOF topochemistry typically rely on the analysis of framework topology after the MOF structure was resolved. However, the symmetry-guided design implies it is possible to achieve a bottom-up design with desired network connectivity and topology prior to the construction of MOFs. [48] A series of highly porous MOFs with fluorite (**flu**) topology were constructed through the symmetry-guided synthesis strategy, and this work will be elaborated upon in Chapter III.

1.2 Symmetry-Guided Design of MOFs with Tetrahedral Ligands

By unravelling their structure-property relationships and employing the principles of group theory and topological chemistry, the majority of this dissertation relies on the rational design of MOFs with anticipated structures, porosities and topologies. Ligands with tetrahedral geometry are especially intriguing for MOF construction for several reasons. [45] First, a tetrahedral linker has a full T_d symmetry, which is, by far, the highest symmetry in a linker that has been achieved through organic synthesis. High-symmetry building units are always preferred in MOF construction, as

they facilitate the packing process of repetitive units during the assembly of crystalline materials.[43, 44] Second, a tetrahedral linker may adopt the symmetry of any T_d subgroups and generate diversity in MOF structures. (Figure I-2) Third, tetrahedral linkers are inherently three-dimensional, fully-extended struts for MOF construction. Once incorporated into a framework, wide channels and large pores will be provided to maximize the exposure of the framework struts and eliminate the "dead space". In other words, MOFs with exceptionally large porosities could be constructed with tetrahedral building units and symmetrically compatible SBUs.

In general, tetrahedral linkers are still relatively less explored in contrast with linear and tritopic ones possibly due to the challenges in organic synthesis. MOFs with rigid tetrahedral building units have already been explored by Yaghi [62, 63], Lin [64-67], Long [68], Schroder [69], Kim [70], Suh [71], Shimizu [72], Davies [73-76], Lambert [77, 78] and some other research groups [79-81]; however, many of the MOFs suffer from complicated ligand synthesis [67, 69], limited porosity [63, 70] and undesired interpenetration [65, 66].

A limited number of net topologies are associated with MOFs assembled from tetrahedral linkers. Among them, the topology of fluorite (**flu**), platinum sulfide (**pts**) and **alb/P** are the most prominent examples of the topologies with potential for high porosity. A graphic representation of these topologies is illustrated in Figure I-3. In particular, the **flu** topology represents a network that combines 4-connected tetrahedral linkers and 8-connected cubical SBUs in a 2:1 ratio. Similarly, the **pts** topology is the default topology that combines 4-connected tetrahedral linkers and 4-connected square

planar SBUs. The **alb/P** topology combines 4-connected tetrahedral linkers and 8-connected hexagonal bipyramidal SBUs.

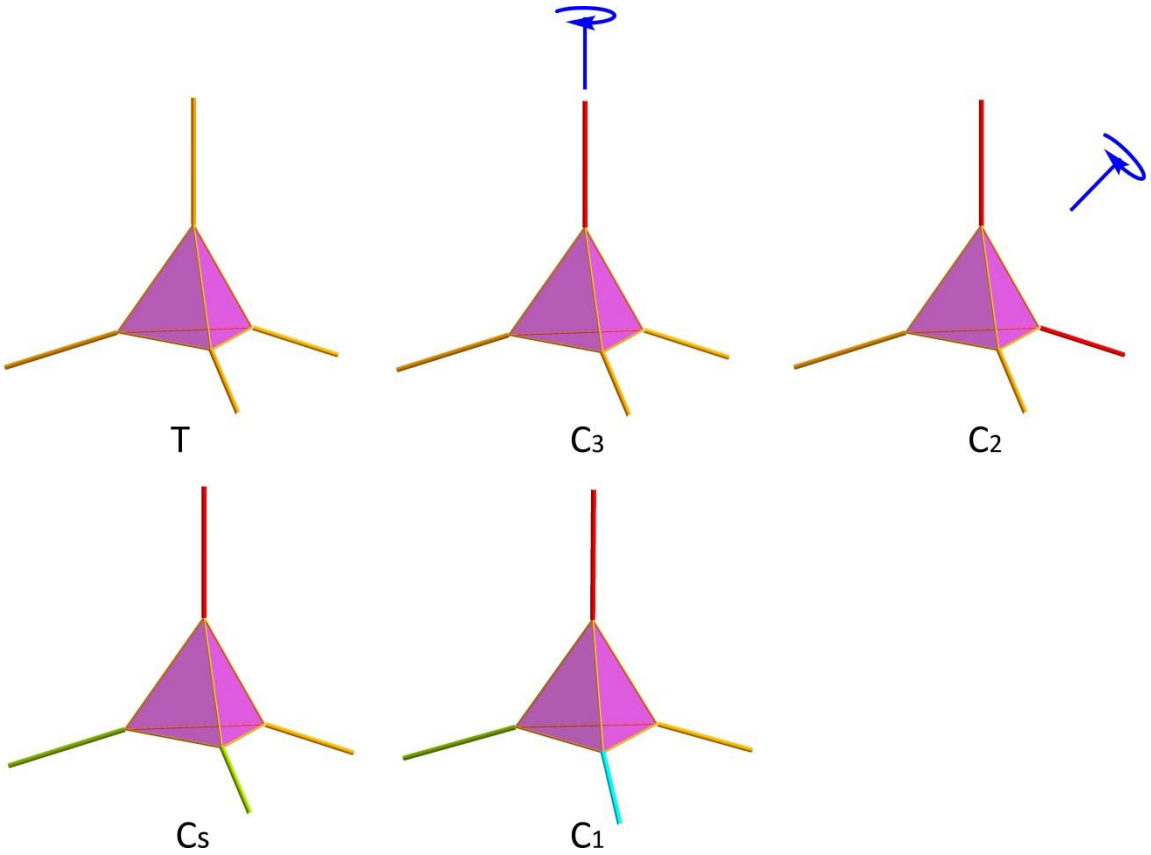

Figure I-2. Symmetry elements of a full T_d symmetry; different colors represent different coordination environments.

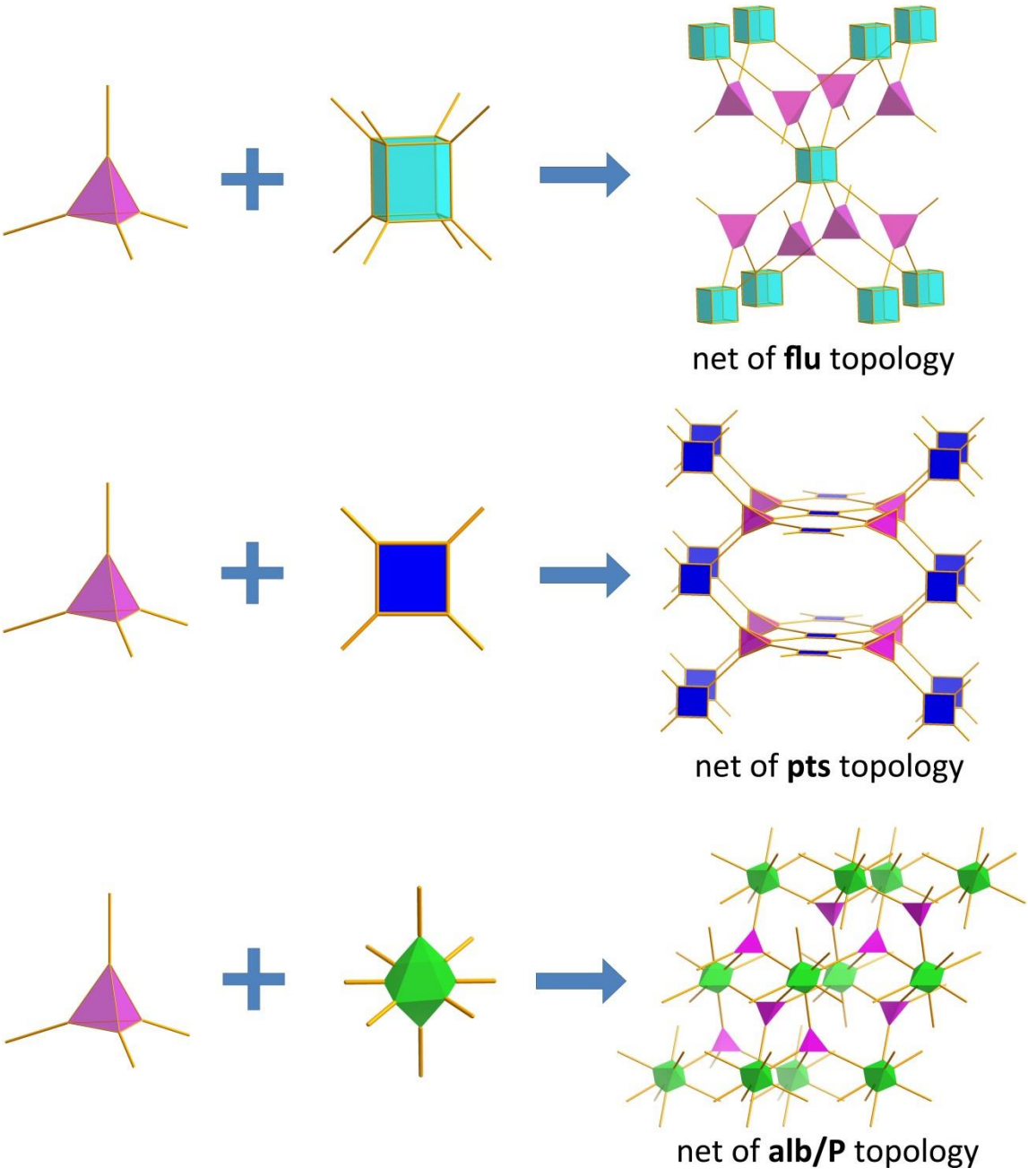

Figure I-3. Graphical representation of different topologies associated with MOFs assembled from tetrahedral ligands.

The fluorite topology (**flu**) is especially interesting for MOF construction for several reasons. First, the fluorite topology is the default topology that connects the tetrahedral nodes and cubical nodes by only one kind of link. This will eliminate the possibilities of forming MOFs with other topologies in the same condition, which makes it possible to predict the structure of resulting MOF before it is made. [82, 83] Second, unlike the **dia**, **pts** or **alb/P** nets, frameworks which may eventually suffer from self-interpenetration when elongated ligands are used, a net with **flu** topology cannot be translated in any direction without overlapping with itself, as the **flu** net is not self-dual. [84] In other words, a framework with **flu** topology is not likely to undergo self-interpenetration. This is extremely helpful for the construction of MOFs with large cavities, since the elongation of organic linkers will typically result in framework interpenetration. Third, MOFs with this topology may exhibit high porosity. A close examination of fluorite reveals its structure as a cubic close packing (ccp) of the calcium where all its tetrahedral interstitial holes are filled by fluoride. It should be noted that all the octahedral interstitial holes remain unoccupied. (Figure I-4(a)) By augmenting the fluoride nodes with a rigid tetrahedral ligand and substituting the calcium nodes with an 8-connected metal-containing cluster, a MOF with the same topology but considerably enlarged interstitial octahedral cavities will be generated. [48]

In order to construct a framework with fluorite topology, the key step is to find the two components that are symmetrically complementary with each other: a 4-connected ligand that can be topologically represented as a tetrahedral node, and an 8-connected metal-containing SBU as a cubical node. One representative example of

fluorite-topology MOF is a framework constructed from the 8-connected [$M_4(\mu_4$-Cl)(tetrazolate)$_8$] clusters, reported by Long group. [85] A tetrazolate-based ligand with tetrahedral geometry, tetrakis(4-tetrazolylphenyl)methane (H_4**TTPM**) should be utilized in this case. This framework, $Cu[Cu_4(\mu_4\text{-}Cl)(TTPM)_2]_2(CuCl_2)(DMF)_5$ was prepared by a solvothermal reaction between $CuCl_2 \cdot H_2O$ and H_4**TTPM** in DMF/methanol mixture in the presence of HCl at room temperature for 4 days. Green tetragonal rod-like crystals were yielded from the reaction. This framework also possesses a fluorite topology net with its octahedral cavity size of 17.8 × 17.8 × 27.5 Å. (Figure I-4(b)) Nevertheless, due to the anionic nature of its metal-containing SBUs, this framework appears to be anionic where many bulky counterions were trapped in its octahedral holes. Its calculated solvent accessible volume is 19.70%. This framework is porous upon activation, with a BET (Brunauer−Emmett−Teller) surface area of 2506 $m^2 \cdot g^{-1}$, while a structural change was observed during the activation process. [68] An isostructural MOF, IMP-16 (IMP represents "Imperial College London"), which is made from an analogous silicon-centered tetrazolate ligand, was also recently reported. It possesses a solvent accessible volume of 74.30% and a BET surface area of 2665 $m^2 \cdot g^{-1}$. [76]

In order to construct a fluorite-topology framework with larger porosity, an 8-connected SBU that is electrically neutral should be carefully selected. Zirconium polyoxo clusters have attracted our attention for their abundance [86], stability [87], and tunable connectivity [53]. PCN-521 (PCN represents "Porous Coordination Network") consists of 8-connected [$Zr_6(\mu_3\text{-}OH)_8(OH)_8$] clusters combined with the **MTBC** ligand (**MTBC**=4',4'',4''',4''''-methanetetrayltetrabiphenyl-4-carboxylate). This MOF possesses

an expected **flu** topology. After the augmentation of 4-connected tetrahedral nodes by the **MTBC** ligand, the "octahedral interstitial cavity" of this framework was significantly amplified to the size of 20.5 × 20.5 × 37.4 Å (Figure I-4(c)), providing the largest cavity of any MOF made from tetrahedral linkers. [48] Due to the chemical resemblance between zirconium and hafnium, an isostructural framework, PCN-523 with hafnium-containing SBUs, was also reported. It should be noted that PCN-521 also possesses the largest solvent accessible volume (78.50%) and BET surface area (3411 $m^2 \cdot g^{-1}$) among all the MOFs with tetrahedral ligands. It is the first example of a non-interpenetrated MOF constructed from the **MTBC** ligand.

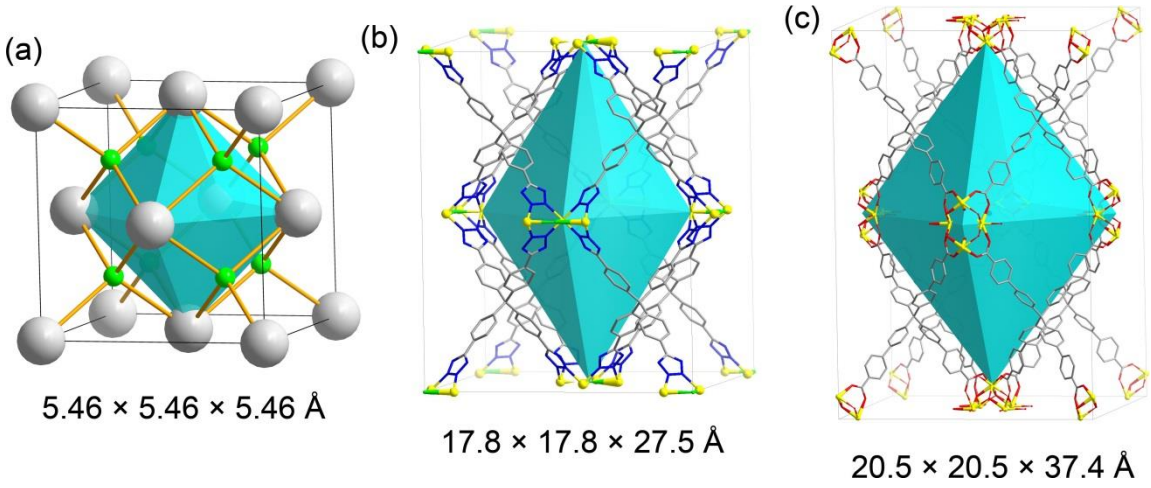

Figure I-4. (a) The graphic representation of the fluorite structure. The turquoise polyhedron represents the unoccupied octahedral interstitial cavities from the ccp of Ca^{2+}. Color Scheme: Ca, gray; F, green. (b) The structure of Cu-TTPM MOF made from the tetrazolate ligand. The counterions are omitted for clarity. (c) The structure of PCN-521. Color Scheme: C, gray; O, red; Zr, yellow.

The platinum sulfide topology (**pts**) is another important network topology associated with tetrahedral linkers. Combination of 4-connected square planar clusters (such as dinuclear paddle-wheel SBUs) and rigid tetrahedral linkers usually results in a framework with this topology. It should be noted that this topology is the default net connecting 4-connected tetrahedral nodes and 4-connected square planar nodes by only one type of link. It should be noted that a few other topological nets (**mog**, **ptt**, etc.) are also related to the combination of 4-connected tetrahedral nodes and 4-connected square planar nodes, but they are not the default net for the combination of them. [84, 88] For instance, a net of moganite topology (**mog**) combines tetrahedral nodes and square planar nodes in a 2:1 ratio with two different types of linkers, [89] and thus a **mog** net is not the default net combining the two different nodes. The non-interpenetrated **pts** net usually adopts a tetragonal space group $P4_2/mmc$. Prominent examples include MOF-11 [62] ($Cu_2(ATC)\cdot 6H_2O$, **ATC**=1,3,5,7-adamantane tetracarboxylate), MOF-36 [63] ($Zn_2(MTBA)(H_2O)_2\cdot(DMF)_6(H_2O)_5$, **MTBA**=methanetetra(4-benzoate)), $Cu_2(MTBA)(H_2O)_2\cdot(DEF)_6(H_2O)_2$, [64] PCN-512 [52] / IMP-9 [73] ($Cu_2(TCPS)(H_2O)_2$, **TCPS**=4,4′,4″,4‴-tetrakiscarboxyphenylsilane, see Figure I-5(a)), and PCN-516 [52] ($Zn_2(TCPS)(H_2O)_2$).

For **pts** topology, further elongation of the tetrahedral linker will eventually result in a self-interpenetrated framework. The combination of a **MTBC** linker (4′,4″,4‴,4⁗-methanetetrayltetrabiphenyl-4-carboxylate) and a dicopper paddle-wheel generates a two-fold interpenetrated network $Cu_2(MTBC)(H_2O)_2$ (Figure I-5(b)).[64] Due to its two-fold interpenetrating nature, the symmetry of its space group was lowered

from $P4_2/mmc$ to $P\text{-}42_1c$. Self-interpenetration has significantly reduced the size of cavities in this MOF. Interpenetrated **pts** frameworks with even longer tetrahedral linkers were also reported. [90] A network with **pts** topology was also observed for metallo ligands with tetrahedral geometry [91, 92] and tetratopic linkers with twisted tetrahedral conformations.[93, 94]

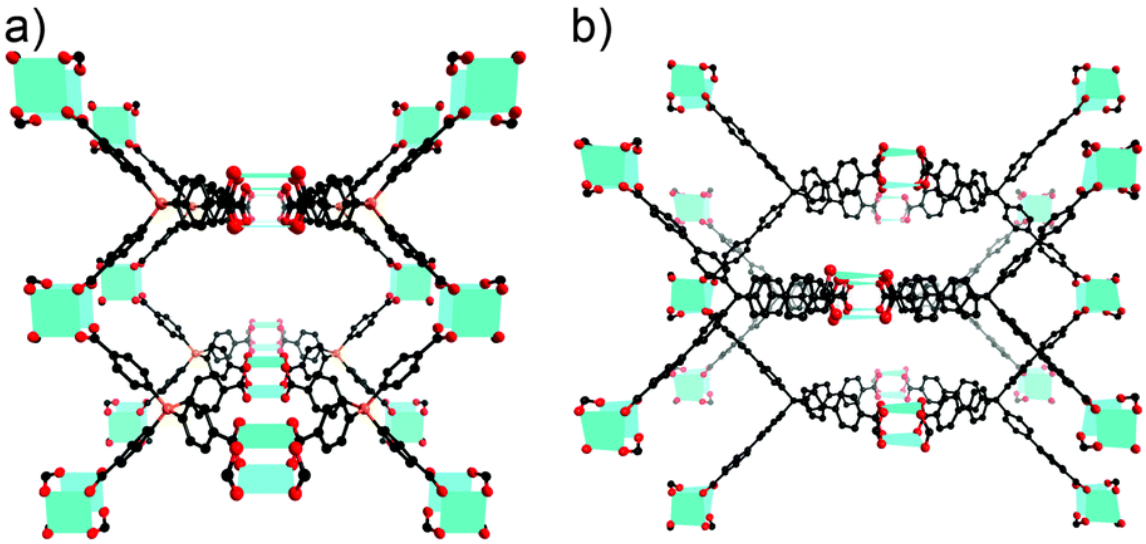

Figure I-5. The crystal structure of (a) PCN-512/IMP-9 with a **pts** topology; (b) $Cu_2(MTBC)(H_2O)_2$ with a doubly interpenetrated **pts** topology. Color scheme: C, black; O, red; Si, orange; Cu, turquoise polyhedra. (Reprinted with permission from Ref. 45, copyright 2014 Royal Chemical Society)

Combining 4-connected tetrahedral linkers and 8-connected hexagonal bipyramidal SBUs produces a net of **alb/P** topology. PCN-511, [52] consisting of TCPS ligand and an 8-connected zinc cluster, is a prominent example. Frameworks with **alb/P**

topology could also suffer from self-interpenetration. For example, when the **MTBC** linker was used, a novel 3D compound containing two-fold interpenetration was obtained. [66] A few other topologies are also related to MOFs assembled from tetrahedral linkers. For example, the diamond (**dia**) topology is a 4,4-connected network observed when the tetrahedral linkers are combined with SBUs that possess a tetrahedral geometry. [65] MOFs with **dia** topology could also suffer from self-interpenetration. [72]

1.3 Metal-Organic Polyhedra: Definition, Structures, and Their Relevance to Metal-Organic Frameworks

Metal-organic polyhedra (MOPs) are another important category of MOMs. Unlike the 3D extended nature of MOFs, MOPs are supramolecular coordination assemblies of discrete cages that typically possess high symmetries, well-defined cavities and predictable structures. [95-98] Due to their fascinating structures and convenient synthetic procedures, they have great potential for applications in materials science and host-guest chemistry. [99, 100] By using organic linkers with different bridging angles, MOPs with a variety of different geometries can be constructed, and the resulting geometries are closely related to the bridging angles of their ligands. [96, 97] Isophthalates are one of the important categories of organic linkers for MOP construction. [95] With a bridging angle of 120 ° between the two adjacent carboxylates, the combination of 24 isophthalate moieties and 12 metal-containing SBUs with square planar geometry yields a cuboctahedral cage with O_h symmetry. (Figure I-6(a))

Utilization of MOPs (or coordination polyhedra) as building blocks appears to be an efficient strategy to construct highly-porous MOFs with desired properties. [101-103] Unlike the fluorite topology MOFs which have only one type of cavity (the interstitial octahedral cavities resulted from the ccp of the SBUs) with uniform size and shape, MOFs with other topologies may possess several different types of cavities. This makes it rather challenging to rationalize the shape and size of frameworks with these topologies. Nevertheless, owing to their well-defined cavities and predictable structures, incorporation of MOPs into extended frameworks (such as MOFs) has significantly simplified the design and synthesis of MOFs with hierarchical cavities. So far, MOFs with cuboctahedral cages are mostly explored due to the relatively easier synthesis of the 120˚-angular-dicarboxylate ligands. A series of (3,24)-connected isoreticular MOFs with **rht** topology were constructed consequently by using coplanar, C_3-symmetric ligands with three isophthalate moieties. [104-110] Even though these MOFs are highly porous, their frameworks were stabilized by the incorporation of "microwindows" whose shape and size were fixed by the isophthalate moieties.

One of these (3,24)-connected isoreticular MOF series, PCN-61, [104] was synthesized by a solvothermal reaction between $Cu(NO_3)_2 \cdot 2.5H_2O$ and H_6**BTEI** (**BTEI**=5,5',5"-benzene-1,3,5-triyltris(1-ethynyl-2-isophthalate)) in DMF in the presence of HBF_4 at 75˚C for 3 days. Its crystal structure can be conceived as the packing of three different types of polyhedral cages with different sizes: a cuboctahedral cage with diameter of 12 Å, a truncated tetrahedral cage with diameter of 15 Å, and a truncated octahedral cage with diameter of 23 Å. In this framework, mesoporous cavities (the

truncated octahedral cages, illustrated as pink spheres) were stabilized by the surrounding microporous cages (cuboctahedral cages, illustrated as yellow spheres) made from the isophthalate moieties. (Figure I-6(b)) This framework possesses a solvent accessible volume of 77.0%, and exhibits a permanent inner porosity after the activation process, with a BET surface area of 3000 $m^2 \cdot g^{-1}$.

As the organic linker is elongated, the size of truncated tetrahedral cages and truncated octahedral cages will expand accordingly, while the size of cuboctahedral cages always remains constant. [104, 105] Consequently, the large cavity can always be stabilized by its surrounding microporous cuboctahedral cavities. Further elongation of the organic linker yields a series of highly porous MOFs, among which NU-110E (see Figure I-6(c), NU represents "Northwestern University") possesses the largest experimental BET surface area among all the existing porous materials to date. [110] NU-110E consists of dicopper paddlewheel SBUs connected by the **BTTEI** ligand (**BTTEI**=5,5',5''-(((benzene-1,3,5-triyl-tris(ethyne-2,1-diyl))tris(benzene-4,1-diyl))tris(ethyne-2,1-diyl))triisophthalate). This framework is isoreticular to the PCN-61 series. Due to its highly porous nature, supercritical CO_2 activation has to be applied to maintain the integrity of its framework. It has a solvent accessible volume of 93.0% and exhibits a BET surface area of 7140 $m^2 \cdot g^{-1}$.

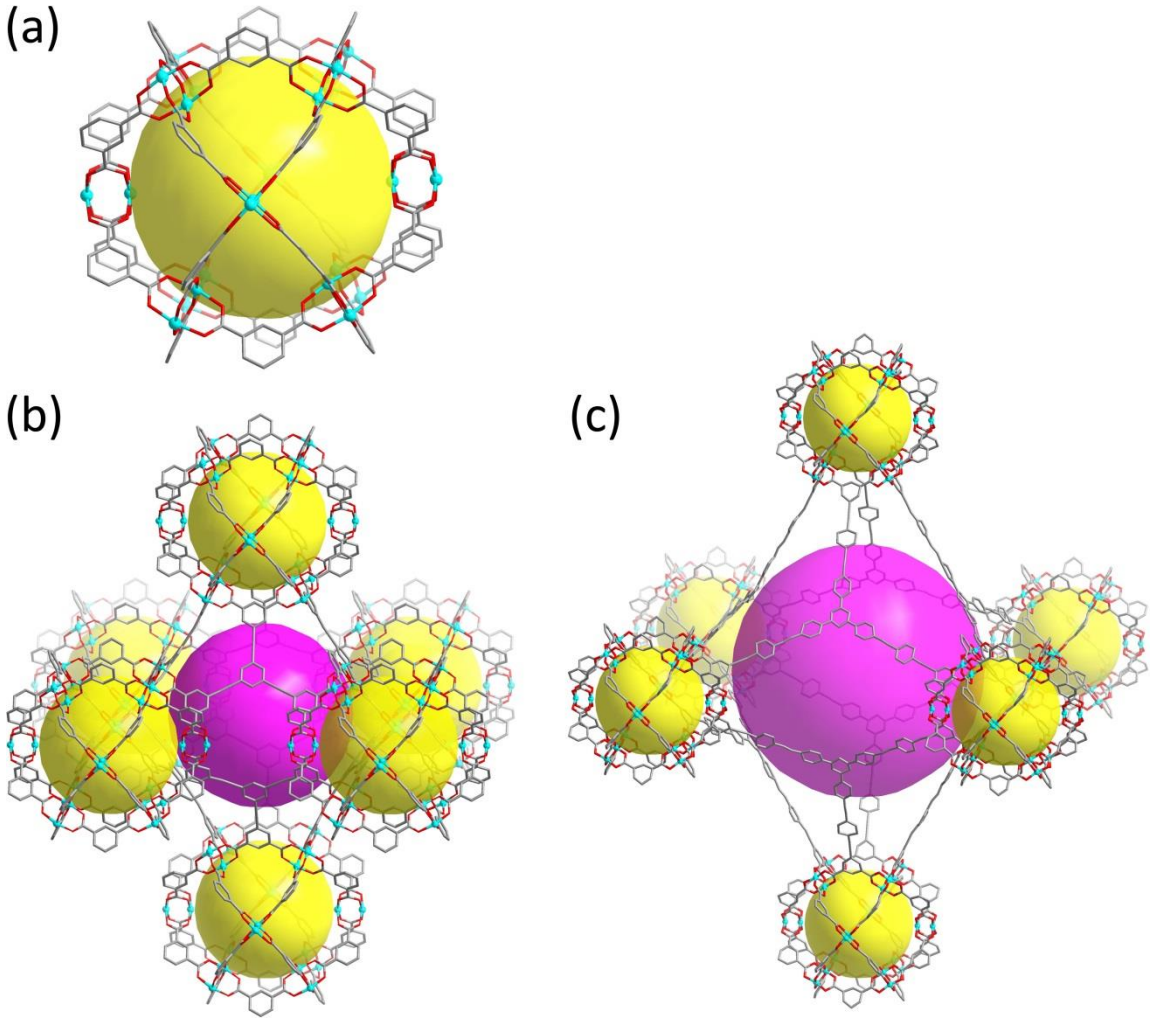

Figure I-6. (a) The graphic representation of a MOP with a cuboctahedral cage. The yellow sphere indicates the empty space inside its cage. (b, c) The crystal structures of PCN-61 and NU-110E, respectively. Both of their frameworks adopt the **rht** topology where their mesoporous cavities (illustrated as pink spheres) were stabilized by the introduction of the microporous cuboctahedral cages (illustrated as yellow spheres) made from the isophthalate moieties. Color scheme: C, gray; O, red; and Cu, cyan. (Reprinted with permission from Ref. 49, copyright 2014 Royal Chemical Society)

1.4 Porous Organic Polymers: Structures, Crystallinity and Applications

Even though MOFs possesses many advantages such as enormous surface area, tunable structures and convenient post-synthetic modifications, most MOFs suffer from limited stability, which restrained their practical applications. [111] Porous organic polymers (POPs), [18] appearing as hyper-crosslinked organic polymers, have provided an alternative solution to the construction of ultra-porous materials with greatly enhanced thermal and chemical stability. Similar to MOFs, POPs are also promising materials for gas storage, [112-114] carbon dioxide sequestration [115-117] and catalysis [118-120]. POPs can exist in both crystalline and amorphous forms, where the crystalline form of POPs are usually termed as covalent organic frameworks (COFs) [121], and the amorphous materials with no long-range periodicity or regularity in their structures are known as porous polymer networks (PPNs). POPs can exhibit extraordinarily large porosity as well, without compromising the stability of this framework. [112] For example, the BET surface area of PPN-4 is 6461 $m^2 \cdot g^{-1}$, which was the largest experimental surface area among all the porous materials at its publication time [113] until NU-110E [110] was recently published. The ultrahigh surface area in PPN-4 was hypothetically attributed to its framework with conceptual diamondoid (**dia**) topology enforced by the rigidity of its tetrahedral monomers (Figure I-7(a)). Tetrahedral building blocks are also exceedingly attractive for the construction of highly porous POPs, because the interconnection between them can provide wide openings and interconnected pores that can efficiently eliminate the "dead spaces". [111-113, 117, 122]

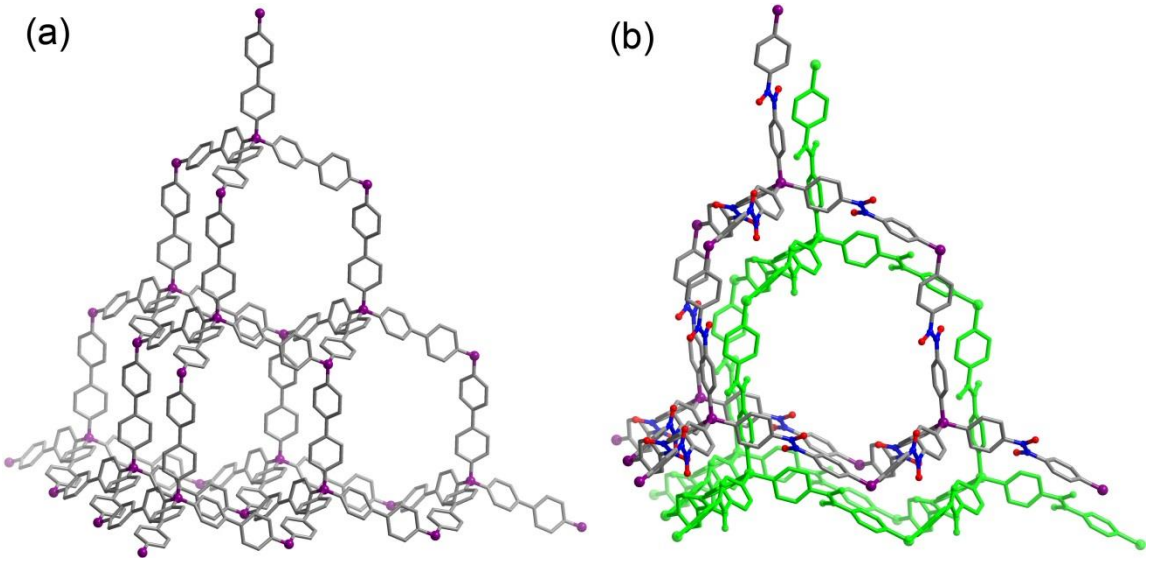

Figure I-7. (a) The conceptual structure of amorphous PPN-4. (b) The single crystal structure of NPN-2. Both of them possess a diamondoid topology. Color scheme: C, gray; O, red; N, blue; and Si, purple. The green network illustrates the self-interpenetrated nature of NPN-2. The actual structure of NPN-2 is a four-fold interpenetrated framework; only two of them are illustrated in the figure for clarity.

It should be noted that the division between COFs and PPNs is far from absolute. As novel synthetic techniques were employed, it is now possible for chemists to synthesize "PPNs" in the crystalline form for a careful examination of their single crystal structures. A novel category of 3D crosslinked organic polymers, the NPN series, was synthesized through the coupling of tetrahedral nitroso compounds, where the nitroso groups can dimerize reversibly to form azodioxides. [122] For example, NPN-2 was synthesized by the polymerization of a tetrahedral compound, tetrakis(4-nitrosophenyl)silane. Unlike the completely non-crystalline nature of PPN-4, NPN-2 can

be obtained in single crystals that are suitable for subsequent crystallographic studies. Single-crystal X-ray diffraction reveals that NPN-2 crystallizes in tetragonal space group *P*-4*b*2, and it possesses a four-fold interpenetrated framework where each individual net adopts a diamondoid topology. (Figure I-7(b))

In the past two decades, chemists have witnessed the exceedingly rapid growth of research on advanced porous materials. As a burgeoning field, APMs have quickly outshined the traditional porous materials in many potential applications due to their fascinating structures, extremely large porosities, and tunable properties. Nevertheless, it is still of great importance for chemists, materials scientists, and engineers to initiate a substantial amount of research on APMs in order to fully understand their structure-property relationships, and achieve a genuine rational design of APMs whose properties are accurately predictable before these materials can be made. In addition, many APMs suffer from complicated synthetic routes and expensive costs, which can potentially impede their industrial applications. More studies are still essential to address all the obstacles on the road to APM commercialization.

CHAPTER II

STRUCTURAL DESIGN OF METAL-ORGANIC FRAMEWORKS WITH TETRAHEDRAL BUILDING UNITS [*]

2.1 Introduction

For the past few years, MOFs have gained a tremendous amount of attention because of their novel structures and diverse applications, where the ligand design is of vital importance in the preparation of MOFs with proposed topology, desired porosity and expected functionality. [43, 44] Due to the extraordinary degree of variability of both their organic linkers and their metal-containing SBUs, much research has been carried out on the structural characteristics of MOFs, such as the geometry of ligands, the resulting topology, and the framework porosity. Unlike other ligand geometries that have been comprehensively studied by MOF chemists, investigations of MOFs with rigid tetrahedral ligands are still relatively rare. [45] For this reason, it is difficult for researchers to have an all-inclusive look at the geometrical and topological significance of tetrahedral building units. Although many PPNs have been constructed from tetrahedral building units [111-113], the lack of crystalline structure in PPNs has prevented us from studying the symmetry of the tetrahedral building units in those materials. MOFs with rigid tetrahedral building units have already been explored by some research groups, but the majority of them suffer from a series of complications such as complicated ligand

[*] Reproduced with permission from "Structural Design of Porous Coordination Networks from Tetrahedral Building Units", by Zhang, M.; Chen, Y.-P.; Zhou, H.-C., *CrystEngComm*, **2013**, *15*, 9544-9552, copyright 2014 by Royal Society of Chemistry.

synthesis, limited porosity, and unexpected self-interpenetration. Only few of those works have undertaken a systematic study of tetrahedral building units from a symmetric point of view. [73] Davies and co-workers have prepared some novel silicon-centered ligands for MOF construction, [73-76] where the introduction of silicon-centered ligands has largely simplified the process for preparing tetrahedral ligands. However, regardless of the porous nature of some of their MOFs, the authors did not publish any investigation of their porosity and gas sorption properties. Herein, we introduce eight MOFs constructed from this synthetically accessible silicon-centered ligand, provide the gas adsorption behaviors of the stable ones, and afford a systematic outlook of tetrahedral ligands from the symmetry perspective. All these MOFs were structurally characterized and are inherently porous with solvent accessible volume up to 73.10%; while at least two of them possess a permanent inner porosity after the removal of any guest molecules in the framework. Among all these MOFs, seven of them possess a new structure, one of them possesses a novel topology, and two of them show properties potentially useful for gas storage applications.

Regardless of the aforementioned drawbacks of the tetrahedral ligands, they are highly desirable for MOF synthesis, especially the easily prepared and commercially affordable ones. This is because the tetrahedral ligand is a fully extended strut. Once incorporated into the framework with symmetrically compatible SBUs, its inherent three-dimensional nature will ensure the framework porosity and provide a framework with ultralarge pore sizes. Also, since the tetrahedral ligand is a highly symmetric building unit with a full T_d geometry, it possesses a diversity of symmetric elements that

can play many different roles in the construction of the framework. When a full T_d geometry is not compatible with the geometry of a certain metal SBU, it may reduce its symmetry and exhibit any subgroups of the T_d group during the formation of the framework. (See Figure I-2) Due to their symmetrical variety, MOFs with a diversity of topology can be constructed from the tetrahedral building units and thus they are particularly stimulating to study from a topological point of view. [52]

Production cost is always a primary concern for practical application of any materials. Despite their high surface areas and gas uptake capacities, many MOFs suffer from complicated multi-step ligand synthesis from expensive reagents. This makes it difficult to find any practical applications for them. The H_4**TCPS** (**TCPS**=4,4′,4″,4‴-tetrakiscarboxyphenylsilane) ligand has gained our attention because of both its tetrahedral structure and the simplicity of its synthesis. The inexpensive starting materials, two-step synthesis, and high yield reactions that do not require the utilization of any noble-metal catalyst or flash chromatography have made it an especially promising ligand for MOF research. Solvothermal reactions between the H_4**TCPS** and various metals have yielded eight MOFs, seven of which possess a novel structure, and one of which possesses a novel MOF topology.

2.2 Experimental Section

2.2.1 Materials and Instrumentation

The ligand H_4**TCPS** was synthesized by a modified procedure previously reported in the literature. (Scheme II-1) [123] All chemicals were used without further

purification unless otherwise mentioned. Silicon tetrachloride ($SiCl_4$) and *n*-butyl lithium (*n*-BuLi) were purchased from Sigma Aldrich, and all other chemicals were purchased from VWR unless mentioned otherwise. ^1H nuclear magnetic resonance (NMR) data were recorded on a Mercury 300 MHz NMR spectrometer at the Center for Chemical Characterization and Analysis (CCCA), Department of Chemistry, Texas A&M University. Fourier transform infrared spectroscopy (FTIR) data were collected using a SHIMADZU IRAffinity-1 FTIR Spectrophotometer. Thermogravimetric analyses (TGA) were performed on a SHIMADZU TGA-50 Thermogravimetric Analyzer with a heating rate of 5 ℃·min^{-1} under N_2. Gas sorption measurements were conducted using a Micrometritics ASAP 2020 system at listed temperatures.

2.2.2 Ligand Synthesis

The synthesis of H_4**TCPS** ligand was illustrated in Scheme II-1.

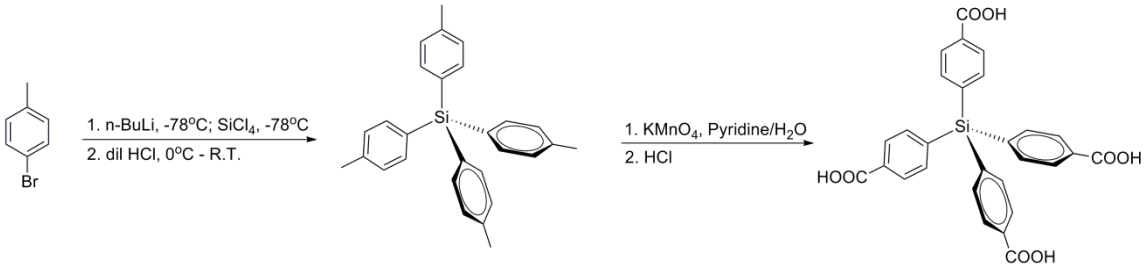

Scheme II-1. Synthesis of the H_4**TCPS** ligand. Compared to many other tetrahedral ligands, this ligand can be obtained from a two-step synthesis without any expensive catalysts or flash chromatography.

Synthesis of tetrakis(4-tolyl)silane. [123] A 500 mL round bottom flask equipped with a condenser was pumped under vacuum and refilled with N_2 three times before the dry 4-bromotoluene (pre-dried by molecular sieves, 17.10 g, 12.3 mL, 0.1 mol) was added. Freshly distilled THF from a solvent still (300 mL) was carefully added to the flask through a cannula. The solution was cooled to -78˚C by a dry ice/acetone bath. At this temperature, *n*-butyl lithium (40 mL, 2.5 M in hexane) was added dropwise in a careful manner for 1 hour. The reaction mixture was kept at -78˚C for an additional 2 hours before $SiCl_4$ (2.86 mL, 25 mmol) was added dropwise. The mixture was stirred at this temperature for an additional 2 hours before it was warmed up to room temperature and kept overnight. The reaction mixture was quenched with 2 M HCl (60 mL) and extracted with ethyl acetate (100 mL×3). The combined organic phase was washed with brine, dried over $MgSO_4$ and evaporated to give the crude product. A recrystallization in EtOAc/Hexane afforded 6.94 g white crystalline powder as the final product (70.78%). ^{1}H NMR (300 MHz, DMSO-d_6): δ =7.32 (d, 8H, Ph), 7.22 (d, 8H, Ph), 2.32 (s, 12H, Me).

Synthesis of 4,4′,4″,4‴-tetrakiscarboxyphenylsilane. A 500 mL round-bottomed flask was charged with 3.92 g (10 mmol) of tetrakis(4-tolyl)silane, 50 mL of water and 150 mL of pyridine. While the reaction was refluxing, 30 g $KMnO_4$ was added carefully in three portions and the reaction mixture was refluxed overnight. The flask was then cooled to room temperature and CH_3OH was added slowly to decompose unreacted potassium permanganate. Filtration provided a clear solution and the solid was washed with hot water. The filtrate was concentrated to dryness and 50 mL water was added to dissolve the solid. Concentrated HCl was added cautiously until no more

precipitate formed. Filtration provided a white solid which was used for the following experiments. An analytical sample was obtained by recrystallization in acetic acid (2.66 g, 52%). ^{1}H NMR (300 MHz, DMSO-d_6): δ = 8.02 (d, 8H, Ph) and 7.62 (d, 8H, Ph).

2.2.3 MOF Synthesis

Synthesis of PCN-511, $Zn_3(HTCPS^{3-})_2$. All the following MOFs (PCN-511 – PCN-517) were synthesized by solvothermal reactions in a 2 mL Pyrex vial unless otherwise mentioned. In order to perform the gas adsorption study, an adequate amount of the products (more than 100 mg) were accumulated by performing identical reactions in multiple vials before the samples were combined and activated. H_4**TCPS** (6.4 mg, 0.0125 mmol) and $Zn(NO_3)_2$ $6H_2O$ (22 mg, 0.075 mmol) were ultrasonically dissolved in 1.7 mL *N*,*N*′-diethylformamide (DEF). The reaction mixture was then heated in an 85 ℃ oven for 48 h before it was allowed to cool to room temperature. Large, colorless, blocky crystals were obtained (4.8 mg, 64%).

Synthesis of PCN-512, $Cu_2(TCPS^{4-})(H_2O)_2$. H_4**TCPS** (6.4 mg, 0.0125 mmol) and $Cu(NO_3)_2$ $\cdot 2.5H_2O$ (17 mg, 0.075 mmol) were ultrasonically dissolved in 1.7 mL *N*,*N*′-dimethylacetamide (DMA) with the presence of two drops of tetrafluoroboric acid (HBF_4, 48%). The reaction mixture was then heated in an 85 ℃ oven for 24 h before it was allowed to cool down to room temperature. Large, blue, diamond-shaped crystals were obtained (4.2 mg, 53%).

Synthesis of PCN-513, $Zn_5(\mu_3\text{-}OH)_2(TCPS^{4-})_2(DMF)_2(NMP)_4$. H_4**TCPS** (6.4 mg, 0.0125 mmol) and $Zn(NO_3)_2$ $6H_2O$ (22 mg, 0.075 mmol) were ultrasonically

dissolved in 1.4 mL *N*,*N*′-dimethylformamide (DMF) and 0.3 mL *N*-methyl-2-pyrrolidone (NMP). The reaction mixture was then heated in an 85 ℃ oven for 48 h before it was allowed to cool to room temperature. Two different types of single crystals were identified. Beside PCN-511, another distinct crystal that appears to consist of colorless blocks was shown in the product. This impurity was identified as PCN-511, and no reaction producing phase-pure PCN-513 was identified yet.

Synthesis of PCN-514·DMF, $Cd_4(TCPS^{4-})_2(DMF)_8$. H_4**TCPS** (6.4 mg, 0.0125 mmol) and $Cd(NO_3)_2 \cdot 4H_2O$ (23 mg, 0.075 mmol) were ultrasonically dissolved in 1.4 mL DMF and 0.3 mL NMP. The reaction mixture was then heated in an 85 ℃ oven for 48 h before it was allowed to cool down to room temperature. Large, colorless, blocky crystals were obtained (8.3 mg, 65%).

Synthesis of PCN-514·DMA·NMP, $Cd_4(TCPS^{4-})_2(DMA)_4(NMP)_2(H_2O)_2$. H_4**TCPS** (6.4 mg, 0.0125 mmol) and $Cd(NO_3)_2 \cdot 4H_2O$ (23 mg, 0.075 mmol) were ultrasonically dissolved in 1.4 mL DMA and 0.3 mL NMP. The reaction mixture was then heated in an 85 ℃ oven for 48 h before it was allowed to cool to room temperature. Large, blocky crystals were obtained (7.6 mg, 59%).

Synthesis of PCN-515, $[Zn_4(\mu_4\text{-}O)(H_2O)][Zn_3(\mu_3\text{-}OH)(H_2O)_3][Zn_2(H_2O)](HTCPS^{3-})(TCPS^{4-})_3$. H_4**TCPS** (6.4 mg, 0.0125 mmol) and $Zn(NO_3)_2 \cdot 6H_2O$ (22 mg, 0.075 mmol) were ultrasonically dissolved in 1.4 mL DMA and 0.3 mL NMP. The reaction mixture was then heated in an 85 ℃ oven for 96 h before it was allowed to cool to room temperature. Large, colorless, blocky crystals were obtained.

Synthesis of PCN-516, $Zn_2(TCPS^{4-})(H_2O)_2$. H_4**TCPS** (3.2 mg, 0.0063 mmol) and $Zn(NO_3)_2$ $6H_2O$ (22 mg, 0.075 mmol) were ultrasonically dissolved in 1.7 mL DMA. The reaction mixture was then heated in an 85 ℃ oven for 72 h before it was allowed to cool to room temperature. Large, colorless, columnar crystals were obtained.

Synthesis of PCN-517, $Cd_4(TCPS^{4-})_2(H_2O)_4$. H_4**TCPS** (3.2 mg, 0.0063 mmol) and $Cd(NO_3)_2$ $4H_2O$ (23 mg, 0.075 mmol) were ultrasonically dissolved in 1.7 mL DMF. The reaction mixture was then heated in a 100 ℃ oven for 48 h before it was allowed to cool to room temperature. Large, colorless, blocky crystals were obtained.

2.2.4 Structure Determination of Single Crystals

All compounds, PCN-511 – PCN-517 were taken from the solution directly, transferred into oil and mounted onto a loop for single crystal X-ray data collection. Diffraction patterns were measured on a Bruker Smart Apex diffractometer equipped with a Mo-Kα sealed-tube X-ray source (λ = 0.71073 Å) under protection of N_2 stream at 110 K. The data frames were recorded using the program APEX2 and processed using SAINT routine within APEX2. The data were corrected for absorption and beam corrections based on the semi-empirical technique as implemented in *SADABS*. All structures were solved by direct methods using *SHELXS* and refined by full-matrix least-squares on F^2 using *SHELXL* software.

Non-hydrogen atoms were refined with anisotropic displacement parameters during the final cycles, whereas organic hydrogen atoms were located with isotropic displacement parameters set to 1.2 $\times U_{eq}$ of the attached atoms. Attempts to locate and

refine the strong solvent peaks were successful, but contributions to scattering due to those highly disordered solvent molecules were removed using the SQUEEZE routine of PLATON; structures were then refined again using the data generated.

The detailed information about the solution and refinement of the single crystal structures can be found in the electronic supplementary materials of this manuscript. [52] Their crystal structures are available at the Cambridge Crystallographic Data Centre (CCDC) with assigned deposition numbers 942372 –942378.

2.2.5 Activation Procedures and Gas Sorption Measurements

The fresh MOF samples must be activated prior to any gas sorption measurements. In order to remove any unreacted starting materials and trapped compounds in their pores, the as-synthesized PCN-511 (~100 mg) samples were treated by solvent exchange with DMF 4 times and acetone 4 times for about 12 h each. After the careful removal of acetone by decanting, the sample was transferred into a sorption tube and activated under dynamic vacuum at room temperature for 6 h. It was then activated by using the 'outgas' function of the adsorption instrument for 12 h at 100 ˚C prior to any gas adsorption–desorption measurement.

The fresh PCN-512 samples were activated by using freeze-thaw activation procedures. [64, 124] After the as-synthesized PCN-512 (~100 mg) samples was treated by solvent exchange with DMF 4 times and acetone 4 times, the dark blue crystals were further solvent exchanged with benzene twice before loading into a sorption tube. A small amount of benzene was left in the sorption tube, and the sample was treated with

an ice/water bath in the presence of NaCl (-10 ˚C) and subsequently by three freeze-thaw cycles. The sample was then treated with an ice/water bath in the presence of NaCl (-10 ˚C) under a dynamic vacuum overnight until all the benzene was removed. The bath was removed and the sample was kept under vacuum at room temperature for another 24 h. It was activated by using the 'outgas' function of the adsorption instrument for 12 h at 85 ℃ prior to any gas adsorption/desorption measurement.

2.3 Results and Discussion

2.3.1 Characterization of Crystal Structures

The structure of PCN-511. Single crystal XRD reveals that PCN-511 crystallizes in *C*2/*c* space group where Zn_3 clusters are connected by tetrahedral ligands. In this SBU, two Zn ions are four coordinated and one is six coordinated (Figure II-1(a)), which resembles the SBU in the MOF constructed from an elongated rigid tetrahedral ligand with Zn ions in the presence of DEF, as reported by the Lin group. [66] Each SBU was connected to six carboxylate groups (COO^-) and two carboxylic acid groups (COOH) to balance the positive charge on the Zn_3 cluster. Each asymmetric unit in this MOF consists of 1.5 Zn ions and one partially deprotonated H**TCPS**$^{3-}$ ligand. Due to the rigidity and the fully extended nature of the tetrahedral ligand, PCN-511 exhibits 3D channels with diameter 5 Å along the *c* axis (Figure II-1(b)) and diameter 6 Å along the 011 axis. Each Zn_3 SBU is connected to eight different tetrahedral ligands to form a 4, 8-connected 3D framework of a rare **alb**/**P** topology [66] (Figure II-1(c)) denoted as

$(4^4 \cdot 6^2)_2(4^8 \cdot 6^{17} \cdot 8^3)$. The calculated solvent accessible volume of PCN-511 is 45.60% by *PLATON* platform. [125]

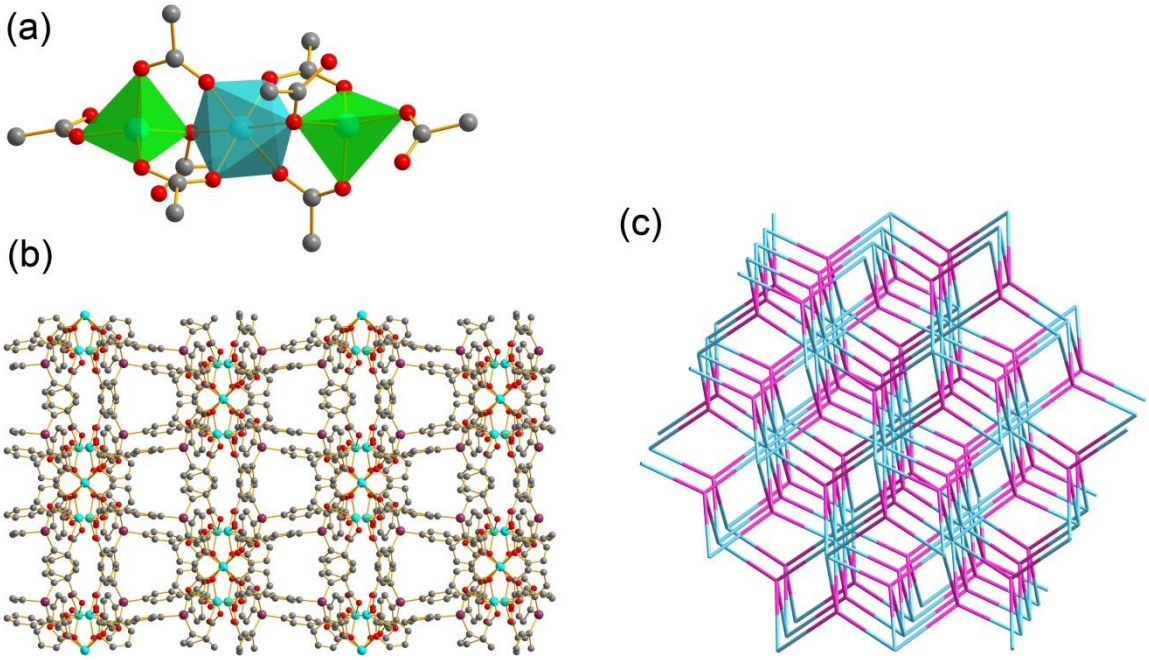

Figure II-1. (a) The eight-connected Zn_3 SBU, where the green and cyan polyhedra represent 4- and 6-coordinated Zn, respectively. (b) The representation of the crystal structure of PCN-511. Color scheme: C, gray; O, red; Si, purple; and Zn, cyan. H atoms were omitted for clarity. (c) The topology of PCN-511, where the cyan and magenta nodes represent 8- and 4-connected nodes, respectively.

It should be noted that the framework of PCN-511 has the same connectivity as that of IMP-11 [73] without any crystallographic evidence of the existence of dimethylammonium cations in the pores. With the same network connectivity, IMP-11 was reported by Davies *et al.* as an anionic framework with the $Me_2NH_2^+$ cations trapped

inside as the counterions. In their original work, IMP-11 was identified from a solvothermal reaction in DMF/H_2O that had yielded a mixture of crystals where many of the crystals, including IMP-11, could not be obtained purely. However, PCN-511 can be obtained in pure phase if DEF is used as the solvothermal solvent. Its purity and porosity have encouraged us to study its gas adsorption properties, which will be illustrated in detail in the following sections.

The structure of PCN-512 (IMP-9). Single crystal XRD study shows that PCN-512 crystallizes in the tetragonal space group $P4_2/mmc$, where the 4-connected copper paddlewheels were connected by the tetrahedral ligand to form a 4, 4-connected network with **pts** topology denoted as $(4^2 \cdot 8^4)$. The calculated solvent accessible volume of PCN-512 is 72.70% by *PLATON* platform. [125] This material has exactly the same structure as IMP-9 synthesized by Davies *et al*, [73] who studied this MOF from a structural point of view without providing any gas adsorption data; whereas the gas sorption isotherms of this MOF were carefully examined in this work.

The structure of PCN-513. Single crystal XRD reveals that PCN-513 crystallizes in the $P\bar{1}$ space group where $Zn_5(\mu_3\text{-}OH)_2$ clusters were connected by the tetrahedral ligands. In this SBU, four Zn ions are four coordinated and one in the center is six coordinated. (Figure II-2(a)) Two hydroxide groups were identified in this SBU, where each OH^- coordinates to two 4-coordinated Zn and one 6-coordinated Zn. The hydrogen atom on the OH^- groups can be determined by Fourier peaks, which are 0.964 Å away from the riding oxygen atoms, indicating the excellent crystal quality. This OH^- group is hydrogen bonded to the oxygen atom on a nearby carboxylate group where the

H···O distance is 1.931 Å. This is a rarely seen hydrogen-bond-incorporated SBU in MOFs, where, we believe, the O–H···O hydrogen bonding interaction has facilitated the formation of this peculiar $Zn_5(\mu_3\text{-}OH)_2$ SBU. (Figure II-2(a)) Two of the 4-coordinated Zn ions were coordinated with a DMF solvent. Two NMP molecules were identified in the pores of this MOF from the crystallographic data. The porosity of this structure was calculated after all solvents were removed, and the calculated solvent accessible volume of PCN-513 is 44.10% according to the calculation of *PLATON* routine.[125] After the solvents were squeezed, three dimensional channels can be identified in this structure. (Figure II-2(b)); however, gas adsorption properties were not investigated due to likely stability issues of the SBU, which will probably collapse upon the removal of the coordinating DMF solvents. [126] Each $Zn_5(\mu_3\text{-}OH)_2$ cluster connected to eight different tetrahedral ligands, forming a 4, 8-connected 3D framework with a very rare **flu** topology [48, 68, 70] denoted as $(4^{12}\cdot6^{12}\cdot8^4)(4^6)_2$. (Figure II-2(c))

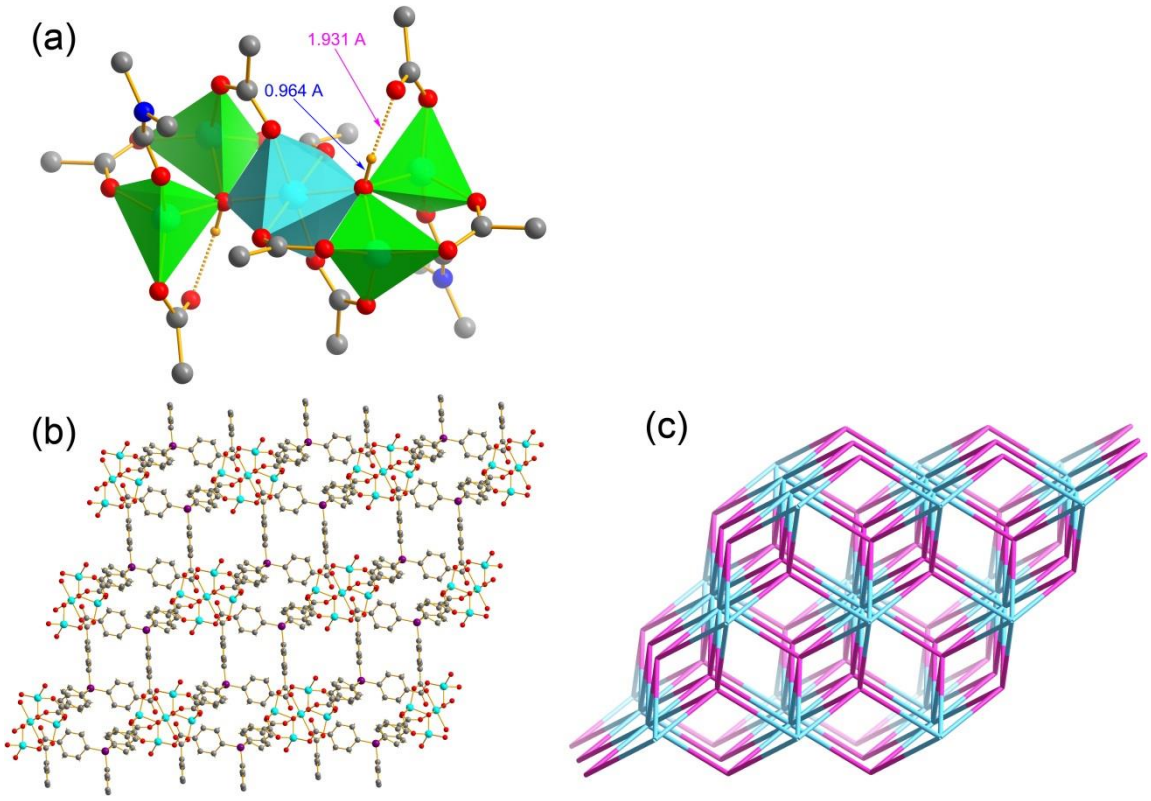

Figure II-2. (a) The $Zn_5(\mu_3\text{-}OH)_2$ SBU where the H atoms (yellow sphere) on the OH^- groups can be determined by Fourier peaks. The green and cyan polyhedra represent 4- and 6-coordinated Zn, respectively. The distances of O–H bond and the H···O hydrogen bond were given, respectively. (b) The representation of the crystal structure of PCN-513 along c axis after removal of all solvents. Color scheme: C, gray; O, red; Si, purple; and Zn, cyan. H atoms were omitted for clarity. (c) The topology of PCN-513, where the cyan and magenta nodes represent 8- and 4-connected nodes, respectively.

The structure of PCN-514. Colorless, blocky crystals of $Cd_4(TCPS^{4-})_2(DMF)_8$ (PCN-514·DMF) and $Cd_4(TCPS^{4-})_2(DMA)_4(NMP)_2(H_2O)_2$ (PCN-514·DMA·NMP) were solvothermally synthesized by the aforementioned procedure. Single crystal XRD

reveals that PCN-514 crystallizes in the $P\bar{1}$ space group where Cd_3 clusters were connected by eight tetrahedral ligands. In this cluster, each Cd is six-coordinated. (Figure II-3(a)) The Cd_3 cluster in PCN-514 is connected by eight carboxylate groups (COO^-), which makes it an anionic framework. Notably, an unanchored Cd ion with six coordinating solvent molecules can be crystallographically identified, which is the counterion to balance the negative charge on the SBU. While the connectivity of the framework of PCN-514·DMF and PCN-514·DMA·NMP are exactly the same, the coordinating molecules on the unanchored Cd vary by using different solvents. In PCN-514·DMF, six DMF molecules were coordinated to the unanchored Cd (Figure II-3(b)); whereas in PCN-514·DMA·NMP, two molecules of DMA, two molecules of NMP and two molecules of H_2O were coordinated to it (Figure II-3(c)), where the H_2O was hydrogen bonded to a carboxylate in the Cd_3 cluster and a free DMA molecule in the pore (Figure II-3(e)), respectively. The two hydrogen atoms on H_2O can be determined by Fourier difference map, which gave two peaks 0.960 Å away from the oxygen atoms, It should be noted that this hydrogen bond does not exist in PCN-514·DMF, which has no coordinating H_2O molecules (Figure II-3(b)), whereas an additional free DMF molecule can be identified in its pores. Regardless of the existence of the unanchored Cd ions and some non-coordinated solvents in the pore, the framework is microporous with three dimensional channels after removal of all trapped species. (Figure II-3(d)). The solvent accessible volume of this structure was 52.40% after the removal of all the unanchored Cd ions and free solvent molecules. [125] Each Cd_3 cluster connects to eight

different tetrahedral ligands to form a 4, 8-connected 3D framework of a **flu** topology [48, 68, 70] denoted as $(4^{12}\cdot6^{12}\cdot8^{4})(4^{6})_2$. (Figure II-2(c)).

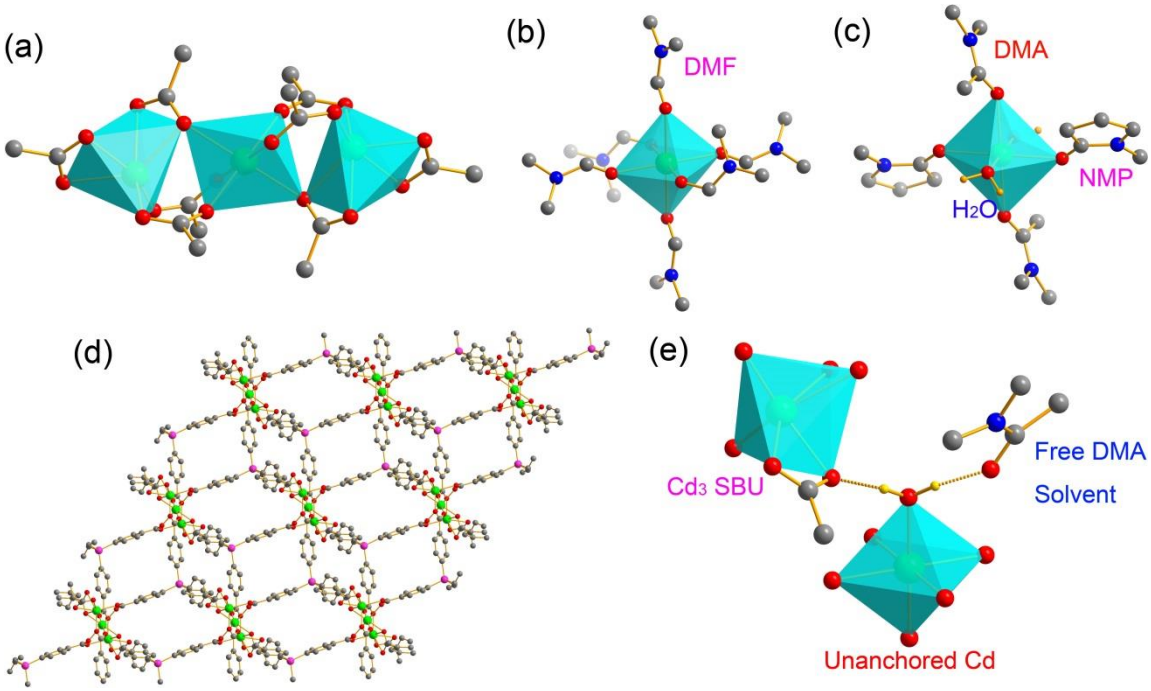

Figure II-3. The crystal structure of PCN-514. (a) The Cd_3 SBU where the cyan polyhedra represent 6-coordinated Cd. (b) The unanchored Cd ion in PCN-514·DMF, where the Cd is coordinated to six DMF molecules. (c) The unanchored Cd ion in PCN-514·DMA·NMP, where the Cd is coordinated to two molecules of DMA, two molecules of NMP and two molecules of H_2O. (d) The representation of the crystal structure of PCN-514 along an axis after removal of all unanchored Cd complexes. Color scheme: C, gray; O, red; N, blue; Si, purple; and Cd, green. H atoms were omitted for clarity. (e) The two hydrogen bonds on the H_2O molecule in PCN-514·DMA·NMP, where one is bonded to the Cd_3 SBU and the other one is bonded to a free DMA solvent in the pore.

The structure of PCN-515. Single crystal XRD reveals that PCN-515 crystallizes in $P2_1/c$ space group where three distinct Zn SBUs were discovered in its structure. This structure consists of a 7-connected $Zn_4(\mu_4\text{-O})$ SBU, a 5-connected $Zn_3(\mu_3\text{-OH})$ SBU and a 4-connected Zn_2 SBU in 1:1:1 ratio, where all the SBUs have never been observed in other porous Zn MOFs. Unlike the commonly 6-connected $Zn_4(\mu_4\text{-O})$ SBU (usually known as Zn_4O for MOF chemists) with a perfect octahedral geometry that was found in MOF-5 [14] and many other MOFs, this MOF has adopted a distorted 7-connected Zn_4O since the tetrahedral nodes (the ligand) and octahedral nodes (the regular Zn_4O cluster) do not appear to be compatible with each other in the formation of any three dimensional networks among all the current existing MOF examples. Each 7-connected Zn_4O cluster was linked with six carboxylate groups (COO^-) and one carboxylic acid group (COOH). This can be further substantiated by the crystallographic data, where six COO^- were coordinated to the Zn_4O cluster as a bridging ligand and one COOH coordinated in a different way as a monodentate ligand (Figure II-4(a)). With a coordinating H_2O molecule, it has generated a 7-connected Zn_4O SBU in which two Zn ions are four coordinated and the other two are five coordinated (Figure II-4(a)). Another SBU is a 5-connected $Zn_3(\mu_3\text{-OH})$ SBU (Figure II-4(b)). With three coordinating H_2O molecules, this SBU contains one 4-coordinated Zn, one 5-coordinated Zn and one 6-coordinated Zn, where one of the H_2O molecules on the 6-coordinated Zn is hydrogen bonded to the carboxylate that coordinates to the 4-coordinated Zn as a monodentate ligand (Figure II-4(b)). The last SBU is a 4-connected Zn_2 SBU that resembles a $Zn_2(COO^-)_4$ paddlewheel (Figure II-7(b)), but there are only three bridging carboxylates

in this paddlewheel-like structure (Figure II-4(c)). An additional carboxylate was coordinated to one of the Zn ions as a monodentate ligand, where the other Zn ion was coordinated by H_2O at the same position. This has made both of the Zn ions in this SBU 4-coordinated (Figure II-4(c)). It should be noted that all these SBUs have seldom been observed in the previous MOFs, which makes PCN-515 an extremely rare example of a MOF that incorporates three rarely seen SBUs in the same network.

The asymmetric unit in this MOF consists of one 7-connected $Zn_4(\mu_4\text{-O})$ SBU, one 5-connected $Zn_3(\mu_3\text{-OH})$ SBU and one 4-connected Zn_2 SBU together with four **TCPS** ligands that are connected to the metal SBUs in completely different fashions. This makes the four **TCPS** ligands both chemically and topologically different (Figure II-5 (a) – (d)), which results in a new 4, 4, 4, 4, 4, 5, 7-connected network (Figure II-5(e)) that has not been reported in the literature. In its asymmetric unit, one TCPS ligand (represented as the red node) was connected to three $Zn_4(\mu_4\text{-O})$ SBUs and one $Zn_3(\mu_3\text{-OH})$ SBU (Figure II-5(a)); another (represented as the orange node) was connected to three $Zn_4(\mu_4\text{-O})$ SBUs and one Zn_2 SBU (Figure II-5(b)). The other tetrahedral ligand (represented as the magenta node) was connected to one $Zn_4(\mu_4\text{-O})$ SBU, two $Zn_3(\mu_3\text{-OH})$ SBUs and one Zn_2 SBU (Figure II-5(c)); while the last one (represents as the yellow node) was connected with two $Zn_3(\mu_3\text{-OH})$ SBUs and two Zn_2 SBUs (Figure II-5(d)). This network can be denoted as $(4\cdot6^5)_2(4^3\cdot6^3)(4^3\cdot6^6\cdot8)(4^4\cdot6^2)(4^5\cdot6)(4^9\cdot6^9\cdot8^3)$. It is worth mentioning that one of the tetrahedral ligands is topologically identical to the 4-connected Zn_2 SBU, which has the extended point symbols $\{4\cdot6(2)\cdot6\cdot6(2)\cdot6\cdot6(2)\}$.

The rigidity of the fully extended tetrahedral ligands has resulted in the inherent porosity of PCN-515. The diameters of the channels are 6 Å along the b axis (Figure II-6(a)) and 7 Å along c axis (Figure II-6(b)), where the diameter of the molecular cages that were surrounded by tetrahedral ligands and the three SBUs is about 11 Å. The calculated solvent accessible volume of this MOF is as large as 70.50% according to the calculation of *PLATON*. [125] However, due to the possible stability issue of the 5-connected $Zn_3(\mu_3\text{-OH})$ SBU and 4-connected Zn_2 SBU, which will probably collapse upon the removal of the coordination solvent, [126] the gas uptake study was not performed in this MOF.

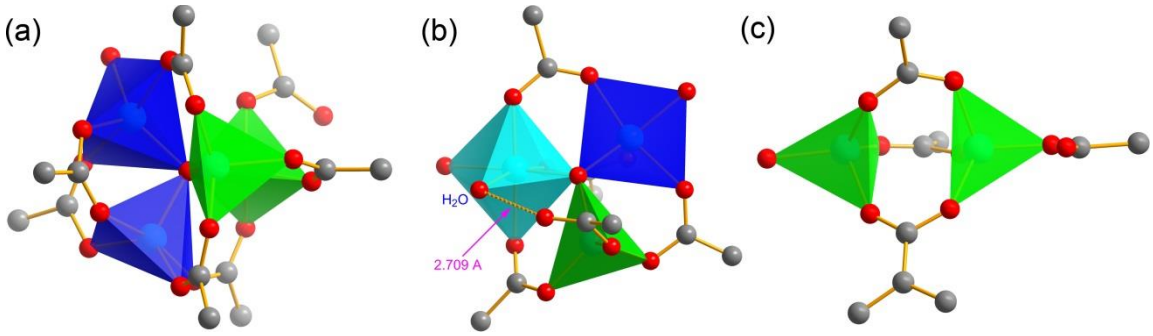

Figure II-4. The three distinctive SBUs in PCN-515, where the green, blue and cyan polyhedra represent 4-, 5- and 6-coordinated Zn, respectively. Color scheme: C, gray; O, red; and Zn, cyan. H atoms were omitted for clarity. The hydrogen bond that exists in $Zn_3(\mu_3\text{-OH})$ cluster is illustrated as a dash line in (b).

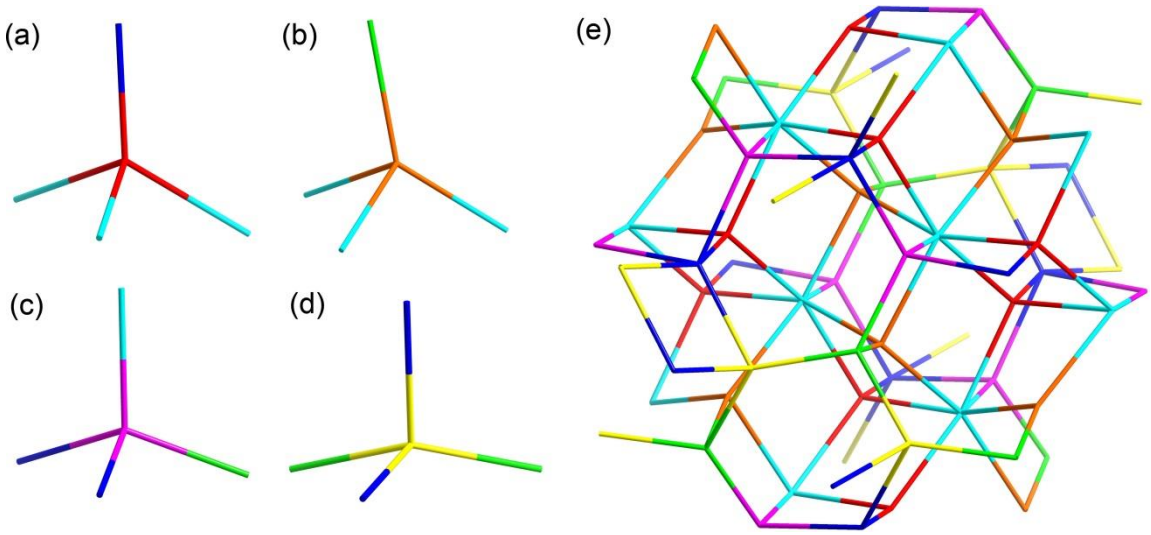

Figure II-5. The topological analysis of PCN-515. (a) – (d) The representation of four topologically distinctive ligands. (e) The representation of PCN-515 topology, where red, orange, magenta and yellow nodes represent four topologically different ligands; and the green, blue, cyan nodes represent the three different SBUs.

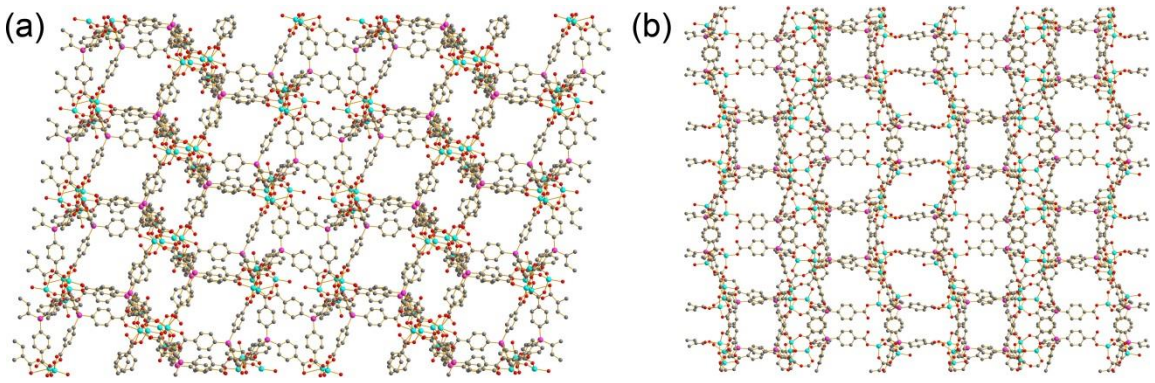

Figure II-6. The crystal structure of PCN-515 along the *b* axis (a) and *c* axis (b). Color scheme: C, gray; O, red; Si, purple; and Zn, cyan. H atoms were omitted for clarity.

The structure of PCN-516. Single crystal XRD reveals that PCN-516 crystallizes in the $P4_2/mmc$ space group where the zinc paddlewheels were connected by tetrahedral ligands. Unlike the copper paddlewheels in PCN-512 (IMP-9) where the distance between the dicopper centers is about 2.66 Å (Figure II-7(a)), the distances between the dizinc centers is about 2.99 Å (Figure II-7(b)), which is consistent with the literature value. [127] Each zinc ion in the paddlewheel is coordinated by a H_2O axially to form a five coordinated metal center. This makes PCN-516 an isostructural MOF with PCN-512 in which the dizinc centers was replaced by dicopper centers. The 4-connected zinc paddlewheels were connected by the tetrahedral ligand to form a 4, 4-connected network with **pts** topology (Figure II-7(c)) denoted as $(4^2 \cdot 8^4)$. The calculated solvent accessible volume of PCN-516 is 73.10% by *PLATON*. [125] The crystal structure shows that it has large channels along the *a* and *b* axis (Figure II-7(d) and (e)).

The structure of PCN-517. Single crystal XRD reveals that PCN-517 crystallizes in the $P\bar{1}$ space group. Its framework has exactly the same connectivity as that of the PCN-514 series, where the Cd_3 clusters were connected by eight tetrahedral ligands to form an anionic framework. This makes it the same framework topology as that of PCN-514, except for the disorder occurring in this framework. Unlike the PCN-514 where all the pores were occupied by the unanchored Cd^{2+} complexes, in PCN-517, the Cd^{2+} counterion can be identified in four different locations, with 25% occupancy for each location in order to balance the negative charge on the framework. This has resulted in additional pore spaces in PCN-517, since not all the pores were blocked by the unanchored Cd^{2+} counterions.

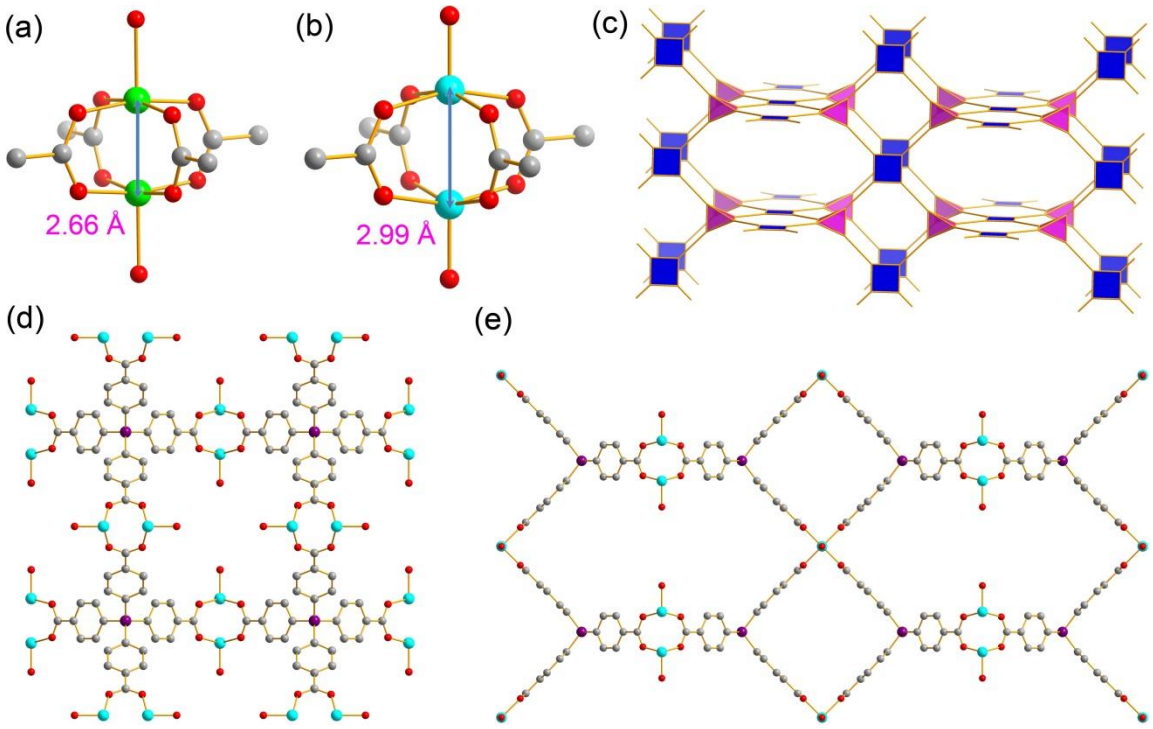

Figure II-7. (a) The representation of a copper paddlewheel. (b) The representation of a zinc paddlewheel. (c) The topology of PCN-512 and PCN-516. (d) The presentation of the crystal structure of PCN-516 along *c* axis. (e) The presentation of the crystal structure of PCN-516 along *a* and *b* axis. Color scheme: C, gray; O, red; Si, purple; Zn, cyan; and Cu, green. H atoms were omitted for clarity.

2.3.2 Porosity and Gas Sorption Study

The microporous nature, good crystal quality, and three dimensional channels of PCN-511/PCN-512 have inspired us to investigate their gas adsorption properties. PCN-511 exhibits a type-I isotherm of N_2 sorption at 77K and 1 bar (Figure II-8(a)) with the Langmuir surface area, [128] BET surface area, [129] and pore volume 794 $m^2 \cdot g^{-1}$, 703 $m^2 \cdot g^{-1}$, and 0.29 $cm^3 \cdot g^{-1}$, respectively. Its H_2 uptake at 77 K and 1.08 bar (810 mmHg) is 133.87

$cm^3 \cdot g^{-1}$ (1.195 wt %, Figure II-8(b)), even without the presence of the unsaturated metal centers (UMCs), which is larger than many other MOFs that have similar BET surface areas. [17] Its CO_2 uptake and CH_4 uptake at 273 K and 1.08 bar are 61.68 $cm^3 \cdot g^{-1}$ and 18.84 $cm^3 \cdot g^{-1}$, respectively (Figure II-8(c) and (d)).

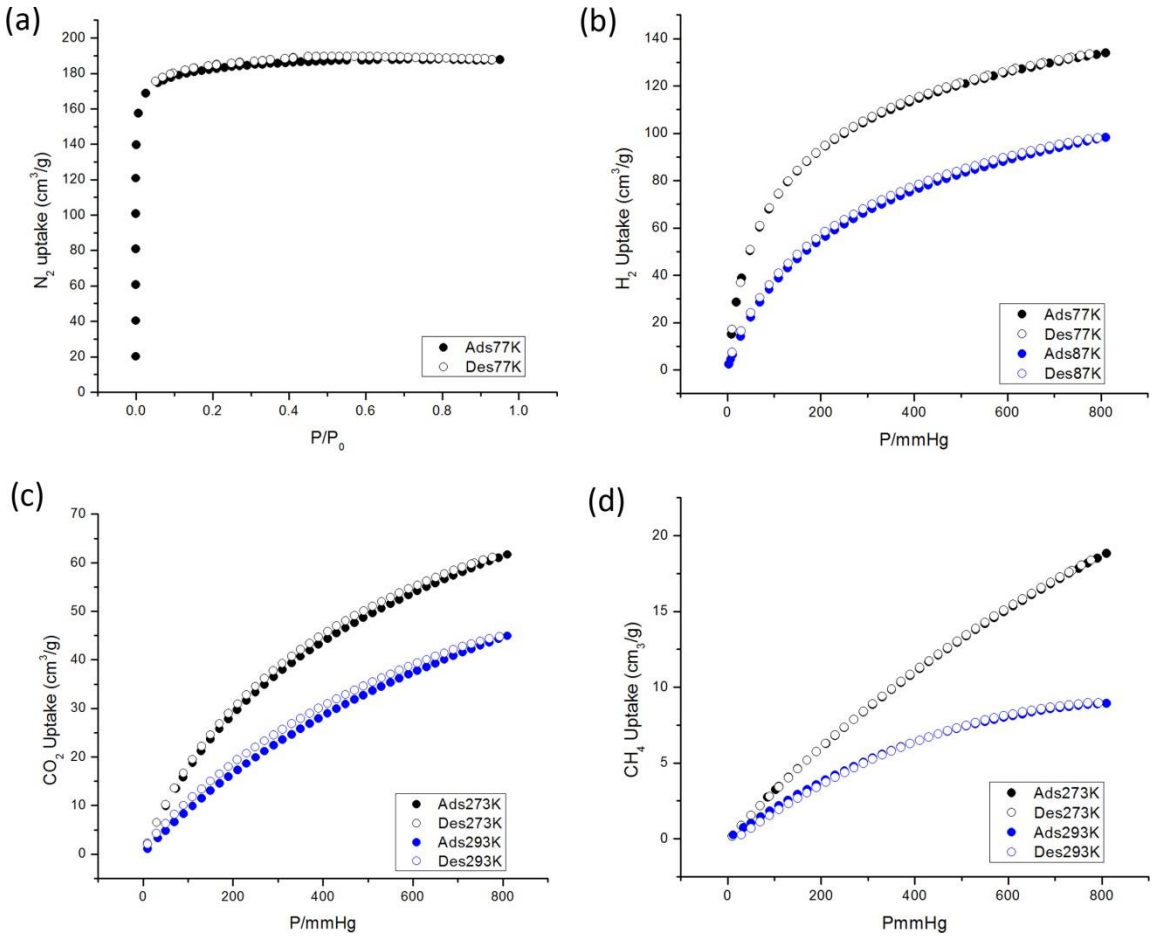

Figure II-8. The gas sorption isotherms of PCN-511 at different temperatures. The closed and open circles correspond to the adsorption and desorption process, respectively.

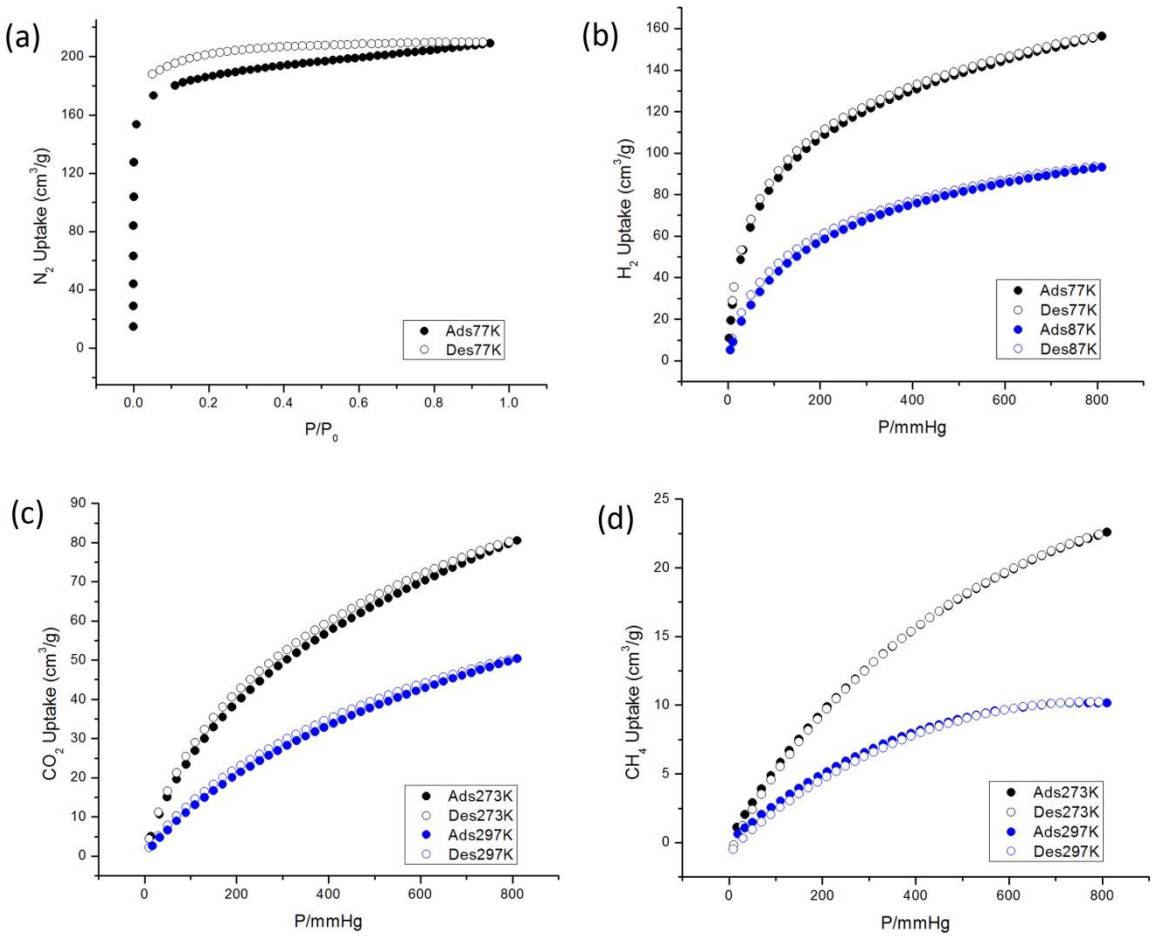

Figure II-9. The gas sorption isotherms of PCN-512 at different temperatures. The closed and open circles correspond to the adsorption and desorption process, respectively.

Differing from the conventional activation method applied to PCN-511, PCN-512 was activated by freeze-thaw activation procedures [64, 124]. After three freeze-thaw cycles, a color change of the crystals was observed from blue to dark purple, probably because of the removal of the axial H_2O ligand and the generation of UMCs. Owing to the existence of the micropores, PCN-512 also exhibits a Type-I isotherm (Figure II-9(a))

with the Langmuir surface area, BET surface area, and pore volume 911 $m^2 \cdot g^{-1}$, 601 $m^2 \cdot g^{-1}$, and 0.32 $cm^3 \cdot g^{-1}$, respectively. Even with a relatively smaller BET surface area, its H_2 uptake at 77 K and 1.08 bar (810 mmHg) is about 156.13 $cm^3 \cdot g^{-1}$ (1.39 wt %, Figure II-9(b)), probably due to the presence of the unsaturated copper centers (Figure II-7(a)). [17] Its CO_2 uptake and CH_4 uptake at 273 K and 1.08 bar are 80.56 $cm^3 \cdot g^{-1}$ and 22.60 $cm^3 \cdot g^{-1}$, respectively (Figure II-9(c) and (d)).

2.4 Summary

By utilizing a silicon-centered, easily-prepared tetrahedral ligand, eight different crystals (PCN-511 – PCN-517, where PCN-514 exists in two forms, PCN-514·DMF and PCN-514·DMA·NMP) were obtained from the solvothermal reactions between the ligand and different metal salts. All the MOFs were structurally and topologically analyzed, where seven of them possess new structures. Their ligand symmetry, porosity, and topology are summarized in Table II-1.

In particular, PCN-515 contains three rarely seen SBUs in the same framework, showing a topology that was never previously observed. Gas adsorption properties were explored on the MOFs that are stable upon removal of residual solvents. PCN-512 has a BET surface area of 601 $m^2 \cdot g^{-1}$ and H_2 uptake of 1.39 wt % weight percent at about 1 bar and 77 K, which shows some promise for industrial applications of gas storage due to both its low synthetic cost and its relatively large gas uptake.

Table II-1: Summary of all the aforementioned MOFs with their porosity and topology

MOF	Ligand Symmetry	Space Group	Ionic Frame-work	Solvent Accessible Volume [a]	BET ($m^2 \cdot g^{-1}$)	Topology	Schläfli Symbols
PCN-511	C_1	$C2/c$	No	45.6	703	**alb/P**	$(4^4 \cdot 6^2)_2(4^8 \cdot 6^{17} \cdot 8^3)$
PCN-512	D_{2d}	$P4_2/mmc$	No	72.7	601	**pts**	$(4^2 \cdot 8^4)$
PCN-513	C_1	$P\bar{1}$	No	44.1	N/A	**flu**	$(4^{12} \cdot 6^{12} \cdot 8^4)(4^6)_2$
PCN-514·DMF	C_1	$P\bar{1}$	Yes	52.4	N/A	**flu**	$(4^{12} \cdot 6^{12} \cdot 8^4)(4^6)_2$
PCN-514·DMA	C_1	$P\bar{1}$	Yes	52.4	N/A	**flu**	$(4^{12} \cdot 6^{12} \cdot 8^4)(4^6)_2$
PCN-515	C_1, C_1, C_1, C_1 [b]	$P2_1/c$	No	70.5	N/A	[c]	$(4 \cdot 6^5)_2(4^3 \cdot 6^3)(4^3 \cdot 6^6 \cdot 8)$ $(4^4 \cdot 6^2)(4^5 \cdot 6)(4^9 \cdot 6^9 \cdot 8^3)$
PCN-516	D_{2d}	$P4_2/mmc$	No	73.1	N/A	**pts**	$(4^2 \cdot 8^4)$
PCN-517	C_1	$P\bar{1}$	Yes	N/A [d]	N/A	**flu**	$(4^{12} \cdot 6^{12} \cdot 8^4)(4^6)_2$

[a] Calculated by *PLATON*.

[b] Four topologically different ligands exist in this MOF.

[c] This topology is not assigned with a name yet.

[d] The solvent accessible volume was not calculated due to the existence of disorder in this structure.

CHAPTER III

SYMMETRY-GUIDED SYNTHESIS OF HIGHLY POROUS METAL-ORGANIC FRAMEWORKS WITH FLUORITE TOPOLOGY [*]

3.1 Introduction

In the past two decades, the exploration of MOFs has been one of the most rapidly developing areas in chemistry due to their structural diversity and great potential for various applications. While a great amount of effort has been made to achieve high porosities [105, 110, 130, 131] and specific framework functionalities [132], rational design of MOFs with desired characteristics still remains challenging. [43, 49, 133, 134] Symmetry-guided design of MOFs typically involves the selection of metal building units and organic ligands that are symmetrically complementary to each other for the purpose of forming a three dimensional network with large cavities and desired topology. Traditional cases of symmetry-guided designs usually involve the extension of the size of the organic linkers based on an existing structure, expecting to obtain an isoreticular framework with the same topology but larger porosity. [41] However, the elongation of MOF constructional units will inherently undermine the stability of the framework and, in many cases, result in undesired framework interpenetration. [41] In fact, framework stability and undesired self-interpenetration are the two primary concerns in the construction of highly porous MOFs with elongated ligands.

[*] Reproduced in part with permission from "Symmetry-Guided Synthesis of Highly Porous Metal–Organic Frameworks with Fluorite Topology", by Zhang, M.; Chen, Y.-P.; Bosch, M.; Gentle, T.; Wang, K.; Feng, D.; Wang, Z. U.; Zhou, H.-C., *Angew. Chem. Int. Ed.* **2014,** *53*, 815-818, copyright 2014 by John Wiley & Sons.

A careful inspection of the net topology of simple mineral structures may provide novel insights into the rational design of MOFs. The study on MOF topology has recently gained an increasing amount of attention, because of both its importance in understanding the framework structure from the fundamental level [58] and its close connection with the framework porosity, stability and possibility of interpenetration [59]. In this work, we have demonstrated a successful implementation of symmetry-guided design of stable, non-interpenetrated MOFs with the expected topology. Herein, we report two MOFs, PCN-521 and PCN-523, both of which are highly porous frameworks with large cavities. They are the first examples of Zr/Hf MOFs constructed from tetrahedral ligands. In particular, PCN-521 has the largest surface area, pore size and solvent accessible volume among all the MOFs from tetrahedral ligands. They are the first examples of Zr/Hf MOFs with tetrahedral linkers.

3.2 Experimental Section

3.2.1 Materials and Instrumentation

The tetrakis(4-bromophenyl)methane was synthesized according to the reported procedures.[111] The 4-(methoxycarbonyl)phenylboronic acid was purchased from AK Scientific Inc. The tetrakis(triphenylphosphine)palladium(0) was purchased from Pressure Chemical Co. The Cesium fluoride (CsF), dimethoxyethane (DME), *N*,*N'*-dimethylformamide (DMF), *N*,*N'*-dimethylacetamide (DMA), *N*,*N'*-diethylformamide (DEF), chloroform ($CHCl_3$), trifluoroacetic acid (CF_3COOH), benzoic acid, acetone, zirconium(IV) chloride ($ZrCl_4$), hafnium chloride ($HfCl_4$) tetrahydrofuran (THF) and

methanol were purchased from VWR. All commercial chemicals were used without further purification unless otherwise mentioned. ^{1}H nuclear magnetic resonance (NMR) data were recorded on a Mercury 300 MHz NMR spectrometer at the Center for Chemical Characterization and Analysis (CCCA), Department of Chemistry, Texas A&M University. Fourier transform infrared spectroscopy (FTIR) data were collected using a SHIMADZU IRAffinity-1 FTIR Spectrophotometer.

Powder X-ray diffraction (PXRD) was carried out with a BRUKER D8-Focus Bragg-Brentano X-ray Powder Diffractometer equipped with a Cu sealed tube (λ = 1.54178) at 40 kV and 40 mA. Thermogravimetric analyses (TGA) were performed on a SHIMADZU TGA-50 Thermogravimetric Analyzer with a heating rate of 5 ℃·min^{-1} under N_2. Gas sorption measurements were conducted using a Micrometritics ASAP 2020 system at different temperatures. The simulated PXRD spectra were acquired by the diffraction-crystal module of the *Mercury* program based on the single crystal data. The program is available free of charge *via* internet at http://www.iucr.org.

3.2.2 Ligand Synthesis

The ligand H_4**MTBC** (4′,4″,4‴,4⁗-methanetetrayltetrabiphenyl-4-carboxylic acid) was synthesized based on previous literature [64] with some modifications, which are illustrated in Scheme III-1.

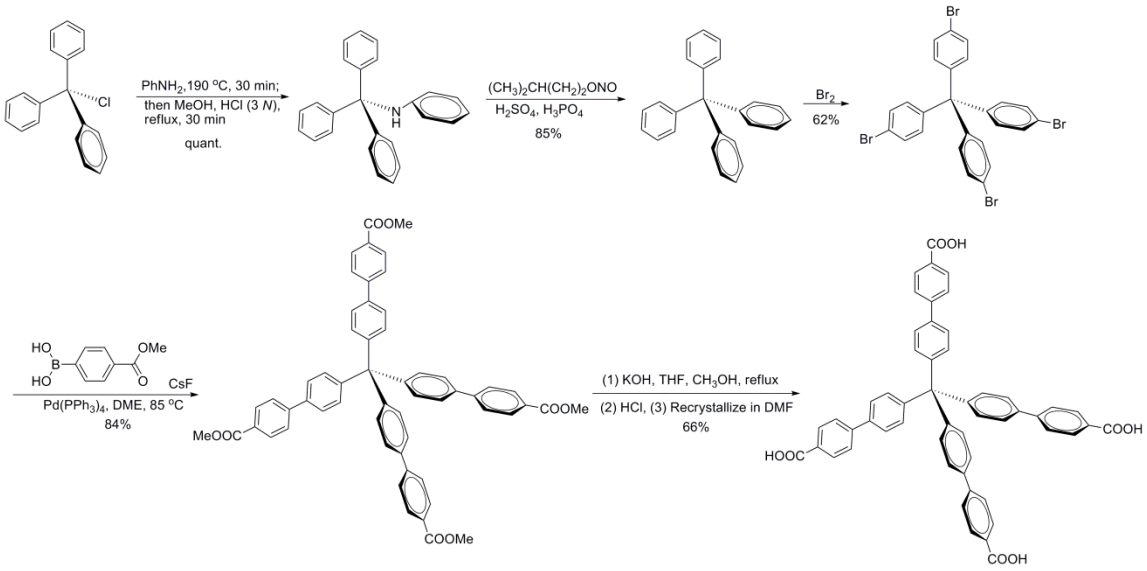

Scheme III-1. The synthesis of H_4**MTBC** ligand.

Synthesis of tetramethyl 4′,4″,4‴,4⁗-methanetetrayltetrabiphenyl-4-carboxylate. Tetrakis(4-bromophenyl)methane was synthesized according to a reported procedure. [111] Tetrakis(4-bromophenyl)methane (2.4 g, 4 mmol), 4-(methoxycarbonyl) phenylboronic acid (1.8 g, 5 mmol), Tetrakis(triphenylphosphine)palladium(0) ($Pd(PPh_3)_4$, 300 mg) and CsF (3.8 g, 12.5 mmol) were charged in a 500 mL round bottom flask equipped with a condenser. The flask was pumped under vacuum and refilled with N_2 for three times. Freshly degassed dimethoxyethane (DME, 300 mL) were carefully added to the flask through a cannula. The resulting mixture was stirred and heated up at 85 ˚C for 3 days under nitrogen atmosphere. After cooling to room temperature, the solution was evaporated under vacuum and the resulting residue was dissolved in 300 mL $CHCl_3$. Filtration through Celite provided a green-yellowish solution, which was washed with water three times and brine once. The aqueous layer

was back-extracted with chloroform and the combined organic layers were dried over $MgSO_4$ and filtered. The solvent was removed and the crude product was dissolved in 30 mL acetone under ice-water bath. Tetramethyl 4′,4″,4‴,4⁗-methanetetrayltetrabiphenyl-4-carboxylate was obtained as an off-white solid by filtration and dried in vacuum (2.8 g, 84%) whose purity is good enough to perform the following experiment. An analytical sample was obtained by column chromatography on silica gel with 3:7 EtOAc/Hexane to give this compound as a pale yellow solid. ^{1}H NMR (300 MHz, DMSO-d_6): δ = 8.03 (d, 8H), 7.85 (d, 8H), 7.77 (d, 8H), 7.42 (d, 8H), 3.86 (s, 12H).

Synthesis of 4′,4″,4‴,4⁗-methanetetrayltetrabiphenyl-4-carboxylic acid. Tetramethyl 4′,4″,4‴,4⁗-methanetetrayltetrabiphenyl-4-carboxylate (3.15 g, 3.6 mmol), 3 g NaOH, 120 mL THF, 80 mL water and 80 mL MeOH were mixed in a 500 mL round bottom flask equipped with a condenser. The mixture was refluxed overnight and then cooled down to room temperature. The solution was evaporated under vacuum at 40˚C to remove THF and MeOH, and the residue was acidified with 2 M HCl till pH=1. The white solid was obtained by filtration, washed with water and dried in a vacuum. The final product was obtained as a white powder after a recrystallization in DMF (2.03 g, 66%). ^{1}H NMR (300 MHz, DMSO-d_6): δ = 8.01 (d, 8H), 7.82 (d, 8H), 7.77 (d, 8H), 7.42 (d, 8H).

3.2.3 MOF Synthesis

Synthesis of PCN-521, $[Zr_6(\mu_3\text{-}OH)_8(OH)_8](MTBC)_2$. Phase pure single crystals of PCN-521 that are suitable for single crystal X-ray Diffraction (XRD) were

synthesized by the following route. $ZrCl_4$ (12 mg), H_4**MTBC** (10 mg) and benzoic acid (350 mg) were ultrasonically dissolved in 1.7 mL of DEF in a 3 mL Pyrex vial. The mixture was then heated in a 120 ℃ oven for 24 h. Large, colorless, distorted-octahedron-shaped single crystals of PCN-521 were yielded. A larger amount of PCN-521 samples were obtained by the same solvothermal condition with benzoic acid or trifluoroacetic acid in a 20 mL Pyrex vial. Trifluoroacetic acid is preferred to prepare MOF samples for gas sorption purposes since it is easier to be removed from the MOF cavities during the activation process. The purity of this MOF can be preliminarily checked by the observation of the crystal shapes and further substantiated by Powder X-ray Diffraction (PXRD). FTIR (KBr): = 3570 (w), 3520 (m), 2340 (m), 2313 (s), 1674 (m), 1508 (s), 1396 (s), 789 (m), and 725 (m).

Synthesis of PCN-523, $[Hf_6(\mu_3\text{-}OH)_8(OH)_8](MTBC)_2$. Phase pure single crystals of PCN-523 that are suitable for single crystal X-ray Diffraction (XRD) were synthesized by the following route. $HfCl_4$ (75 mg), H_4L (50 mg) and benzoic acid (1750 mg) were ultrasonically dissolved in 8.5 mL of DEF in a 20 mL Pyrex vial. The mixture was then heated in a 120 ℃ oven for 24 h. After cooling down to room temperature, colorless distorted-octahedron-shaped crystals were harvested by filtration. (53 mg, 58% yield). The purity of this MOF can be preliminarily checked by the observation of the crystal shapes and further substantiated by PXRD. FTIR (KBr): = 3500 (w), 2334 (m), 2295 (s), 1614 (s), 1504 (m), 1373 (m), 793 (m), and 752 (m).

3.2.4 Single Crystal Crystallography of PCN-521 and PCN-523

A transparent distorted-octahedron (PCN-521) / distorted-octahedron (PCN-523) crystal was taken from the solution directly, transferred into oil and mounted onto a loop for single crystal X-ray data collection. Diffractions were measured on a Bruker Smart Apex diffractometer equipped with a Mo-Kα sealed-tube X-ray source (λ = 0.71073 Å, graphite monochromated) and a cooling device (110 K). The data frames were recorded using the program APEX2 and processed using the program *SAINT* routine within APEX2. The data were corrected for absorption and beam corrections based on the semi-empirical technique as implemented in *SADABS*. The structures were solved by direct method using *SHELXS* and refined by full-matrix least-squares on F^2 using *SHELXL* software. [135]

For the refinement of PCN-521, intensity data was integrated in tetragonal crystal system. While applying data to *XPREP*, it was shown that the R(sym) is 0.149 for highest symmetric Bravais lattice, Tetragonal I. In case of Tetragonal I crystal system, *XPREP* listed 8 space groups. *I*4/*m* was the best candidate with the lowest CFOM factor (5.67), whereas *I*4/*mmm* was the second centrosymmetric choice (CFOM = 14.64). By using these two space groups, we obtained R value is 0.2151 for *I*4/*m*, and R value is 0.2274 for *I*4/*mmm*, respectively, before *SQUEEZE*. Slightly better R value was given by the solution with *I*4/*m* space group, which should be assigned for this structure. Similarly, same *I*4/*m* space group was employed with the lowest centrosymmetric CFOM factor (6.05) for PCN-523. These two crystals, PCN-521 and PCN-523 are isostructural.

For the refinements of both PCN-521 and PCN-523, all carbon atoms were refined with the help of EADP restrains on each ligand to clear the warnings about non-positive definite matrices. All non-hydrogen atoms were refined with anisotropic displacement parameters during the final cycles. Organic hydrogen atoms were located in calculated positions with isotropic displacement parameters set to 1.2 × U_{eq} of the attached atoms. The solvent molecules were highly disordered, and attempts to locate and refine the solvent peaks were unsuccessful. Contributions to scattering due to these solvent molecules were removed using the *SQUEEZE* routine of *PLATON*; [136] structures were then refined again using the data generated. The contents of the solvent region are not represented in the unit cell contents in the crystal data.

The detailed information about the solution and refinement of the single crystal structures of PCN-521 and PCN-523 can be found in the supporting information of this manuscript. [48] The CIF files can be obtained free of charge from the Cambridge Crystallographic Data Centre *via* www.ccdc.cam.ac.uk/data_request/cif with assigned deposition numbers 956577 for PCN-521, 956576 for PCN-523.

3.2.5 Topological Analysis

All the topological analyses of the crystal structures were performed by using *TOPOS 4.0* Professional. The analysis of PCN-521 is very straightforward since there are no disorders or entanglements involved in this structure. After loading the structure cif file in the *TOPOS* program, the adjacent matrix was calculated by the *AutoCN* module. After removing all the 0-coordinated and 1-coordinated atoms, the structure was

divided into clusters by using the *ADS* module; then followed by a simplification of the network by running the *ADS* module again. After removing all the 2-coordinated atoms in the simplified network, the topology analysis can be performed based on the simplified network. (Figure III-1)

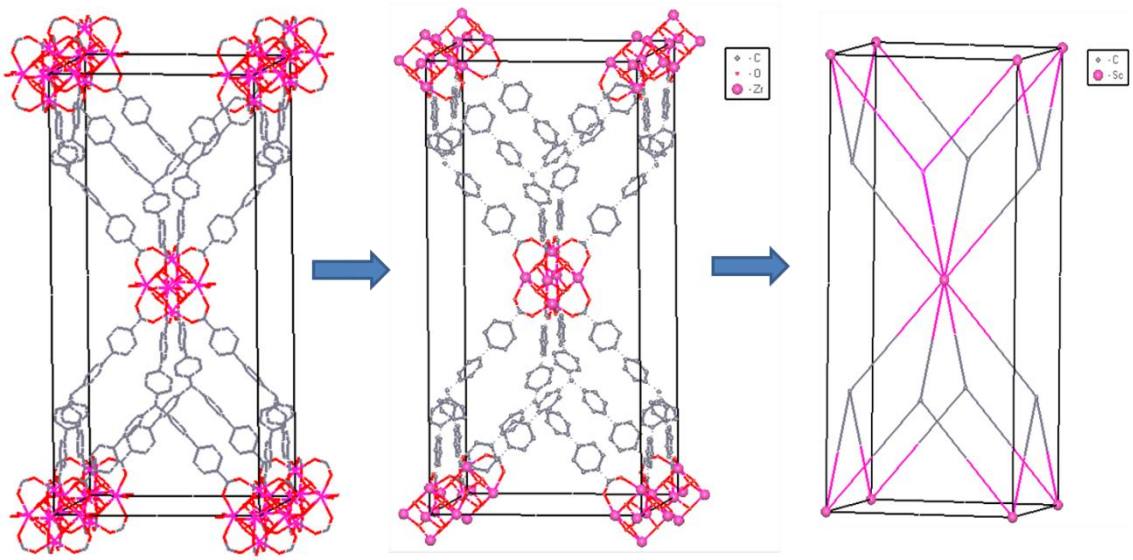

Figure III-1. The topological analysis of the network of PCN-521. The topological representation of PCN-521 was illustrated on the right, where the gray and magenta nodes represent the 4-connected tetrahedra and 8-connected cube, respectively.

PCN-523 is an isostructural framework to PCN-521 except that minor disorder occurs on the central phenyl rings of the tetrahedral ligands. Its structure was directly loaded into the *TOPOS* program without removal of disorder, and the topological analysis was performed in the same way as that of PCN-521. Both PCN-521 and PCN-523 are 4, 8-connected networks of fluorite topology.

3.2.6 Activation Procedures and Gas Sorption Measurements

The fresh PCN-521/PCN-523 samples must be activated prior to any gas sorption measurements. In order to remove any unreacted starting materials, inorganic compounds and trapped benzoic acid in its pores, the as-synthesized PCN-521 (~50 mg) / PCN-523 (~100 mg) samples was treated with ~40 mL DMA at 100 ℃ for 12 h. The solvent was immediately decanted when it was still hot and another 40 mL DMF was replenished immediately. The sample was subsequently treated with solvent exchange, with DMA 6 times and acetone 6 times, and each time for about 12 h. After the carefully removal of acetone by decanting, the sample was transferred into a sorption tube and activated under dynamic vacuum at room temperature for 6 h. It was activated by using the 'outgas' function of the adsorption instrument for 10 h at 100 ℃ prior to any gas adsorption/desorption measurements.

3.3 Results and Discussion

3.3.1 Symmetry-Guided Synthesis of Highly Porous MOFs

The fluorite topology [68, 70, 137] is especially intriguing for the construction of highly porous materials. The structure can be conceived as a cubic close packing (ccp) of the calcium cations (Ca^{2+}) in which the fluoride anions (F^-) fill in all its tetrahedral interstitial cavities (Figure III-2(a)), leaving all the octahedral interstitial cavities unoccupied (Figure III-2(b)). Materials with larger octahedral cavities can be generated by augmenting the 4-connected nodes with a rigid tetrahedral ligand (Figure III-2(c)), which are connected by the 8-connected metal SBUs. This MOF can be conceived as the

cubic close packing of the metal clusters where all the tetrahedral interstitial cavities are "occupied" by the ligands, and all the octahedral interstitial cavities should remain empty (Figure III-2(d)). Additionally, frameworks with this topology cannot undergo a translation in any direction without overlapping with itself, and thus cannot exhibit self-interpenetration. The large unoccupied octahedral interstitial cavities and the non-interpenetrated nature of the fluorite topology have made it especially attractive for MOF construction.

The Yaghi [62, 63], Lin [65-67], Kim [70], Long [68], Schroder [69], Suh [71], Shimizu [72] groups and our group [52, 138, 139] have prepared MOFs from tetrahedral ligands for structural or gas-adsorption studies, but most of the resulting MOFs suffer from limited surface areas, small pore sizes and undesired interpenetration (See Table III-1). It is suggested that these limitations result from symmetry incompatibility between the tetrahedral ligands and the metal SBUs utilized in the framework. A close examination of the fluorite structure reveals that the utilization of an 8-connected metal SBU is of key importance for the construction of a framework with the desired topology.

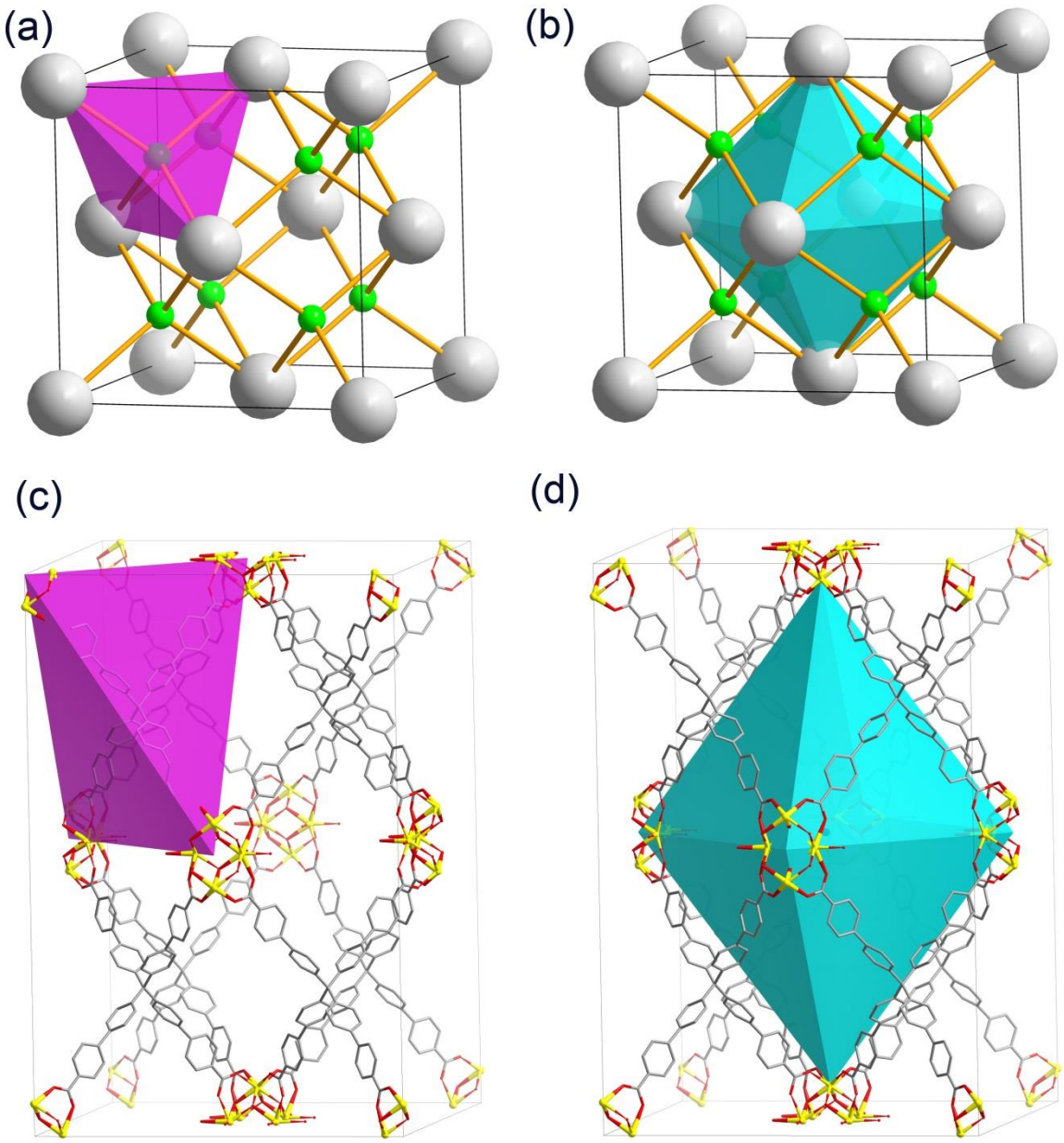

Figure III-2. (a) A representation of the fluorite structure where the fluoride anions fill all the tetrahedral interstitial cavities. (b) The unoccupied octahedral interstitial cavities in the fluorite structure. (c) The augmentation of the tetrahedral node of fluorite structure results in a framework with the same topology but larger pores. (d) The representation of an octahedral cavity in PCN-521 with the size of 20.5 × 20.5 × 37.4 Å.

Zirconium polyoxo clusters have attracted our attention as SBUs for several reasons. First, zirconium is a metal which is about three times more abundant in the earth's crust than the other commonly used metals, such as copper and zinc. [86] Second, the employment of high-valence metals will considerably increase the chemical stability of the framework. Even though the list of existing porous MOFs with trivalent metals (such as Al^{3+}, Fe^{3+}, Cr^{3+}, In^{3+}, *etc.*) is still short, the structures based on M^{4+} (such as Zr^{4+}, Hf^{4+}, Ti^{4+}, *etc.*) cations are even rarer. [140] There are a limited number of reported Zr MOFs [53, 87, 141-143], but they have demonstrated their high stability to air, water, [87] and even concentrated acid [141]. Third, and most importantly, the Zr clusters have the appropriate connectivity for the construction of MOFs with fluorite topology. So far, So far, 12-connected, [87, 142, 143] 8-connected [48, 53, 141] and 6-connected Zr_6O_8 clusters [144] were identified in a variety of stable MOFs. (Figure III-3) Unlike the commonly-seen 12-connected Zr_6O_8 clusters encountered in the UiO-66 series [87], 8-connected Zr_6O_8 clusters were recently reported in PCN-222 (MOF-545), [53, 141] which was obtained by using a monocarboxylate as a modulating reagent. Following a similar synthetic route with tetrahedral ligands has provided us the desired MOFs.

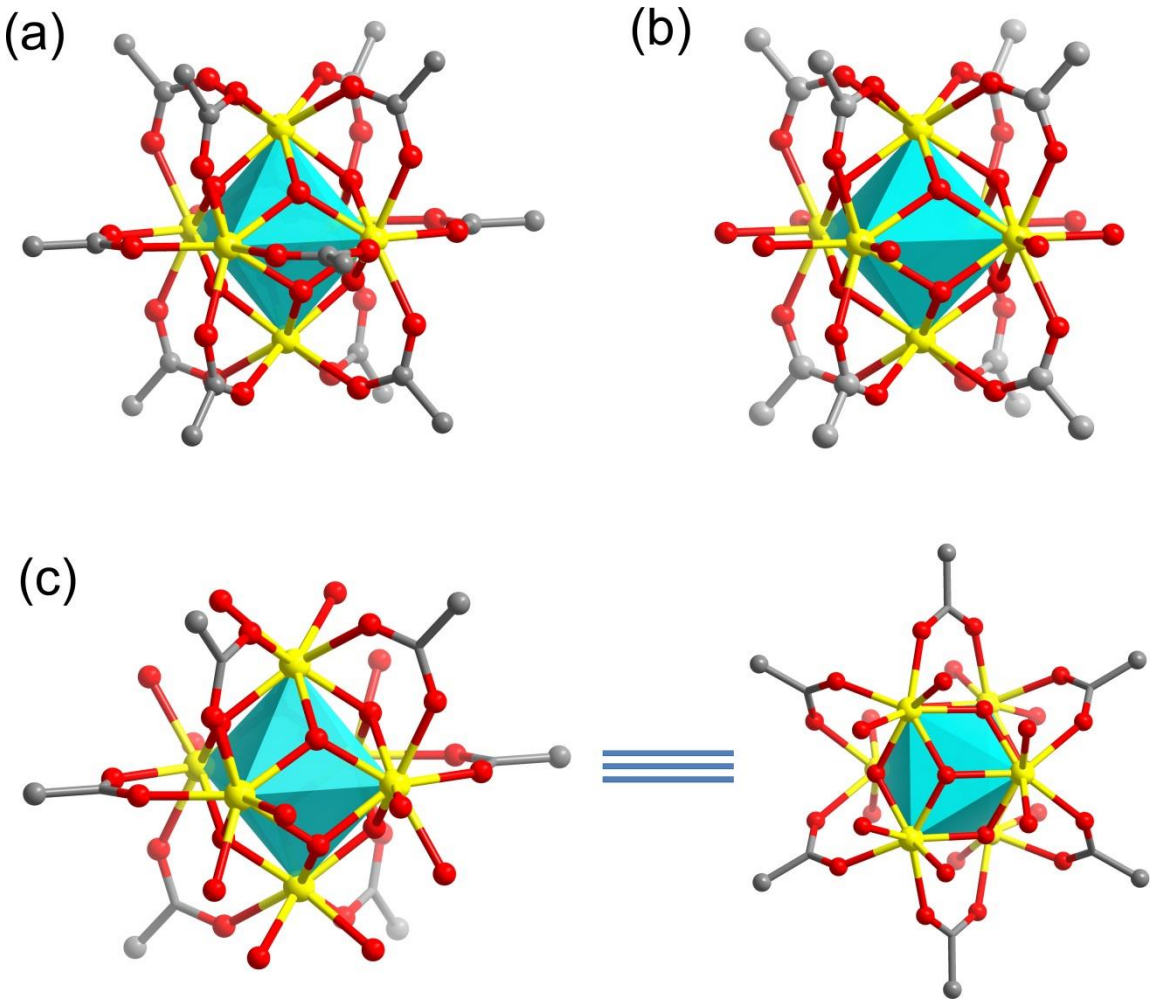

Figure III-3. Different connectivities of Zr_6O_8 clusters. (a) 12-connected; (b) 8-connected; (c) 6-connected (left: side view; right: top view). Color scheme: C, gray; O, red; and Zr, yellow. The cyan polyhedra represent the octahedral geometry of the Zr_6O_8 cluster.

Colorless octahedral single crystals (Figure III-6(a)) of PCN-521 $[Zr_6(\mu_3\text{-}OH)_8(OH)_8)](MTBC)_2$ were obtained by a solvothermal reaction of $ZrCl_4$ and H_4**MTBC** in *N*, *N'*-diethylformamide (DEF) in the presence of benzoic acid or trifluoroacetic acid

at 120 ˚C for 24h. Single crystal X-ray diffraction studies reveal that PCN-521 crystallizes in the tetragonal space group *I*4/*m*, which is constituent with its crystal shape (a distorted octahedron). This framework consists of the 8-connected Zr_6O_8 clusters (Figure III-4(a)) linked by tetrahedral ligands (Figure III-4(b)). Similar to the clusters in PCN-222 (MOF-545) [53, 141], the symmetry of Zr_6O_8 clusters is reduced from O_h to D_{4h}. It is this symmetry reduction that has made this SBU symmetrically-compatible with the tetrahedral ligands, resulting in a framework with the cavities as large as 20.5 × 20.5 × 37.4 Å (Figure III-2(d)). On the other hand, the tetrahedral ligand MTBC has lost its C_3 proper rotational axes by distorting the angles of its two arms from 109˚28' to 87.16˚ and 121.65˚ but has retained its S_4 improper rotational operations (Figure III-4(b)), and thus the ligand symmetry was reduced from T_d to D_{2d}. It is the combination of the D_{4h} and D_{2d} symmetries that has resulted in the crystal space group *I*4/*m*, where the two phenyl rings of MTBC ligand rotate 41.76° from each other to meet the directionality of the 8-connected Zr_6O_8 SBU (Figure III-5). As expected, the tetrahedral ligands link to the Zr SBUs in a 2:1 ratio to form a 4,8-connected net with the fluorite (**flu**) topology [68, 70, 137] denoted as $(4^{12}\cdot 6^{12}\cdot 8^4)(4^6)_2$. (Figure III-4(c)) It should be noted that a few other coordination polymers with the **flu** topology were previously reported without providing evidence of the existence of potential voids (See Table III-1). According to the latest IUPAC definition, MOFs are infinite crystalline coordination networks with potential inner porosity. [13] The calculated solvent accessible volume of PCN-521 is 78.50% by *PLATON* platform, [125] indicating its significantly porous nature, which is further substantiated by the subsequent gas sorption measurements. Like the other zirconium-

based MOFs, PCN-521 is also resistant to air and water, despite the large channels in the framework. The thermal decomposition of PCN-521 starts at 500˚C, which indicates this MOF has high thermal stability as well.

The successful synthesis of PCN-521 has provided a general way of making stable, non-interpenetrated MOFs with large porosities. New structures can be obtained by varying both the organic linkers and the metal SBUs. An isostructural MOF, PCN-523, was obtained by replacing the 8-connected Zr_6O_8 clusters with Hf_6O_8 clusters. Colorless, distorted-octahedron-shaped single crystals of PCN-523 $[Hf_6(\mu_3\text{-}OH)_8(OH)_8](MTBC)_2$ were synthesized from a similar solvothermal reaction of $HfCl_4$ and H_4**MTBC** in DEF. Gas sorption measurements were also performed on PCN-523 after phase-pure single crystals were obtained via modulated synthesis. The calculated solvent accessible volume of PCN-523 is 77.90% by *PLATON* platform. [125] The size of its octahedral cavity is 22.1 × 22.1 × 35.3 Å. It should be noted that this Hf MOF also possesses high chemical and thermal stability. Due to the non-interpenetrated nature of fluorite-topology framework, it is suggested that further elongation of the tetrahedral ligands may result in MOFs with even larger cavities. This work is currently in progress in our group.

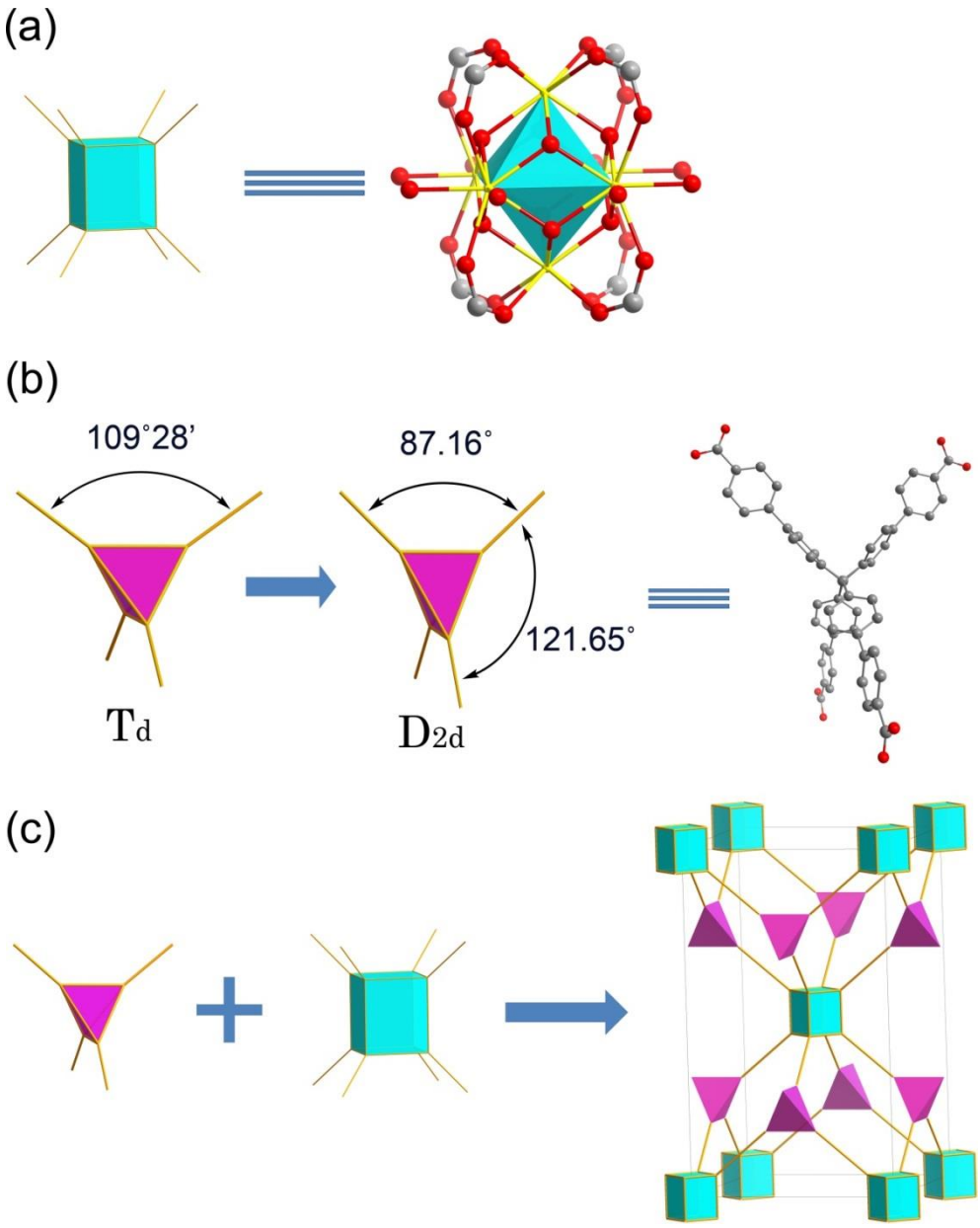

Figure III-4. (a) The 8-connected Zr_6O_8 cluster in PCN-521 and its topological representation. Color Scheme: C, gray; O, red; Zr, yellow. (b) The distortion of the conformation of the tetrahedral ligand in PCN-521 and its topological representation. (c) The augmented fluorite topology of PCN-521, where the pink and cyan polyhedra represent 4- and 8-connected nodes, respectively.

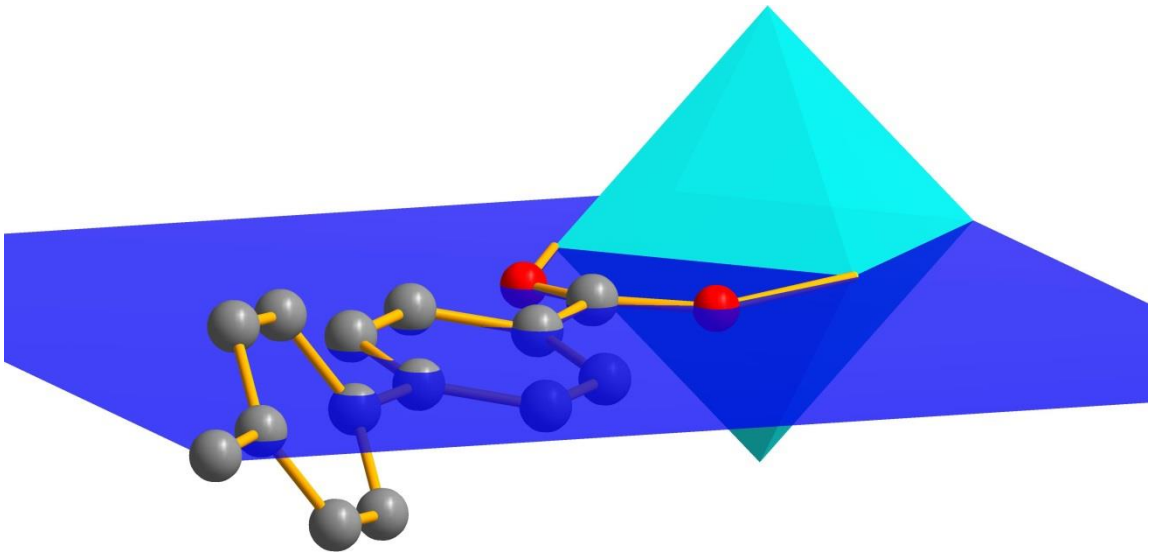

Figure III-5. In PCN-521, the two phenyl rings in the tetrahedral ligand have to rotate 41.76˚ to meet the directionality of the Zr_6O_8 cluster. The cyan octahedron represents a Zr_6O_8 cluster. Color Scheme: C, gray; O, red.

Another MOF, PCN-522, was synthesized by carefully tuning the solvothermal reaction conditions. Unlike the distorted-octahedron-shaped crystals of PCN-521, this MOF crystallizes in a truncated octahedron shape (Figure III-6(b)). Single crystal X-ray diffraction studies reveal that PCN-522 crystallizes in cubic space group $Im\bar{3}m$ with the formula $[Zr_8(\mu_4\text{-}O)_6]_2[Zr_6(\mu_3\text{-}OH)_4(\mu_3\text{-}O)_4]_6(MTBC)_{24}$. Its space group is consistent with its truncated octahedron shape, which inherently has a cubic symmetry. PCN-522 consists of two distinct Zr clusters, a normal 12-connected Zr_6O_8 cluster (which is similar to the clusters in UiO-66 [87]) and a rarely seen 12-connected Zr_8O_6 cluster. To the best of our knowledge, PCN-221 is the only MOF that possesses the same metal cluster. [145] Topologically, these two Zr polyoxo clusters are different, as the former represents a

12-connected cuboctahedron (Figure III-7(a)) and the latter represents a 12-connected icosahedron (Figure III-7(b)). The two different Zr clusters were connected by the tetrahedral linkers to form a 4,12,12-connected network with a topology denoted as $(4^{28}\cdot6^{32}\cdot8^{6})_3(4^{30}\cdot6^{30}\cdot8^{6})(4^{6})_{12}$ (Figure III-7(c)). This is the first reported example of observed topology that connects tetrahedra, cuboctahedra and icosahedra in the same network. The calculated solvent accessible volume of PCN-522 is 72.80% by using the *PLATON* platform, [125] which implies that there should be enough space to accommodate the charge-balancing counterions to balance the positively-charged $[Zr_8O_6(CO_2)_{12}]^{8+}$ cluster in the framework.

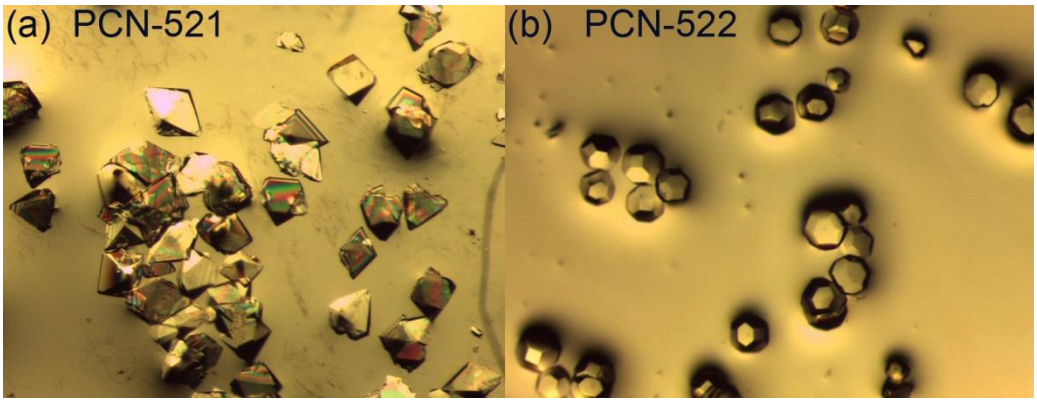

Figure III-6. Microscopic images of (a) the distorted-octahedron-shaped PCN-521 and (b) the truncated-octahedron-shaped PCN-522.

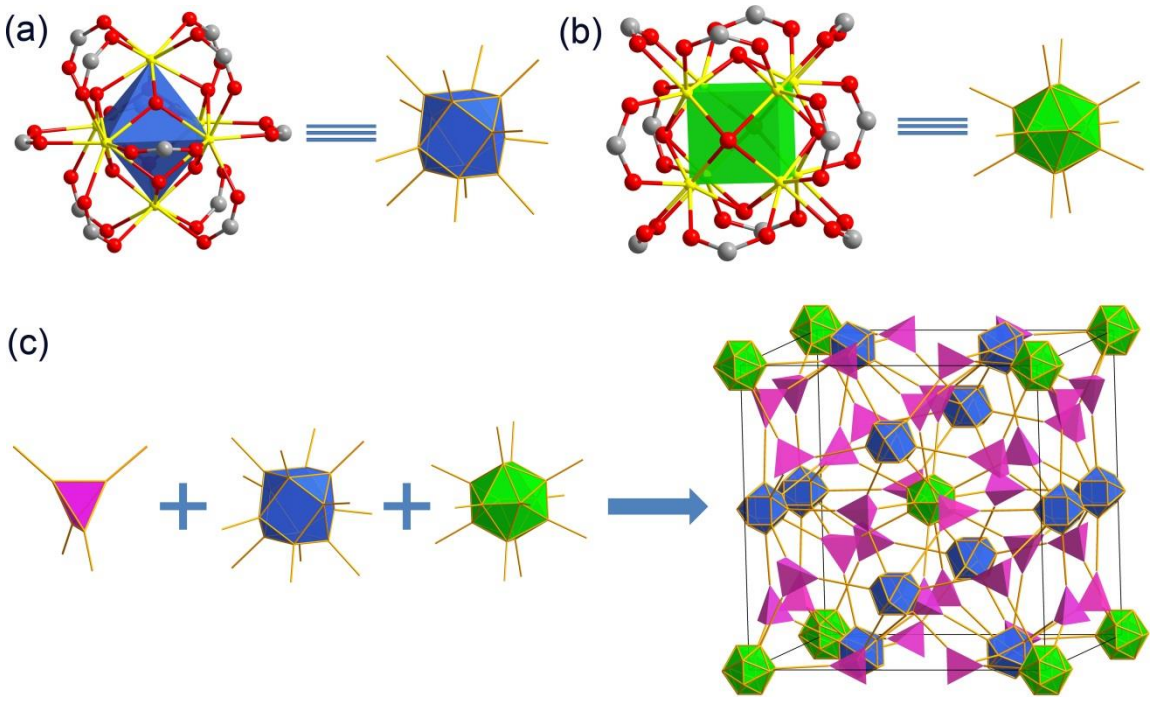

Figure III-7. (a) The 12-connected Zr_6O_8 cluster in PCN-522. (b) The 12-connected Zr_8O_6 cluster in PCN-522. (c) The topological representation of PCN-522.

3.3.2 Modulated Synthesis of MOFs with High-Valence Metal Clusters

Despite the excellent stability of Zr MOFs, one of their primary drawbacks is that the crystallinity and single crystal quality are usually extremely low. The high charge density (Z/r) of Zr^{4+} strongly polarizes the resulting Zr–O bond and thus it has a considerable amount of covalent character, which makes the ligand exchange reactions between Zr clusters and carboxylates extraordinarily slow. This makes it difficult to obtain single crystals in this system. Recent research indicates that the crystal size, quality and morphology can largely affect the surface area of the resulting MOFs. In order to overcome this difficulty and obtain phase-pure single crystals, modulated

synthesis of Zr MOFs was employed by introducing a quantitative amount of modulating reagent, such as benzoic acid or trifluoroacetic acid, to the solvothermal system. [142] Similar as was reported, the presence of the modulating reagent can greatly affect the size, quality and purity of the resulting crystals. In this work, a larger amount of benzoic acid will reduce the crystal size of PCN-521/PCN-523 but improve the crystal purity. The amount of modulating reagent should be carefully tuned to optimize the quality of the products.

The difference between PCN-521 and PCN-522 results from the two different conformations of the tetrahedral ligands combined with three distinct zirconium SBUs. The presence of modulating reagent also plays a critical role in controlling the product formation, presumably because the presence of modulating reagent will affect the kinetics of the framework formation. [146, 147] PCN-522 can be obtained when the concentration of benzoic acid is relatively lower while the formation of PCN-521 requires a larger amount of benzoic acid. It is suggested that larger amounts of benzoic acid can reduce the ligand exchange rate and thus the Zr clusters with fewer connections are favored. PCN-521 consists of only one type of Zr cluster to which all four arms of the tetrahedral linkers are connected in a uniform manner. Consequently, the formation of PCN-521 is more kinetically favored than that of PCN-522, which allows us to obtain phase pure single crystal of PCN-521 that are suitable for gas adsorption study. (See Figure III-8)

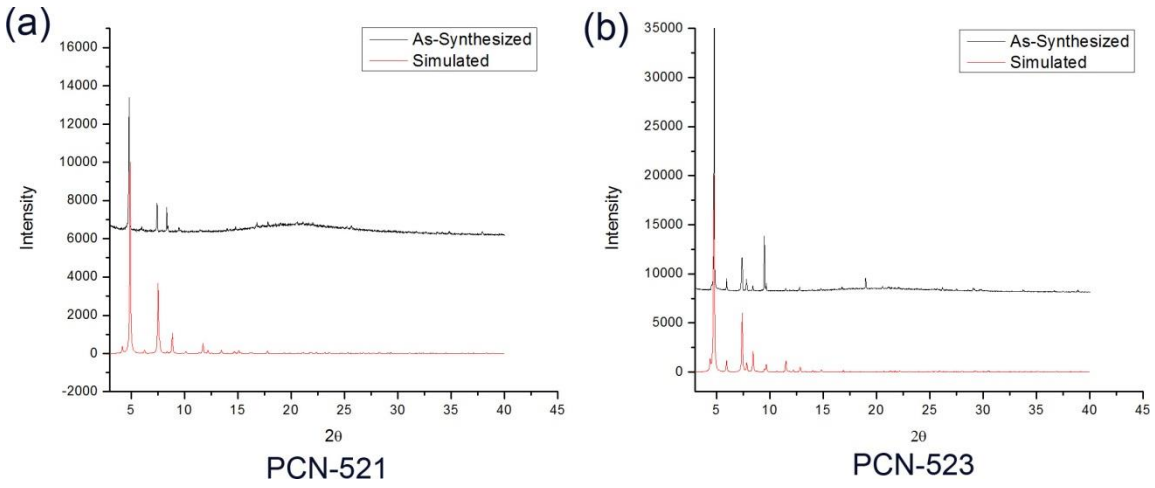

Figure III-8. The PXRD of (a) PCN-521, (b) PCN-523.

3.3.3 Non-Interpenetrated Nature of Fluorite Topology Nets

It should be noted that the **flu** net was identified as the only one in which tetrahedral (4-coordinated) and cubical (8-coordinated) vertices are joined by one kind of link, and is the default structure for that geometry. [83] Beside the existence of the large interstitial cavities, another reason that makes fluorite topology especially intriguing for MOF construction is that frameworks with this topology will not suffer from self-interpenetration. Interpenetration often occurs in topologies with lower connectivity, such as the topologies of **dia** (4,4-connected network), **pts** (4,4-connected network) and **pcu** (6,6-connected network). [59] As a 4,8-connected framework, fluorite-topology frameworks cannot be translated in any direction without overlapping with themselves. The net from the dual of the natural tiling of **flu** is **12-c fcu**, so there is no self-dual net. [84] However, this may not rule out the possibility that a highly distorted **flu** net may still suffer from self-interpenetration. [148]

The non-interpenetrated nature of fluorite topology can be further confirmed by checking the RCSR (Reticular Chemistry Structure Resource) Database, where no entry for "**flu-c**" topology was created ("**flu-c**" means a catenated fluorite framework). The RCSR Database enumerates all the possible nets from a mathematical point of view. The absence of the "**flu-c**" entry shows the interpenetrated fluorite topology does not exist. The RCSR Database is available at http://rcsr.anu.edu.au/. The explanation of usage of this database was described in the corresponding reviews. [88]

3.3.4 Porosity and Gas Sorption Study

To perform gas adsorption measurements, phase-pure single crystals of PCN-521 were obtained by a modulated synthesis strategy (see Figure III-6(a) and Figure III-8(a)). PCN-521 exhibits a type-I isotherm of N_2 sorption at 77 K and 1 bar (Figure III-9(a)), implying the existence of micropores in PCN-521. Its BET surface area is 3411 $m^2 \cdot g^{-1}$. In particular, this MOF has the largest surface area, pore size, and solvent-accessible volume among all MOFs constructed from tetrahedral ligands (See Table III-1). PCN-523 also exhibits permanent porosity and has a type-I isotherm of N_2 sorption at 77 K and 1 bar. Its BET surface area is 1224 $m^2 \cdot g^{-1}$. When O_2 was used, its BET surface area was measured as 1675 $m^2 \cdot g^{-1}$. (Figure III-9(b)) In consideration of a growing interest on surface area per unit volume, [130] the surface area per unit volume of these MOFs were also calculated. The volumetric surface area for PCN-521 is 1617 $m^2 \cdot cm^{-3}$, and for PCN-523 is 667 $m^2 \cdot cm^{-3}$.

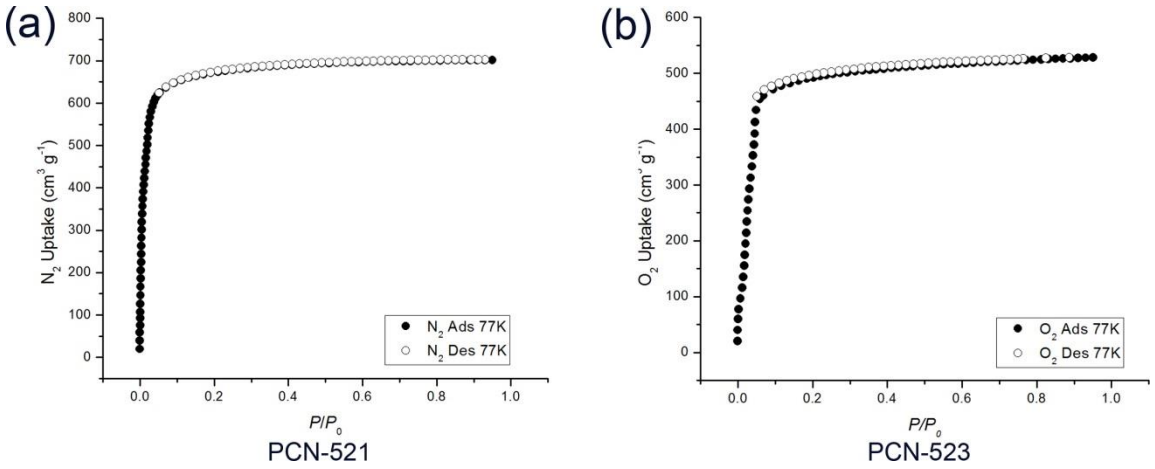

Figure III-9. (a) The N_2 sorption isotherms of PCN-521 at 77 K. (b) The O_2 sorption isotherms of PCN-523 at 77 K.

3.3.5 Thermogravimetric Analysis

The thermogravimetric analysis of PCN-521 and PCN-523 are illustrated in Figure III-10.

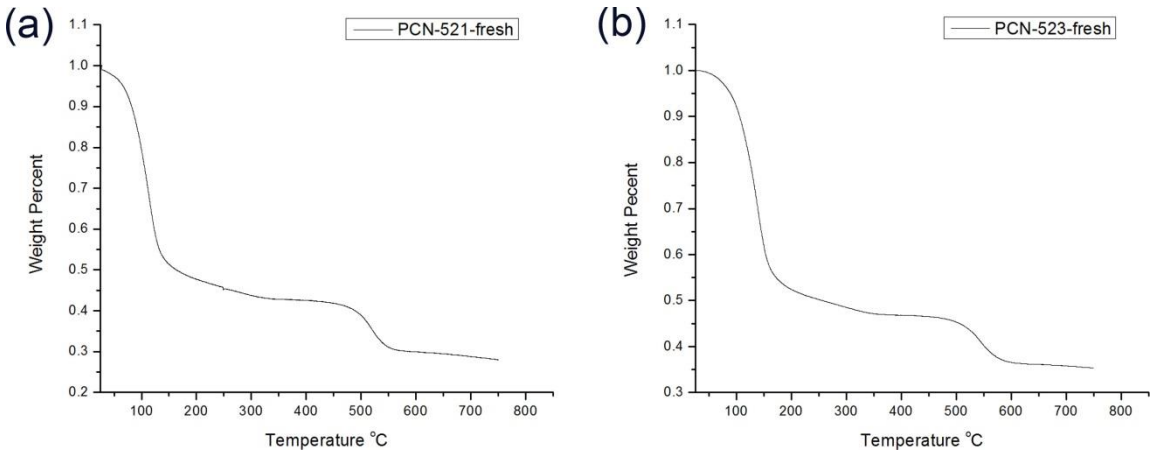

Figure III-10. Thermogravimetric analysis of (a) PCN-521, and (b) PCN-523.

For PCN-521, 50% weight loss is expected for DEF within the pores (25-130 ℃) for the fresh sample, and the next 10% weight loss is the trapped modulating reagent (such as benzoic acid) in the pores (130-500 ℃) for the fresh sample. The decomposition temperature is around 500 ℃ for fresh sample, which indicates the high thermal stability of this MOF. PCN-523 exhibits a very similar pattern in its thermogravimetric analysis plot.

3.4 Summary

In summary, by employing a symmetry-guided design strategy, two stable, non-interpenetrated MOFs, PCN-521 and PCN-523, were synthesized and characterized. PCN-521 has the largest cavity (20.5 × 20.5 × 37.4 Å), BET surface area (3411 $m^2 \cdot g^{-1}$) and solvent accessible volume (78.50%) of any MOF prepared from tetrahedral ligands. They are the first examples of non-interpenetrated MOFs synthesized from the **MTBC** ligand. This work not only illustrates a successful case of designing MOFs with a desired topology, but also provides a systematic way to construct stable, non-interpenetrated MOFs with high porosity.

Table III-1 contains a comprehensive list of MOFs constructed from all rigid ligands with inherent tetrahedral symmetry; and Scheme III-2 illustrates all of the ligand structures. Only MOFs with significant porosities were listed. Specifically, PCN-521 has the largest BET surface area, pore size and void volume among all the listed MOFs.

Table III-1: A comprehensive list of MOFs/coordination polymers with rigid tetrahedral ligands

MOFs	BET ($m^2 \cdot g^{-1}$)	Void volume [c]	Pore size diameter (Å) [a]	Topology	Inter-penetr-ated	Ligand type	Ref
PCN-521	3411	78.5%	21.0	**flu**	No	tetratopic	[48]
PCN-522	N/A [b]	72.8%	11.0	4,12,12[d]	No	tetratopic	‡
PCN-523	1224	77.9%	21.0	**flu**	No	tetratopic	[48]
PCN-501	3090	71.6%	13.0	4,6 [d]	No	mixed-ligand	‡
$Cu_2(ATC)(H_2O)_6$	560 [h]	38.5%	6.0	**pts**	No	tetratopic	[62]
$Zn_2(MTBA)(H_2O)_2$	N/A [b]	72.0%	8.9	**pts**	No	tetratopic	[63]
$Cu_2(MTBA)(H_2O)_2$	526	72.0%	8.4	**pts**	No	tetratopic	[64]
$Cu_2(MTBA)(H_2O)_2$ [e]	1560	N/A [e]	N/A [e]	N/A [e]	No	tetratopic	[64]
$Cd_4(MTBA)_2(DMF)_4$	N/A [b]	N/A	N/A	**flu**	No	tetratopic	[70]
$Cu_2(MTBC)(H_2O)_2$	791	73.0%	7.4	**pts**	Yes	tetratopic	[64]
$Cu_2(MTBC)(H_2O)_2$ [e]	1020	N/A [e]	N/A [e]	N/A [e]	Yes	tetratopic	[64]
$Zn_2(MTBC)(DMF)_4$	177	28.8%	6.2	2, 4 [d]	Yes	tetratopic	[65]
$Zn_2(MTBC)(DMF)_4$ [f]	1170	41.4%	6.2	N/A [f]	Yes	tetratopic	[65]
$Co_2(MTBC)(DMF)_4$	N/A	N/A	N/A	2, 4 [d]	Yes	tetratopic	[65]
$Zn_4(MTBC)(H_2MTBC)_2$	1284	62.4%	6.0	**alb/P** and **lon**	Yes	tetratopic	[66]
$Co_5(MTBC)(HMTBC)_2$	965	61.0%	6.0	**lon**	Yes	tetratopic	[66]
$Cu_2(MTTB)(H_2O)_2$	262 [i]	79.3% [i]	10.6	**pts**	Yes	tetratopic	[90]
$Zn_3(HTCPS)_2$	703	45.6%	6.0	**alb/P**	No	tetratopic	[52]
$Cu_2(TCPS)(H_2O)_2$	601	72.7%	8.6	**pts**	No	tetratopic	[52]
$Mn_6(TTPM)_3(DMF)_5$	N/A [b]	6.4%	6.0	**gar**	No	tetratopic	[68]
$Cu[(Cu_4Cl)(TTPM)_2]_2(CuCl_2)(DMF)_5$	N/A	19.7%	8.0	**flu**	No	tetratopic	[68]

Table III-1: Continued

MOFs	BET ($m^2 \cdot g^{-1}$)	Void volume [c]	Pore size diameter (Å) [a]	Topology	Inter-penetr-ated	Ligand type	Ref
$Cu_4(TTPM)_2(CuCl_2)_{0.7}$ [g]	2506	66.9%	14.1	N/A [g]	No	tetratopic	[68]
$H(Cu_4Cl)(TTPS)_2$	2665	74.3%	21.0	**flu**	No	tetratopic	[76]
$Mn_3(TTPS)_6$	N/A [i]	71.5%	17.0	**gar**	No	tetratopic	[149]
$Cu_4(STI)(H_2O)_4$	875	44.8%	7.2	**scu**	No	octatopic	[80]
$Cu_4(MTBD)(H_2O)_4$	2620	71.0%	8.9	**scu**	No	octatopic	[69]
$Cu_2(H_4TPPM)(H_2O)_2$	363	63.3%	14.3	**sql**	No	octatopic	[67]
$Zn_3(OH)(H_2O)]_4(TPPM)(H_2TPPM)_2$	2718	66.1%	6.8	**tph**	No	octatopic	[67]

‡ Unpublished work. PCN-522 is described in Chapter III; PCN-501 is described in Chapter V.

a Pore size indicates the largest sphere that can fit in its cavity.

b Framework is not stable upon activation.

c Calculated by *PLATON* routine.

d A name was not assigned to this topology yet. The numbers indicate their net connectivity.

e A structural change was observed when the samples were activated by freeze-thaw method

f This sample was obtained after the single crystal to single crystal transformation induced by CH_2Cl_2.

g This MOF is produced from the desolvation of Cu-$[(Cu_4Cl)(TTPM)_2]_2(CuCl_2)(DMF)_5$ where a structural change was observed.

h Langmuir surface area is provided.

i This framework is highly unstable and its activation has resulted in an almost complete collapse.

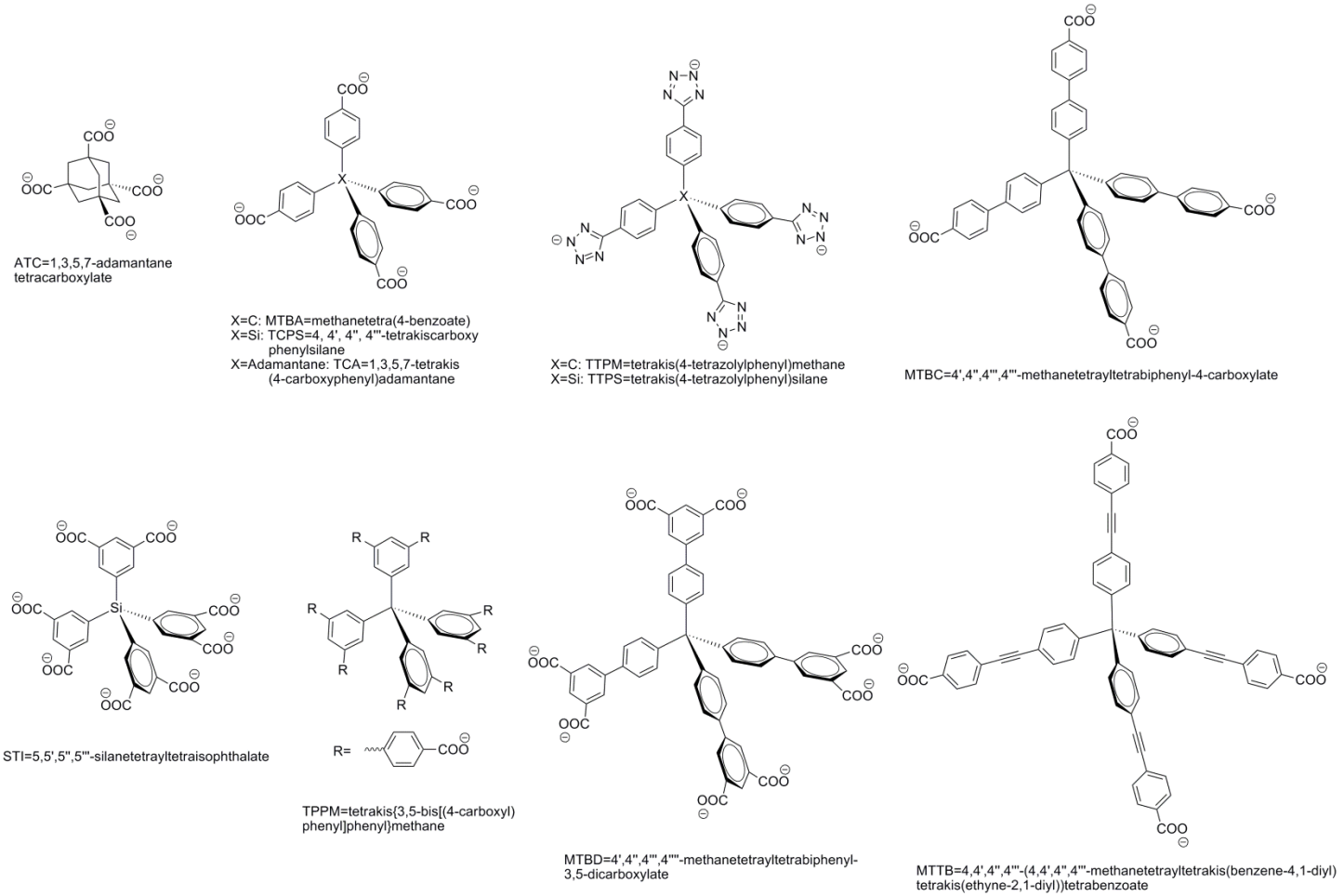

Scheme III-2. The full name and chemical structure of all the tetrahedral ligands.

CHAPTER IV

SYMMETRY-GUIDED DESIGN OF BENZIMIDAZOLE-INCORPORATED POROUS POLYMER NETWORK FOR CARBON CAPTURE WITH HIGH EFFICIENCY AND LOW COST [*]

4.1 Introduction

Elimination of CO_2 from mixed component gas streams has gained a tremendous amount of attention due to growing concern about the environmental and climatic impact of greenhouse gas emissions [150]. Many environmental problems, such as global warming and ocean acidification, have been primarily attributed to the escalating level of atmospheric CO_2. In order to reduce anthropogenic CO_2 emissions, various Carbon Capture and Sequestration (CCS) techniques have been investigated as means to selectively remove CO_2 from the flue gas of fossil-fuel-powered plants and then store it underground. [133] Aqueous alkanolamines, such as monoethanolamine (MEA) solutions, have been utilized due to their large CO_2 capacity and selectivity. [23] Nevertheless, this process suffers from a series of complications that have substantially limited their industrial applications, such as the high regeneration cost arising from the large heat capacity of aqueous MEA solutions, the toxicity, the unpleasant smell and the corrosive nature of amine compounds. [115]

[*] Reproduced with permission from "Stable Benzimidazole-Incorporated Porous Polymer Network for Carbon Capture with High Efficiency and Low Cost", by Zhang, M.; Perry, Z.; Park, J.; Zhou, H.-C., *Polymer* **2014,** *55*, 335-339, copyright 2014 by Elsevier B.V.

As an alternative solution, many solid adsorbents have been shown to be promising candidates to overcome the downsides of aqueous alkanolamine solutions. For the past few decades, advanced porous materials have been extensively investigated in scientific and technological research due to their capability to adsorb and interact with atoms, ions and molecules. PPNs are an emerging category of advanced porous materials that are of interest for carbon dioxide capture due to their great stabilities and convenient functionalization processes. Even though MOFs possesses many advantages such as enormous surface area, tunable structures and convenient post-synthetic modifications, most MOFs suffer from a limited stability, which restrained their practical applications. [111] PPNs, appearing as hyper-crosslinked organic polymers, have provided an alternative solution to the construction of ultra-porous materials with high thermal and chemical stability. [112] Unlike crystalline COFs [121], PPNs are amorphous materials with Brunauer–Emmett–Teller (BET) surface areas as large as 6461 $m^2 \cdot g^{-1}$ (in PPN-4), which is the largest PPN BET surface area to date [113]. Regardless of the enormous surface area and improved stability, those PPNs suffer from several shortcomings that generally hamper them from being practically implemented. First, their synthesis involves the coupling of tetrahedral monomers via the Yamamoto homo-coupling reaction, [112] which requires an extremely expensive and air-sensitive reagent, Bis(cyclooctadiene)nickel ($Ni(cod)_2$). This has significantly increased the production cost of PPNs and prevented their large-scale synthesis for industrial use. Second, many applications of porous materials require the functionalization of the inner pore surfaces. Being constructed primarily from phenyl rings or alkyne bridges, the lack of internal functionalization of those PPNs has

significantly limited their applications, especially for the purposes of carbon dioxide sequestration. Post-synthetic modifications (PSM) of those PPNs appear to be an efficient way to improve their functionality [115, 151]; however, the PSM process has not only drastically impaired their porosity but also further increased their production cost. It is highly desirable to synthesize functionalized PPNs with considerably large porosities and reasonable production costs for industrial CCS processes.

4.2 Experimental Section

4.2.1 Materials and Instrumentation

The tetrakis(4-formylphenyl)silane was synthesized by a previously reported procedure with slight modification. [152] Silicon tetrachloride ($SiCl_4$) and *n*-butyl lithium (*n*-BuLi) were purchased from Sigma Aldrich. The 4-bromobenzaldehyde diethyl acetal, benzene-1,2,4,5-tetraamine tetrahydrochloride, sodium bicarbonate ($NaHCO_3$), *N*,*N'*-dimethylformamide (DMF), tetrahydrofuran (THF), acetone, ethyl acetate, hexane and methanol were purchased from VWR. All commercial chemicals were used without further purification unless otherwise mentioned. ^{1}H nuclear magnetic resonance (NMR) data were recorded on a Mercury 300 MHz NMR spectrometer at the Center for Chemical Characterization and Analysis (CCCA), Department of Chemistry, Texas A&M University. Fourier transform infrared spectroscopy (FTIR) data were collected using a SHIMADZU IRAffinity-1 FTIR Spectrophotometer.

Powder X-ray diffraction (PXRD) was carried out with a BRUKER D8-Focus Bragg-Brentano X-ray Powder Diffractometer equipped with a Cu sealed tube (λ =

1.54178) at 40 kV and 40 mA. Thermogravimetric analyses (TGA) were performed on a SHIMADZU TGA-50 Thermogravimetric Analyzer with a heating rate of 5 ˚C·min^{-1} under N_2. Gas sorption measurements were conducted using a Micrometritics ASAP 2020 system at different temperatures.

4.2.2 Synthesis of PPN

The synthesis of PPN-101 was illustrated in Scheme IV-1.

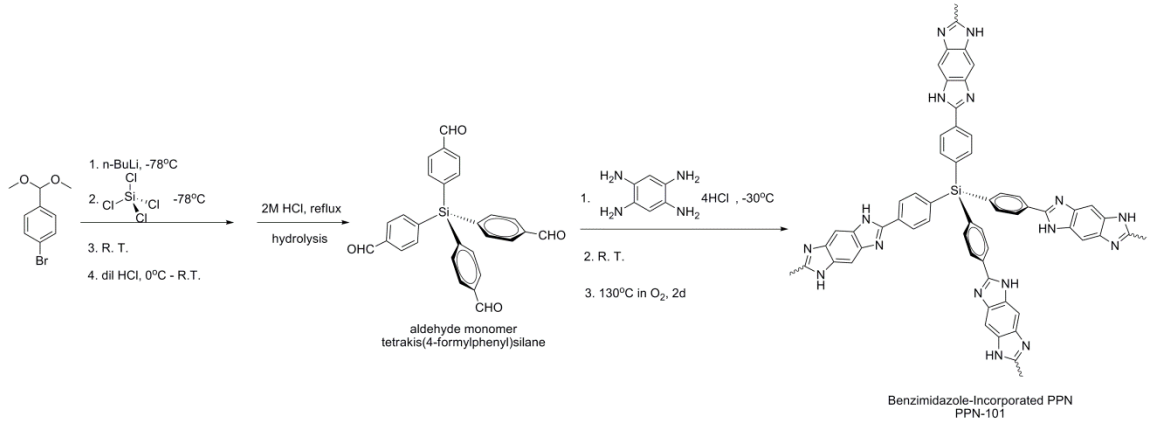

Scheme IV-1. The syntheses of the aldehyde monomer tetrakis(4-formylphenyl)silane and PPN-101. This PPN can be synthesized within two steps from commercially available compounds, and no extremely expensive reagent is involved.

Synthesis of tetrakis(4-formylphenyl)silane. A 500 mL round bottom flask equipped with a condenser was pumped under vacuum and refilled with N_2 three times before the dry 4-bromobenzaldehyde dimethyl acetal (pre-dried by molecular sieves, 10.90 mL, 52.5 mmol) was added. Freshly distilled THF from a solvent still (300 mL) was carefully added to the flask through a cannula. The solution was cooled to -78˚C by

a dry ice/acetone bath. At this temperature, n-butyl lithium (20 mL, 2.5 M in hexane) was added dropwise slowly over a period of 1 hour. The reaction mixture was kept at dry ice/acetone bath temperature -78˚C for an additional 2 hours before $SiCl_4$ (1.14 mL, 10 mmol) was added dropwise. The mixture was stirred at this temperature for an additional 2 hours before it was warmed up to room temperature and kept overnight. The reaction mixture was quenched with 2 M HCl (60 mL) and extracted with ethyl acetate (100 mL × 3). The combined organic phase was washed with brine, dried over $MgSO_4$ and evaporated to give the oily intermediate acetal product $Si(4\text{-}C_6H_4CH(OEt)_2)$, which was hydrolyzed without purification. The oil was dissolved in 100 mL THF/HCl (*aq*) and the mixture was refluxed for 2 hours. The reaction mixture was quenched with enough $NaHCO_3$ until no more formation of CO_2 was observed and extracted with ethyl acetate (100 mL×3). The combined organic phase was washed with brine, dried over $MgSO_4$ and evaporated to give an off-white solid as the crude product. A recrystallization in EtOAc/Hexane afforded 3.24 g white crystalline powder as the final product (72.32%). ^{1}H NMR (300 MHz, DMSO-d_6): δ = 10.08 (s, 4H, CHO), 8.01 (d, 8H, Ph), 7.75 (d, 8H, Ph).

Synthesis of PPN-101. PPN-101 was synthesized by a similar synthetic route as BILP-1. [153] The aldehyde monomer tetrakis(4-formylphenyl)silane (134 mg, 0.3 mmol) was dissolved in anhydrous DMF, and under N_2 atmosphere, the other monomer 1,2,4,5-tetrabenzeneamine tetrahydrochloride (176 mg, 0.6 mmol) dissolved in anhydrous DMF were added dropwise at cryogenic temperature. Orange precipitate was formed very slowly in the solution. The reaction was kept under cryogenic conditions until no more

precipitate was formed and then allowed to warm to r. t. overnight. Then the reaction mixture was placed under an O_2 atmosphere and heated at 130 ˚C for 2 days. (***Caution***: This step should be handled in an extremely cautious way to prevent any possible combustions or explosions. Protective shields should be used during the process of reaction). Fluffy yellowish polymer (119 mg) was produced in 59.2% yield. IR: 725 (s), 829 (s), 1018 (m), 1085 (m), 1294 (m), 1249 (m), 1610 (s), 2312 (w, br), 3616 (w, br).

4.2.3 Activation Procedures and Gas Sorption Measurements

The fresh polymer sample was washed with DMF three times for 3 days, methanol twice for 2 days, and acetone twice for 2 days. After activation at 80 ℃ for 8 h, a feathery bright yellow polymer was produced with a BET surface area of 996 $m^2 \cdot g^{-1}$ and Langmuir surface area of 1613 $m^2 \cdot g^{-1}$. After activation at 120 ℃ for 12 h, the BET surface area was improved to 1096 $m^2 \cdot g^{-1}$ and Langmuir surface area 1799 $m^2 \cdot g^{-1}$. This is probably due to the incomplete removal of the H_2O molecules residing at the Lewis base sites at lower temperatures. [153] A significant increase of both the N_2 and Ar uptake was observed when the sample was activated at an elevated temperature. Further increase of activation temperature did not result in a significant improvement of the surface area or a significant decrease of the weight of the sample.

4.2.4 The Calculation of CO_2/N_2 Selectivity

The Single Isotherm Selectivity. [23] The selectivity of CO_2/N_2 of PPN-101 in flue gas conditions was evaluated from the composition of flue gas where the partial

pressure for CO_2 is 0.15 bar and N_2 is 0.85 bar. The uptake of CO_2 at 0.15 bar and N_2 at 0.85 bar were estimated by linear interpolation, and the selectivity is calculated by Eq. 1.

$$Selectivity = \frac{Q_{CO_2}/Q_{N_2}}{P_{CO_2}/P_{N_2}} \qquad \textbf{Eq. 1}$$

In Eq. 1, Q indicates the quantity of the absorbents, while P indicates the partial pressure.

The IAST Selectivity. The calculation of IAST selectivity of PPN-101 is based on a reported method in literature. [154, 155]

4.3 Results and Discussion

4.3.1 Rational Design of Benzimidazole-Incorporated PPN for CO_2 Capture

Incorporation of Lewis bases into MOFs [22] and PPNs [115] has been demonstrated as an effective way to improve CO_2 uptake and CO_2/N_2 selectivity. These moieties can be incorporated into the struts of the PPN framework, or can be introduced by post-synthetic modification. Pyrazine [156], triazine [157, 158] and polyamines [115] have been successfully incorporated into PPNs. However, none of these materials can remove CO_2 from flue gas with both high efficiency and low cost. Despite the interesting electronic properties resulting from the conjugate system; the CO_2/N_2 selectivity of the pyrazine-incorporated PPN, Aza-CMP, was not investigated, probably due to the low porosity (BET surface area of 24 $m^2 \cdot g^{-1}$ when activated at 300 ˚C) and complicated activation procedure of this material [156]. The incorporation of triazine into PPN frameworks, as shown in TFM-1 [157] and CTF-PX series [158], was demonstrated as a moderately efficient

way to improve the CO_2/N_2 selectivity; however, the selectivity was restrained by the limited basicity of the triazine units. It is conceivable that incorporation of a more basic unit could further improve the CO_2/N_2 selectivity and CO_2 adsorption enthalpy due to the acidic nature of CO_2. The incorporation of polyamines into PPNs [115] was demonstrated as an efficient way to improve the CO_2/N_2 selectivity; however, $Ni(cod)_2$ was required in the synthesis, and the PSM process further increased the cost of this PPN. In spite of the high efficiency of CO_2 removal in polyamine PPNs, the overall production cost remains largely problematic.

Scheme IV-2 illustrates several basic units that have been successfully incorporated into PPNs. Benzimidazole incorporation into the frameworks can be used to improve the CO_2/N_2 selectivity. Polybenzimidazoles (PBIs) have been widely used in other areas, such as in proton-exchange membranes in fuel cells. [159] However, few of the PBIs turn out to be suitable materials for industrial separation of CO_2/N_2 due to their very limited porosity. El-Kaderi and coworkers [153] published the first benzimidazole-incorporated PPN named as BILP-1 (Benzimidazole Linked Polymer) by condensation of tetrakis(4-formylphenyl)methane and 2,3,6,7,10,11-hexaaminotriphenylene, with the BET surface area of 1172 $m^2 \cdot g^{-1}$ and CO_2 uptake of around 180 $mg \cdot g^{-1}$ at 273K, which makes it the first benzimidazole-incorporated PPN with considerable porosity for selective CO_2 removal. However, the laborious syntheses of both the aldehyde [160] and amine [161] monomers significantly increased the production cost of BILP-1 and hindered its synthesis in large quantities. After the discovery of BILP-1, they have provided a series of benzimidazole-incorporated PPNs where expensive monomers were utilized.

[162-164] In this work, PPN-101 was prepared from a synthetically-accessible silicon-centered aldehyde monomer [152] and a commercially available amine monomer, which has significantly brought down the production cost of this PPN, while the presence of the benzimidazole units produces a high CO_2/N_2 selectivity.

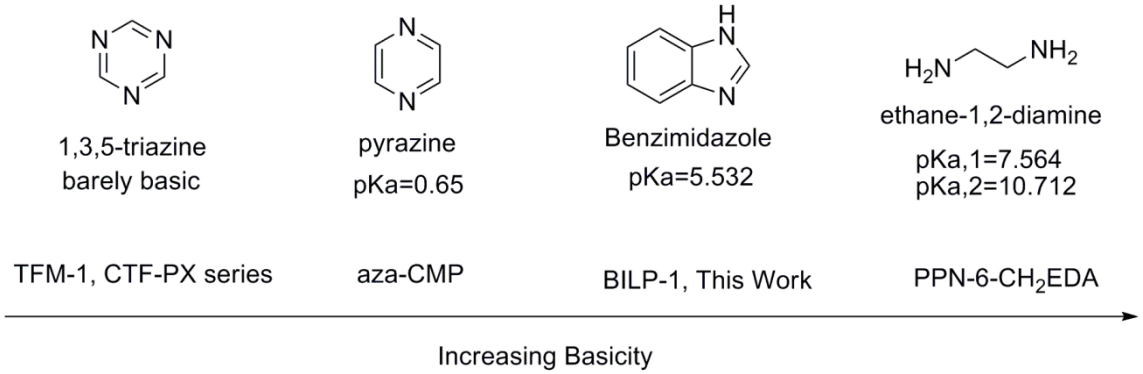

Scheme IV-2. The basicity of the basic units that have been incorporated into PPNs.

The symmetry-guided strategy can also be applied to the PPN synthesis. The fact that many PPNs built from tetrahedral monomers possess both good stability and large surface area has motivated us to keep exploring monomers with a tetrahedral geometry. [111-113] The combination of a tetrahedral unit and a linear unit will result in a framework with a diamondoid topology (**dia** topology). (Figure IV-1) Conceptually, this connectivity will not only retain the framework stability of the diamond-like structures, but also allow adequate exposure of the faces and edges of phenyl rings and benzimidazole rings to the adsorbents, which will increase the surface area and gas uptake capacities. [112] Additionally, the hypothetical diamondoid framework offers large cavities and interconnected pores to efficiently eliminate the "dead space" that has no

contribution to the framework porosity. [113] The introduction of silicon centered monomers, instead of working with the carbon-centered aldehyde monomer that suffers from a complicated synthesis as in BILP-1, has significantly simplified the preparation of the tetrahedral building unit.

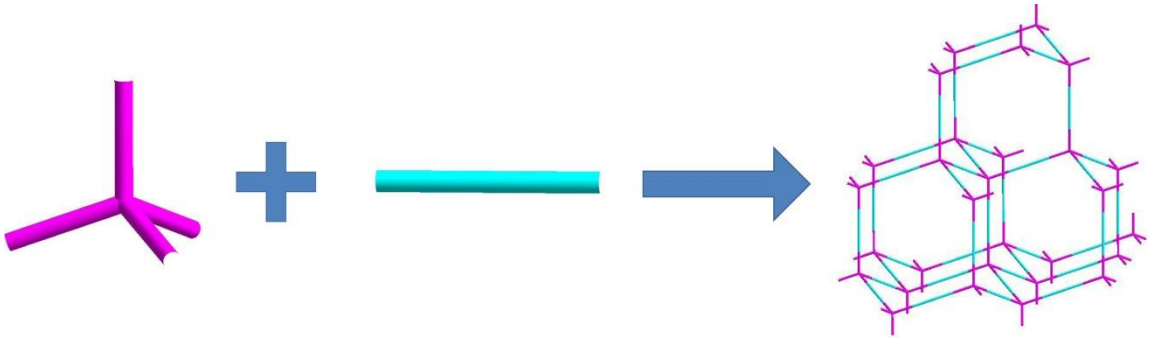

Figure IV-1. The conceptual illustration of an ideal network that incorporates tetrahedral nodes and linear nodes. Ideally, this will give rise to a network with diamondoid topology.

4.3.2 Porosity, Gas Sorption Study, and CO_2/N_2 Selectivity

Similar to other PPNs, PPN-101 is insoluble in commonly used solvents, which simplifies its purification and activation processes. Since the framework is constructed exclusively by robust covalent bonds, PPN-101 exhibits high chemical and thermal stability. The stability, porosity, and internal functionalization of PPN-101 have inspired us to study its gas uptake properties. PPN-101 is porous upon activation and exhibits a type-I isotherm of N_2 sorption at 77K and 1 bar (Figure IV-2(a)), implying the existence of micropores in PPN-101. Its Langmuir surface area, BET surface area and pore volume

are 1798 $m^2 \cdot g^{-1}$, 1095 $m^2 \cdot g^{-1}$, and 0.66 $cm^3 \cdot g^{-1}$, respectively. Its pore size distribution was calculated by the Density Functional Theory (DFT) method (Figure IV-2(b)). Its pore diameters are widely distributed from 10 Å to more than 50 Å and no pattern could be identified from the pore size distribution plot. This implies the amorphous nature of this PPN, which can further be confirmed by the Powder XRD. The most prominent pores have diameters of 11, 16 and 19 Å, respectively, which is consistent with the microporous nature of PPN-101, determined from the N_2 isotherms. Notably, it has a larger average pore size than that of BILP-1, in which the pore sizes were found to be centered at around 6.8 Å. [153] This is probably due to the diamondoid nature of PPN-101, which will inherently provide larger cavities. [113] Note that an isostructural PPN, BILP-4, [164] was published by El-Kaderi where the expensive tetrahedral monomer was used.

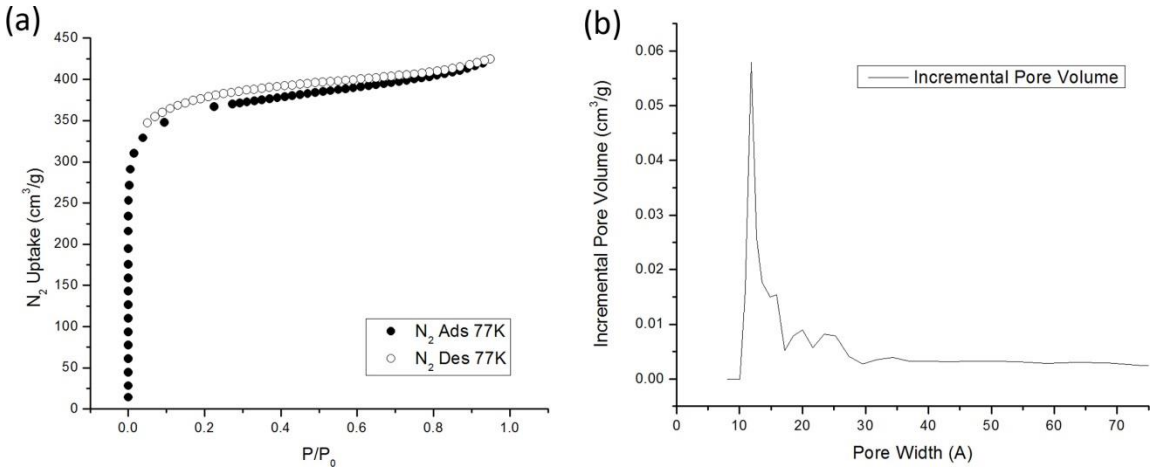

Figure IV-2. (a) The N_2 isotherm of PPN-101 at 77K, 1 bar (b) Its pore size distribution calculated by DFT method.

The benzimidazole-rich PPN-101 was designed to possess an excellent CO_2/N_2 selectivity. Figure IV-3(a) shows the gas uptake isotherms of CO_2 at 273 K and 298 K and the N_2 isotherm at 273 K. The isotherm for CO_2 uptake is fully reversible and the maximum uptake can reach 226.2 $mg \cdot g^{-1}$ at 273K, which is higher than the BILP-1 with 188 $mg \cdot g^{-1}$ at this temperature. [153] This probably resulted from the fact that PPN-101 has large pores and more Lewis base moieties than BILP-1. Additionally, its CO_2 uptake capacities at cryogenic conditions were also investigated. At 195 K and 0.95 bar, its CO_2 uptake is as high as 498 $cm^3 \cdot g^{-1}$. Notably, a deep rise of adsorption occurs between 0 and 0.1 bar, which indicates an excellent CO_2 affinity for the benzimidazole-incorporated PPN-101. A significant hysteresis was observed in cryogenic CO_2 isotherm, which probably resulted from the large heat of adsorption of CO_2 for PPN-101.

The selectivity of CO_2/N_2 of PPN-101 in flue gas conditions was evaluated by the ratio of the adsorbed gas quantity where the partial pressure for CO_2 is 0.15 bar and N_2 is 0.85 bar. Since minuscule N_2 adsorption occurs at 273 K, the calculated single-component CO_2/N_2 selectivity [23] of PPN-101 in flue gas at 273K is as large as 199 (See Electronic Supplementary Materials), which is significantly larger than other base-incorporated PPNs such as BILP-1 (Selectivity = 70) [153], TFM-1 (Selectivity = 48.2) [157] and CTF-PX (Selectivity = 16-24) [158] (See Table IV-1). The selectivity of PPN-101 is smaller than polyamine-tethered PPN-6 series (Selectivity of PPN-6-CH_2DETA is around 400, which is the best selectivity among PPN-6-series) [115], while the BET surface area of PPN-101 is considerably higher than that of PPN-6-CH_2DETA (555 $m^2 \cdot g^{-1}$), where the PSM process has significantly reduced the surface area of PPN-6 (4023 $m^2 \cdot g^{-1}$)

[151]. The calculated IAST selectivity [154, 155] of CO_2/N_2 at 273 K for PPN-101 is 45094. (See the Electronic Supplementary Materials of Ref. 117)

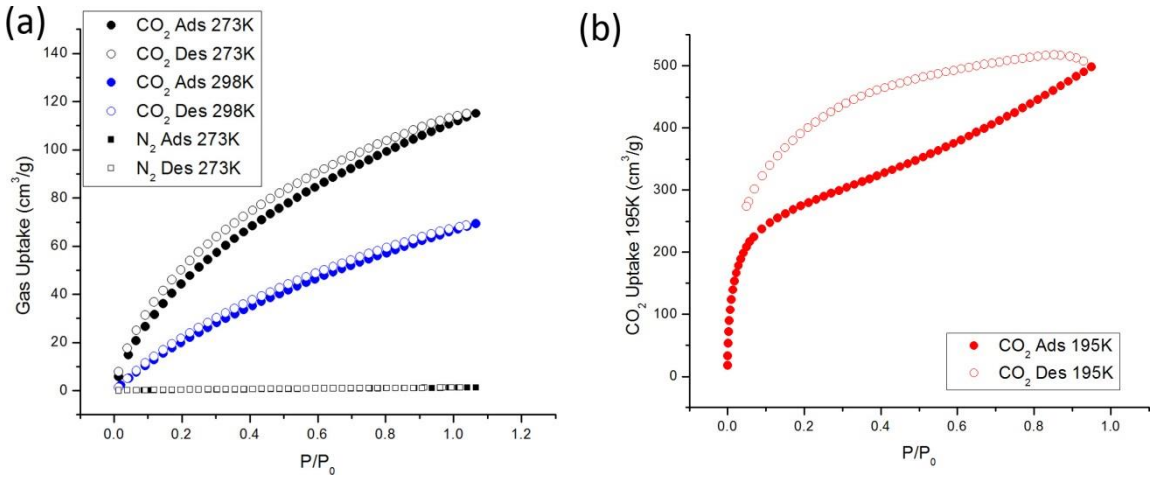

Figure IV-3. (a) CO_2 isotherms at 273K and 298K and the N_2 isotherm at 273K. (b) CO_2 isotherms at 195 K.

Along with its large CO_2 uptake, this PPN has a large H_2 and CH_4 uptake, which makes it very promising for gas storage applications due to its reduced cost. Its H_2 uptake at 77 K and 1.21 bar (906 mmHg) is 214.18 $cm^3 \cdot g^{-1}$ (1.91 wt %, Figure IV-4(a)), even without the presence of the unsaturated metal centers, which is similar to that of BILP-1 (19 mg/g, 1.86 wt %) [153] but larger than many other MOFs/PPNs that have similar BET surface areas. [17] Its CH_4 uptake at 273 K and 1.08 bar are 23.97 $cm^3 \cdot g^{-1}$ (Figure IV-4(b)). The introduction of benzimidazole units into PPN frameworks appears to be an efficient way to improve H_2 and CH_4 uptake as well.

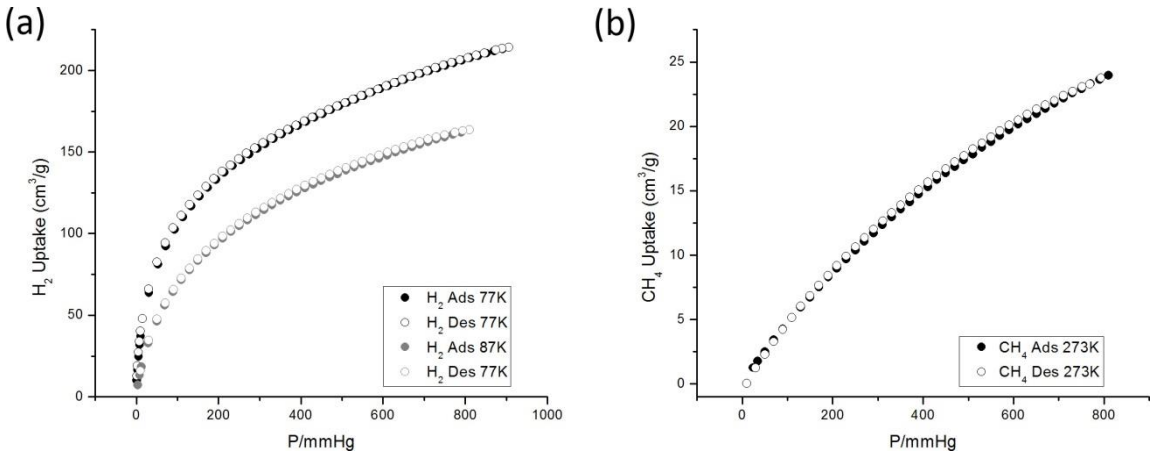

Figure IV-4. (a) The H_2 isotherm of PPN-101 at 77 K and 87 K, 1 bar. (b) The CH_4 isotherm of PPN-101 at 273 K, 1 bar

4.3.3 IR and TGA Characterization of PPN-101

The IR and TGA of PPN-101 sample of are illustrated in Figure IV-5.

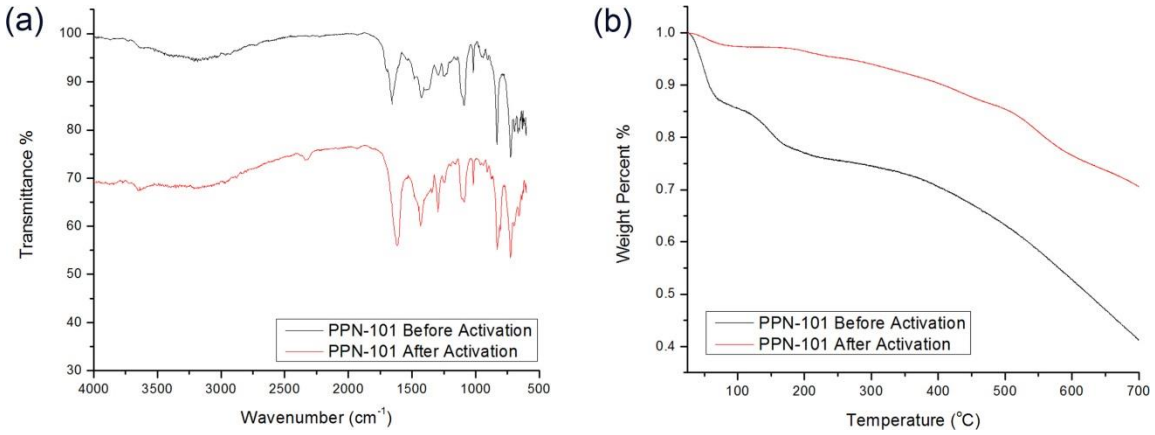

Figure IV-5. (a) The IR of the fresh sample (black) and activated sample (red) of PPN-101. (b) The TGA of the fresh sample (black) and activated sample (red) of PPN-101.

4.4 Summary

In conclusion, an intrinsically-functionalized porous network, PPN-101, was prepared from commercially accessible materials via an easy two-step synthesis. The combination of a tetrahedral monomer and a linear monomer has afforded a framework with a conceptual diamondoid topology. Due to the incorporation of the benzimidazole units, the CO_2 uptake of PPN-101 at 273 K reaches 115 $cm^3 \cdot g^{-1}$ and its calculated single-component CO_2/N_2 selectivity reaches 199. Its calculated IAST selectivity is 45094. Table IV-1 summarizes all the aforementioned base-incorporated PPNs. The low production expense, considerable surface area, and large CO_2/N_2 selectivity make PPN-101 a promising material for industrial CO_2 sequestration. Additionally, it also shows some promise for H_2 storage (1.91 wt % at 77 K, 1.21 bar) and methane storage (23.97 $cm^3 \cdot g^{-1}$ at 273 K, 1.08 bar).

Table IV-1. Summary of the BET surface area, CO_2/N_2 selectivity and production cost of all the aforementioned PPNs with basic units incorporated

	TFM-1	CTF-P6	Aza-CMP	BILP-1	PPN-101	PPN-6-CH_2DETA
Incorporated Units	Triazine	Triazine	Pyrazine	Benzimi-dazole	Benzimi-dazole	Polyamine
Basicity (pK_a)	barely basic	barely basic	0.65	5.532	5.532	$pK_{a,1}$>10
BET Surface Area ($m^2 \cdot g^{-1}$)	738	1152	24 [a] /1227 [b]	1172	1096	555
CO_2 Uptake (273K, $mg \cdot g^{-1}$)	76.1	148.1	N/A	188	226.2	189
Selectivity of CO_2/N_2	29±2	16.1	N/A	~70	199	~400
PSM required [c]	No	No	No	No	No	Yes
Ref	[157]	[158]	[156]	[153]	This Work	[115]

[a] Activated at 300 ˚C.

[b] Activated at 500 ˚C.

[c] PSM will reduce the porosity and increase the production cost.

CHAPTER V

SYMMETRY-GUIDED CONSTRUCTION OF HIGHLY POROUS MIXED-LIGAND METAL-ORGANIC FRAMEWORKS THROUGH HIGH-THROUGHPUT SYNTHESIS

5.1 Introduction

MOFs are an emerging category of porous materials that have gained a tremendous amount of attention in the past two decades. However, it is a challenging problem to rationally design a framework with anticipated properties by judicious selection of their fundamental building blocks from the vast database of available organic ligands and SBUs. Our group has recently reported a rational MOF design strategy, which implies the construction of highly porous MOFs with desired topology and porosity can be achieved by careful selection of two components that are symmetrically complementary with each other, based on a close examination of the topology of some simple mineral structures. [48] In addition to topology-guided MOF design, making mixed-ligand MOFs appears to be another significant strategy to create materials with ultrahigh porosity. [130, 131, 165-168] The traditional way of making highly porous MOFs typically involves the extension of the size of organic linkers based on an existing MOF structure. [41] However, the elongation of ligands usually accompanies complicated multi-step organic syntheses, where, in many cases, the usage of expensive reagents and catalysts is unavoidable. [110] Alternatively, mixed-ligand MOFs are coordination architectures that consist of SBUs connected by two or more organic

linkers, where each linker will otherwise generate a completely different MOF structure without the existence of the other ligand. Novel structures with high porosity and desired properties may be obtained by a combination of two existing ligands.

Nevertheless, the rational design of carboxylate-based mixed-ligand MOFs has been an exceedingly challenging problem for the past few decades, especially for the mixed-ligand MOFs made from two carboxylate linkers with different geometry. Even though more than 20,000 MOFs have been discovered and investigated in the past two decades [169], only an extremely limited amount of them are mixed-ligand MOFs with two carboxylate linkers, and their discoveries have been greatly dependent on serendipity. [165] This limitation may be attributed to several reasons. First, previous discovery of mixed-ligand MOFs largely depends on the trial-and-error method. Second, since the introduction of UMCM-1, [165] it appears that the majority of the subsequent work on carboxylate-based mixed-ligand MOFs are based on ligands with exactly the same geometry, that is, a tritopic ligand with trigonal planar geometry and a ditopic ligand with linear geometry. [140, 170-172] The lack of rational design has discouraged chemists to continue exploration of mixed-ligand MOFs made from ligands with other possible geometries. Third, it still remains largely problematic to predict the structure and properties of mixed-ligand MOFs. For MOFs made from one ligand, a reticular synthesis strategy appears to be an efficient way to envisage the structure, topology and porosity of a novel MOF based on an existing one. [41, 42] However, this rationale does not apply to mixed-ligand MOF systems, where the resulting MOF structures depend on the geometry, ratio and relative reactivity of two different ligands. Fourth, many mixed-

ligand MOFs suffer from complicated activation processes, [130, 167] presumably due to the existence of mesoporous cavities in their structures, which will inherently impair the framework stability and make them less favorable for gas storage applications. [173]

In this work, we demonstrated a successful implementation of rational design of mixed-ligand MOFs by close scrutiny of the correlation between the symmetries of their organic linkers, SBUs and the MOF Bravais lattices. Six microporous MOFs, PCN-501 – PCN-506, are constructed from a synthetically-accessible and commercially-affordable tetrahedral linker in combination with various linear linkers. [52] They are the first examples of mixed-ligand MOFs made from tetrahedral linkers. All of them possess significantly enlarged porosities compared to the MOFs made purely from the corresponding tetrahedral ligand. In particular, PCN-501 possesses a solvent accessible volume of 71.60% and volumetric surface area [130] of 2151 $m^2 \cdot cm^{-3}$, which is the largest value among all the MOFs made from tetrahedral ligands. More importantly, this work affords a general perspective for future design of mixed-ligand MOFs from various ligand geometries.

MOF formation is highly susceptible to many different reaction factors. Both compositional parameters (such as metal-to-ligand ratio, pH, solvents, *etc.*) and process parameters (such as reaction time, temperature, pressure, reaction container, *etc.*) may significantly affect the formation, structure, and other properties of a resulting framework. [174] The challenge of mixed-ligand MOFs primarily lies in the fact that the introduction of an additional ligand will further complicate the reaction parameters, and may possibly disrupt the chemical equilibrium that could have been favorable for MOF

formation. Selection of one oxygen-donor ligand (usually carboxylates) and one nitrogen-donor ligand (such as pyridines, [40] imidazolates, [175] adeninates, [98, 167, 176] *etc.*) may facilitate the formation of mixed-ligand MOFs. Due to their distinctive coordination abilities to a particular metal ion, the undesired competing reactions between the two ligands are significantly reduced, and thus each ligand may preferentially stay in a lattice position where its coordination chemistry is favored. Indeed, the majority of reported mixed-ligand MOFs fall into this category. Another category of mixed-ligand MOFs that consist of two carboxylate ligands still remains largely underdeveloped. Even though it is rare, a close examination of all the existing structures reveals that a judicious selection of two ligands with complementary symmetry may be favorable for the construction of carboxylate-based mixed-ligand MOFs.

Based on a careful examination of symmetry elements in Bravais lattices, we postulate that a carboxylate-based mixed-ligand MOF can be rationally designed by the combination of a non-centrosymmetric ligand (with reflectional or rotational symmetry) with a centrosymmetric ligand (with inversion center). (Figure V-1) For simplicity, hereinafter the non-centrosymmetric ligand with reflectional or rotational symmetry will be referred as "primary ligand" and the centrosymmetric one as "co-ligand" in this manuscript. For a given crystal lattice, the *point group symmetry* of each basic building block of its crystal structure has to be consistent with its *Bravais lattice symmetry*. It is further suggested that the primary ligand will always be incorporated into a lattice position where the rotational axis or mirror planes are located, whereas, the co-ligand should always occupy the positions of inversion centers in a MOF lattice. In other words,

ligands with different geometries will be selectively and discriminatively incorporated into a specific position where their molecular symmetry matches the Bravais lattice symmetry of a resulting MOF. It is this selective ligand incorporation process that circumvents the undesired competing reactions between the two ligands and facilitates the formation of materials with long-range regularity in the arrangement of ligands in its Bravais lattices. The space group of the final MOF structure is a result of a combination of all the symmetry elements from the primary ligand, the co-ligand, and the SBUs.

Ligands with tetrahedral geometry have attracted our attention due to their intrinsic three-dimensional nature and diversity of symmetry elements. [52] (See Figure I-2) Even though a tetrahedral ligand possesses a full T_d symmetry, it may adopt the symmetry of any T_d subgroups when it is incorporated into a MOF framework. The lack of inversion center and the richness in rotational/mirror symmetries make them very promising ligands for the construction of mixed-ligand MOFs, when viewed through the perspective of symmetry-guided design. The **TCPS** ligand (H_4**TCPS**=4,4',4",4"'-tetrakiscarboxyphenylsilane) was utilized as the primary ligand in this work because of its convenient synthesis from inexpensive starting materials. High-throughput synthesis was employed in this work for the purpose of searching for the optimized solvothermal condition for the preparation of each mixed-ligand MOF. [177-179]

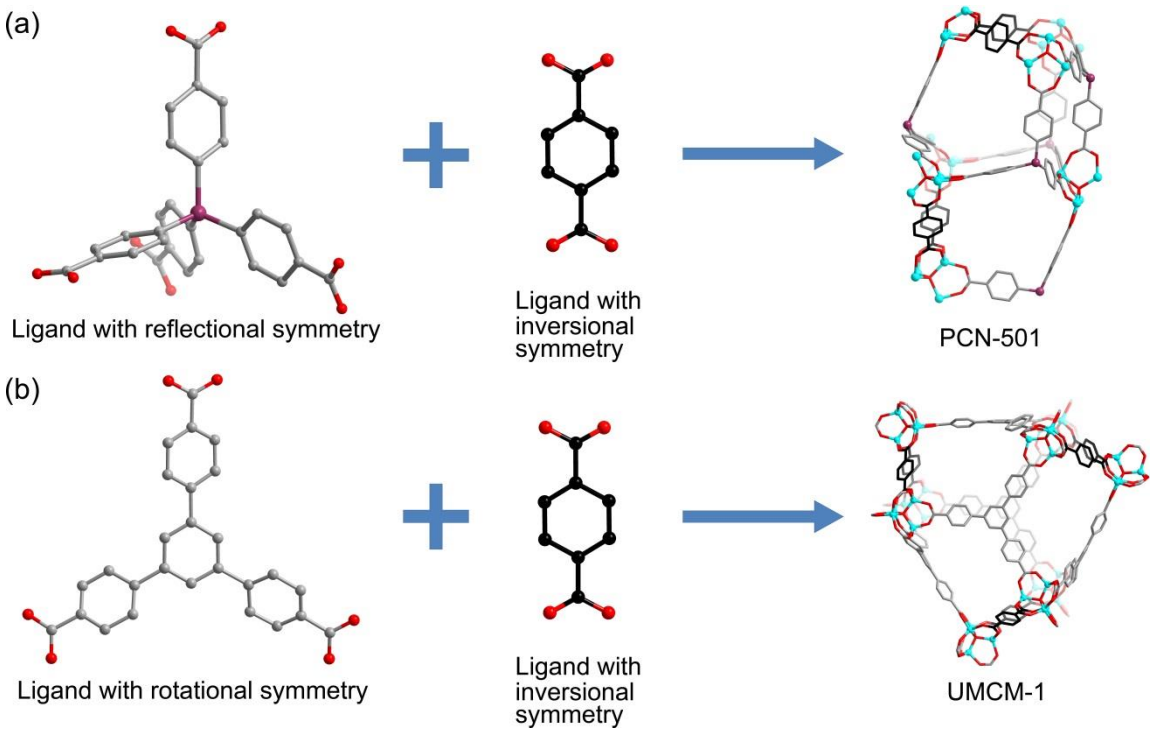

Figure V-1. Mixed-ligand MOFs can be rationally designed by the combination of a non-centrosymmetric ligand (with a reflectional or rotational symmetry) with a centrosymmetric ligand (with an inversional symmetry). (a) The synthesis of PCN-501, where the utilization of a tetrahedral ligand has generated a cage with a mirror plane. (b) The synthesis of UMCM-1, where the utilization of a trigonal planar ligand has generated a cage with a C_3 proper rotational axis. Color Scheme: C: gray; C (on linear ligands): black; O: red; Si: purple; Zn: cyan. H atoms are omitted for clarity.

5.2 Experimental Section

5.2.1 Materials and Instrumentation

The 4,4',4",4"'-tetrakiscarboxyphenylsilane (H_4**TCPS**) was prepared according to a reported procedure with some modifications. [52, 123] Silicon tetrachloride ($SiCl_4$) and *n*-

butyl lithium (*n*-BuLi) were purchased from Sigma Aldrich, and all other chemicals were purchased from VWR unless otherwise mentioned. All chemicals were used without further purification unless otherwise mentioned. ^{1}H nuclear magnetic resonance (NMR) data were recorded on a Mercury 300 MHz NMR spectrometer at the Center for Chemical Characterization and Analysis (CCCA), Department of Chemistry, Texas A&M University. Fourier transform infrared spectroscopy (FTIR) data were collected by a SHIMADZU IRAffinity-1 FTIR Spectrophotometer. Powder X-ray diffraction (PXRD) was carried out with a BRUKER D8-Focus Bragg-Brentano X-ray Powder Diffractometer equipped with a Cu sealed tube (λ = 1.54178) at 40 kV and 40 mA. Thermogravimetric analyses (TGA) were performed on a SHIMADZU TGA-50 Thermogravimetric Analyzer with a heating rate of 5 ℃·min^{-1} under N_2. Gas sorption measurements were conducted using a Micrometritics ASAP 2020 system at listed temperatures.

5.2.2 Ligand Synthesis

The synthesis of H_4**TCPS** ligand was illustrated in Scheme V-1. Its preparation involves a two-step reaction without using expensive reagents or catalysts. In order to accurately control the ratio between different ligands in the high-throughput synthesis on the robotic platform, compounds with high purity must be utilized. In this work, the H_4**TCPS** ligand was prepared through an oxidation reaction of 4,4',4",4"'-silanetetrayltetrabenzaldehyde [117, 152] for the purpose of obtaining a product with improved yield and purity.

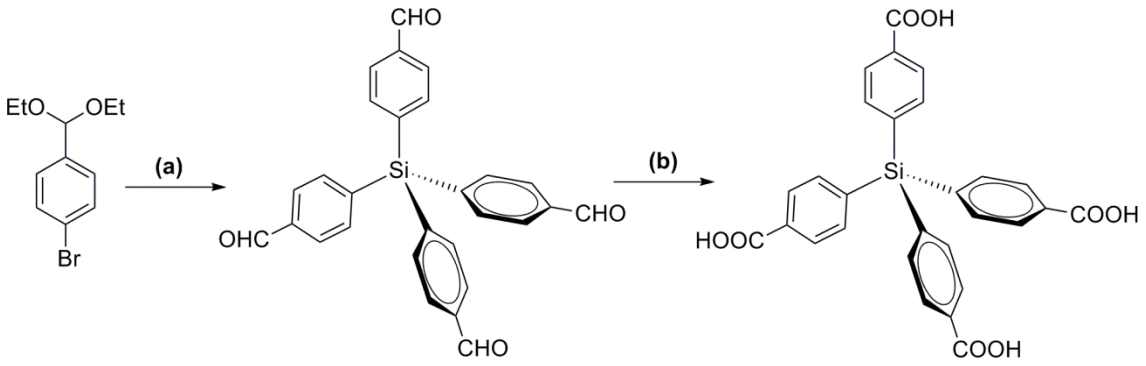

(a) 1. n-BuLi, -78°C; $SiCl_4$, -78°C; 2. dil HCl, 0°C - R.T.; 3. 2M HCl/THF, reflux
(b) 1. $KMnO_4$, Pyridine/H_2O, reflux; 2. HCl

Scheme V-1. Synthesis of the H_4**TCPS** ligand. Compared to the synthetic route described in Chapter II, this approach provides products with improved yield and purity, while it still does not involve any expensive catalysts or flash chromatography in its synthesis.

Synthesis of tetrakis(4-formylphenyl)silane. A detailed description of the synthesis of tetrakis(4-formylphenyl)silane can be found in Chapter V, Section 4.2.2. Final products were harvested as white crystalline powders. ^{1}H NMR (300 MHz, DMSO-d_6): δ = 10.08 (s, 4H, CHO), 8.01 (d, 8H, Ph), 7.75 (d, 8H, Ph).

Synthesis of 4,4′,4″,4‴-tetrakiscarboxyphenylsilane. A 250 mL round-bottomed flask was charged with 2.24 g (5 mmol) of tetrakis(4-formylphenyl)silane, 20 mL of water and 100 mL of pyridine. While the reaction was refluxing, 3 g $KMnO_4$ was added carefully in two portions and the reaction mixture was refluxed overnight. The flask was then cooled to room temperature and CH_3OH was added slowly to decompose unreacted potassium permanganate. Filtration provided a clear solution and the solid was washed with hot water. The filtrate was concentrated to dryness and 50 mL water was

added to dissolve the solid. Concentrated HCl was added cautiously until no more precipitate formed. Filtration yielded the final product as a white solid (2.5 g, 98%). It is suggested that the H_4**TCPS** ligand synthesized in this method possesses a significantly improved quality. The final product was directly used in the subsequent high-throughput synthesis without further purification. ^{1}H NMR (300 MHz, DMSO-d_6): δ = 8.02 (d, 8H, Ph) and 7.62 (d, 8H, Ph).

5.2.3 High-Throughput Synthesis of Mixed-Ligand MOFs

High-Throughput Synthesis. Due to the potential complexity of mixed-ligand MOF systems, high-throughput screening was employed to identify the optimized reaction condition for each individual MOF. The high-throughput experiments were performed on a robotic system equipped with solid- and liquid-dispensing functionality. The model of this robotic system is a Swing/Swave/Sweigher Synthesizer, assembled by Chemspeed Technologies. The recipes for each screening reaction were programmed through a client computer terminal using the "Application Editor" module, and then executed through the "Application Executor" module. A simulation run should be performed through the "Application Executor" module for each experiment before the program was actually executed.

All the MOFs were synthesized by solvothermal reactions in a 2 mL Pyrex vial unless otherwise mentioned. By varying the ratio of two ligands, the metal-to-ligand ratio, the pH and solvents, the optimized synthetic condition for each mixed-ligand MOF could be identified. The robotic platform was programmed to distribute the desired

amount of each compound into a collection of vials. The recipe for each individual vial can be specified by using the "Application Editor" module installed on the client computer terminal.

Even though powder dispensing is allowed in this robotic platform, liquid dispensing was utilized throughout the entire experiment for the following reasons. First, most of the solids involved in this experiment, particularly the metal salts, are sticky and hygroscopic. This makes it almost impossible for these solids to be transferred through a solid dispensing method. Second, the hygroscopicity of these solids will significantly affect the dispensing accuracy as well, where gravimetric measurement was utilized to determine the appropriate quantity of solid to be transferred. On the other hand, utilization of liquid dispensing will considerably simplify the distribution of various compounds by aspirating their stock solutions into a particular vial, and it will significantly enhance the dispensing accuracy as well.

The stock solutions of all the reactants were aspirated through needles on the robot arm, where the needles are connected to the syringes that are located in the cabinet of the robotic system. Four syringes, with volumes of 20 mL, 1 mL, 1 mL, and 1 mL, were utilized for liquid dispensing. The volume of liquid to be dispensed determines which syringe to use. Once the liquid is aspirated, the needle moves to the appropriate vial through movements of the robotic arm and transfers the desired amount of liquid into that particular vial. The needle was thoroughly washed by the particular solvent for each experiment to avoid cross-contamination.

Preparation of Stock Solutions. All the solids, including various ligands and metal salts, were dissolved in stock solutions prior to their dispensing. After a variety of different solvents were tried, DMA is identified as the best solvent for the growth of these mixed-ligand MOFs. NMP may be needed as an additional solvent to improve the quality of mixed-ligand MOF products. The majority of the mixed-ligand MOFs reported in this manuscript was prepared from the following stock solutions: 0.025 $mol \cdot L^{-1}$ of tetrahedral ligand (H_4**TCPS**), 0.05 $mol \cdot L^{-1}$ of linear ligands, and 0.083 $mol \cdot L^{-1}$ of metal salts.

Preparation of Mixed-Ligand MOFs. The vials containing these stock solutions, along with two vials of pure solvents (also known as "stock solvents") and two vials of rinsing solvents (also known as "washing solvents"), were placed in the robotic platform at the desirable positions. Transferring stock solvents into a particular vial will tune the overall concentration of all the solutes. The washing solvents were used to rinse the needles prior to distributing any particular solution with the same solvent. A program was written to distribute a specific amount of each stock solution into a large number of sample vials, from which the best condition for making mixed-ligand MOFs can be identified. A good program for high-throughput synthesis should possess some important attributes such as being time-saving, adaptable, easily understandable and reusable. In other words, a good program will allow us to try a maximum amount of different possible combinations of all reaction variables within a limited amount of vials; at the same time, this program should be easy to understand and easy to be adapted to other similar situations where high-throughput synthesis should be utilized.

Figure V-2 illustrates one of the programs that were used in this experiment. In this program, the stock solutions were transferred to 36 sample vials, which are oriented in the arrangement depicted in Figure V-2. For the purpose of finding the optimized condition for the formation of mixed-ligand MOFs with the maximum efficiency, this program allows to perform the MOF-screening experiment with two distinctive solvents and two different metal salts simultaneously. For a given combination of a metal salt (for example, $Zn(NO_3)_2 \cdot 6H_2O$) and a solvent (for example, DMA), 9 different vials with a varying ratio between two ligands (the tetrahedral ligand and one linear ligand) were distributed by the program. Once a mixed-ligand MOF was identified, similar programs can be written to further explore its optimized condition by changing the ratio of the two ligands with greater accuracy.

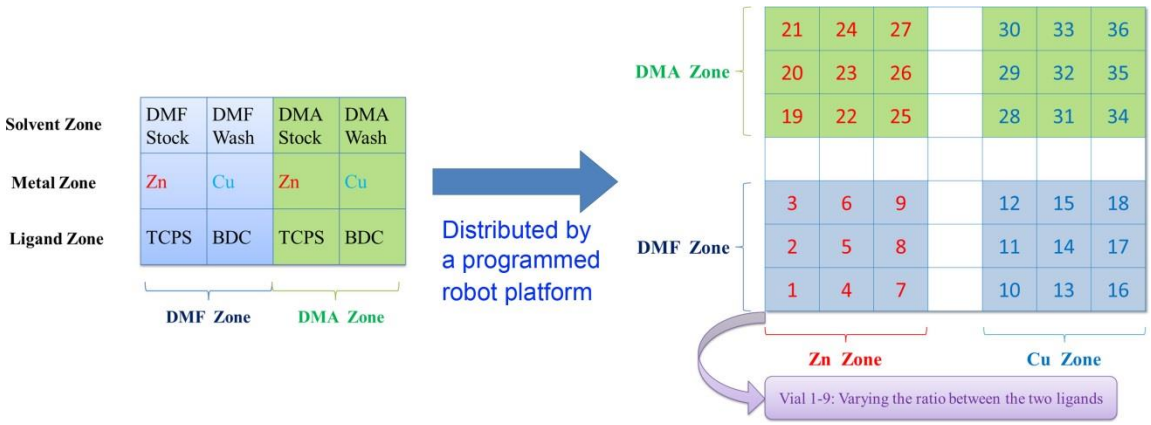

Figure V-2. A graphic illustration of the distribution of stock solutions into desirable vials through a programmed robotic platform.

Another important variable for this experiment is the chemical structure of the co-ligand itself. Different co-ligands with varying size and geometry will generate distinct MOF structures. Based on the hypothesis proposed in the introduction (see Figure V-1), the combination of a tetrahedral ligand with linear ligands (with inversion centers) are likely to produce mixed-ligand MOF structures. This hypothesis is confirmed by the successful construction of six novel mixed-ligand MOFs, named as PCN-501 – 506, by using six distinct linear ligands. The chemical structures of each linear ligand are illustrated in Scheme V-II. The optimized conditions for synthesizing each MOF were summarized in Table V-1.

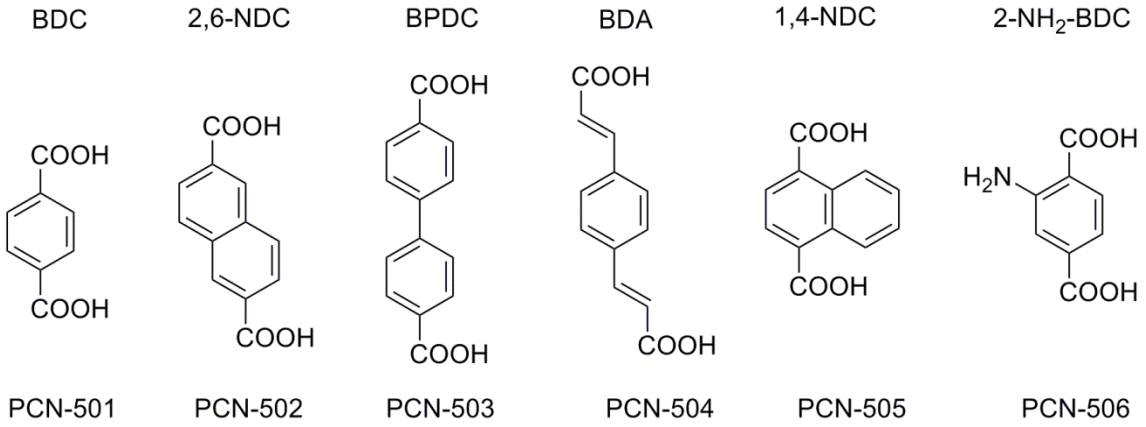

Scheme V-2. The chemical structures of the linear ligands used in mixed-ligand MOFs.

Interestingly, even though a great variety of different metal salts were tried, zinc appeared to be the only metal that yields mixed-ligand MOFs in this tetrahedral-linear mixed-ligand MOF system. All the reported mixed-ligand MOFs were synthesized in

DMA, where the presence of NMP may be necessary for the formation of crystals with better quality in occasional cases.

Table V-1. The optimized synthetic conditions for the mixed-ligand MOFs

MOF	Co-ligand	Ligand I [a] (mL)	Ligand II [a] (mL)	Feed Ratio	Metal [b] (mL)	Primary Solvent [c]	Additional Solvent [d] (mL)	Temp (°C)	Time (h)
PCN-501	BDC	0.29	0.21	1 : 1.45	0.9	DMA	DMA 0.3	100	24
PCN-502	2,6-NDC	0.26	0.24	1 : 1.85	0.9	DMA	NMP 0.3	75	72
PCN-503	BPDC	0.22	0.28	1 : 2.55	0.9	DMA	DMA 0.3	85	48
PCN-504	BDA	0.19	0.31	1 : 3.26	0.9	DMA	DMA 0.3	85	48
PCN-505	1,4-NDC	0.23	0.27	1 : 2.35	0.9	DMA	DMA 0.3	100	24
PCN-506	2-NH_2-BDC	0.25	0.25	1 : 2	0.9	DMA	DMA 0.3	100	24
PCN-511 [e]	N/A	0.5	N/A	N/A	0.9	DEF	DEF 0.3	85	48
PCN-515 [e]	N/A	0.5	N/A	N/A	0.9	DMA	NMP 0.3	85	96

[a] Ligand I and II are 0.025 M tetrahedral ligand and 0.05 M linear ligand dissolved in the primary solvent, respectively.

[b] The metal salt is 0.083 M $Zn(NO_3)_2 \cdot 6H_2O$ dissolved in the primary solvent.

[c] Primary solvent is the solvent used for preparing the stock solutions.

[d] Additional solvent of listed amount was added to the reaction after distributing all the stock solutions into a particular vial.

[e] PCN-511 and PCN-515, two MOFs made only by the TCPS ligand, are listed for comparison. [52]

5.2.4 Structure Determination of Single Crystals of PCN-501 – PCN-506

All compounds, PCN-501 – PCN-506 were taken from the solution directly, transferred into oil and mounted onto a loop for single crystal X-ray data collection. Diffraction patterns were measured on a Bruker Smart Apex diffractometer equipped with a Mo-Kα sealed-tube X-ray source (λ = 0.71073 Å) under protection of N_2 stream at 110 K. The data frames were recorded using the program APEX2 and processed using SAINT routine within APEX2. The data were corrected for absorption and beam corrections based on the semi-empirical technique as implemented in *SADABS*. All

structures were solved by direct methods using *SHELXS* and refined by full-matrix least-squares on F^2 using *SHELXL* software.

Refinement Details of PCN-501. Diffraction frames were integrated in Orthorhombic P by APEX2. *XPREP* agreed that the R(sym) is 0.063 for this Bravais lattice and *n*-glide plane exists based on statistics of systematic absence. A centrosymmetric space group, *Pnma*, was the best candidate with mean |E*E-1|= 0.921 and lowest CFOM factor (2.86). It transforms the diffraction patterns to generate Fourier peaks by direct method. The atom (O1S) is part of DMA solvents, which was neglected due to an enormous thermal ellipsoid. Without any geometry restraints for the structure, we obtained an R value of 0.1161 before the *SQUEEZE* routine of *PLATON* and 0.0683 after that. The squeezed void volume was 6694 $Å^3$, equivalent to 70.3% of the unit cell.

Refinement Details of PCN-502. Diffraction frames were integrated in Monoclinic P by APEX2, and *XPREP* also agreed this Bravais lattice with a low R(sym) of 0.035. Centrosymmetric space group, $P2_1/m$, was the best candidate with mean |E*E-1|= 0.955 and lowest CFOM factor (1.67). It transforms the diffraction patterns to generate Fourier peaks by direct method. The Fourier peaks for the main frameworks were clear and sharp; but those for solvent molecules were confusing due to disordered orientations. After using geometry restraints for those DMA molecules, the isotropic atomic displacement parameters (ADPs) of these atoms were larger than 0.2, which indicates too many electrons were assigned on the positions, inferring the occupancy of these atoms should be lower. Consequently, occupancy refinement was done: 40% for the one containing O3S and 60% for the other free one containing O4S. The isotropic

ADPs of the DMA molecule close to the Zn cluster were reduced to 0.06 while those of the free one were 0.11. It is reasonable to obtain lower ADPs for the solvent near the Zn cluster on account of H-bonds formed by H101, H103 and O3S. The R value is 0.999 before *SQUEEZE* treatment and 0.0634 after *SQUEEZE* treatment. The squeezed void volume was 3708 $Å^3$, equivalent to 54.1% of the unit cell.

Refinement Details of PCN-503. Diffraction frames were integrated in Monoclinic C by APEX2, and *XPREP* also agreed this Bravais lattice with a low R(sym) of 0.057. Centrosymmetric space group, *C2/c,* was the possible candidate with lowest CFOM factor (2.48), whereas the other non-centrosymmetric choice, *Cc*, could promote its symmetry to *C2/c* as well. It transforms the diffraction patterns to generate Fourier peaks by a direct method. All non-hydrogen atoms were easily found after using *SHELXS.* R value is 0.796 before *SQUEEZE* treatment and 0.0391 after that. The squeezed void volume was 16196 $Å^3$, equivalent to 70.0% of the unit cell.

Refinement Details of PCN-504. It should be noted that the unit cell parameters are very similar to those of PCN-503. As expected, diffraction frames were integrated in Monoclinic C and solved in *C2/c* as well. With the help of geometry and ADP restraints, we obtained R value is 0.1384 before *SQUEEZE* routine and 0.0622 after *SQUEEZE*. The squeezed void volume was 16271 $Å^3$, equivalent to 71.3% of the unit cell.

Refinement Details of PCN-505. It should be noted that the unit cell parameters are very similar to those of PCN-501. As expected, diffraction frames were integrated in Orthorhombic P and solved in *Pnma.* Non-hydrogen atoms of the tetrahedral ligand were easily found after running *SHELXS.* However, those of the linear ligand were confusing

and not able to connect to each other smoothly. Since the linear ligand was located at a special position, we constructed a symmetric-disordered model. The site occupancy factor instructions for the linear ligand must be changed to 10.5000 and all disordered atoms must be flanked with PART -1 and PART 0. (PART -1 command suppresses the automatic generation of special position constraints, and cancels the bond connectivity formed by symmetry-related atoms) With restraints of geometry and ADPs, we obtained an R value of 0.1522 before *SQUEEZE* routine of *PLATON* and 0.0633 after that. The squeezed void volume was 6254 $Å^3$, equivalent to 65.4% of the unit cell.

Refinement Details of PCN-506. It should be noted that the unit cell parameters are also very similar to those of PCN-501 and PCN-505. As expected, diffraction frames were integrated in Orthorhombic P and solved in *Pnma.* All non-hydrogen atoms of the tetrahedral ligand and linear ligand were easily found. The occupancy for the linear ligand must be changed to 10.25000 because there is only one $–NH_2$ group attaching on the molecule but showing up at 4 sites. With restraints of geometry and ADPs, we obtained an R value of 0.1379 before *SQUEEZE* routine of *PLATON* and 0.0552 after that. The squeezed void volume was 6421 $Å^3$, equivalent to 67.4% of the unit cell.

PLATON addsym unit were performed twice for every compound: one is checking the heavy atom moiety, the other is checking the final structure. After reasonable geometry of all ligands and solvents were done, eccentric atoms were refined with the help of EADP restrains on each ligand as well as solvent molecules to clear the warnings about non-positive definite matrices and unreasonable thermal ellipsoids. All non-hydrogen atoms were refined with anisotropic displacement parameters during the

final cycles, whereas organic hydrogen atoms were located with isotropic displacement parameters set to 1.2 × U_{eq} of the attached atoms. Attempts to locate and refine the strong solvent peaks were successful, but contributions to scattering due to those highly disordered solvent molecules were removed using the *SQUEEZE* routine of *PLATON*; structures were then refined again using the data generated.

The detailed information about the solution and refinement of the single crystal structures can be found in the electronic supplementary materials of this manuscript. Crystallographic data of PCN-501 – PCN-506 are summarized in Appendix A at the end of this dissertation.

5.2.5 Activation Procedures and Gas Sorption Measurements

In order to perform the gas adsorption study, an adequate amount of the products (more than 60 mg) were accumulated by performing identical reactions in multiple vials on the robotic platform before the samples were combined and activated. All the as-synthesized samples must be activated prior to any gas sorption measurements. In order to remove any unreacted starting materials and trapped compounds in their pores, the as-synthesized mixed-ligand MOF samples were treated by solvent exchange with DMA three times and acetone (for PCN-501)/dichloromethane (for PCN-503 and PCN-504) three times for about 12 h each. After the careful removal of acetone by decanting, the sample was transferred into a sorption tube and activated under dynamic vacuum at room temperature for several hours. It was then activated by using the ‘outgas’ function

of the adsorption instrument for 12 h at 100˚C (for PCN-501) / 75˚C (for PCN-503 and PCN-504) prior to any gas adsorption/desorption measurement.

5.2.6 Topological Analysis

All the topological analyses of the crystal structures were performed by using *TOPOS 4.0* Professional. All the non-coordinating solvents and coordinating solvents were removed from the refined crystal structures before they were loaded into the program. An adjacent matrix for this structure was calculated based on the loaded structure. A simplified network that possesses an identical connectivity as the original framework was obtained by dividing the original structure into clusters.

5.2.7 Calculation of Simulated Surface Area

The calculated accessible surface area of each material was estimated using the Atoms Volume & Surface calculation within the *Materials Studio* package. A probe molecule with the diameter equal to the kinetic diameter of Ar (3.542 Å), or N_2 (3.64 Å), [20] was used to determine the accessible surface area.

5.3 Results and Discussion

5.3.1 Structural Characterization of Mixed-Ligand MOFs

Structure and Porosity of PCN-501. Colorless, blocky, single crystals of PCN-501 ($Zn_4O(H_2O)_2$(TCPS)(BDC)) were obtained by a solvothermal reaction between H_4**TCPS**, H_2**BDC** (**BDC**=1,4-benzenedicarboxylate) and $Zn(NO_3)_2 \cdot 6H_2O$ in a mixture

of DMA at 100˚C for 1 day. Single crystal X-ray diffraction reveals that PCN-501 crystallizes in the orthorhombic space group *Pnma*. This MOF consists of $Zn_4(\mu_4\text{-O})$ clusters connected by four **TCPS** linkers and two **BDC** linkers in a distorted-octahedral geometry. Unlike the commonly seen $Zn_4(\mu_4\text{-O})$ clusters with a full O_h symmetry in the MOF-5 series, [14] (Figure V-3(d)), this SBU consists of three of 4-coordinated zinc and one 6-coordinated zinc. The symmetry of this SBU is hence reduced to C_s (Figure V-3(b)). In order to match the lattice symmetry, the tetrahedral ligand **TCPS** has also adopted a C_s symmetry (Figure V-3(a)) and stays at a position where the mirror plane of the SBU is located (Figure V-3(e)). As expected, all the **BDC** linkers exclusively exhibit an inversion symmetry *i* (Figure V-3(c)) and they stay at the positions where the inversion centers are located in the Bravais lattice. (Figure V-3(e)). It is the combination of a mirror plane from the **TCPS** ligand and two independent inversion centers from the **BDC** ligand that has resulted in a framework with an orthorhombic space group (Figure V-3(e)), where all the lattice axes have to remain mutually orthogonal in order to meet all the symmetry requirements from two kinds of linkers.

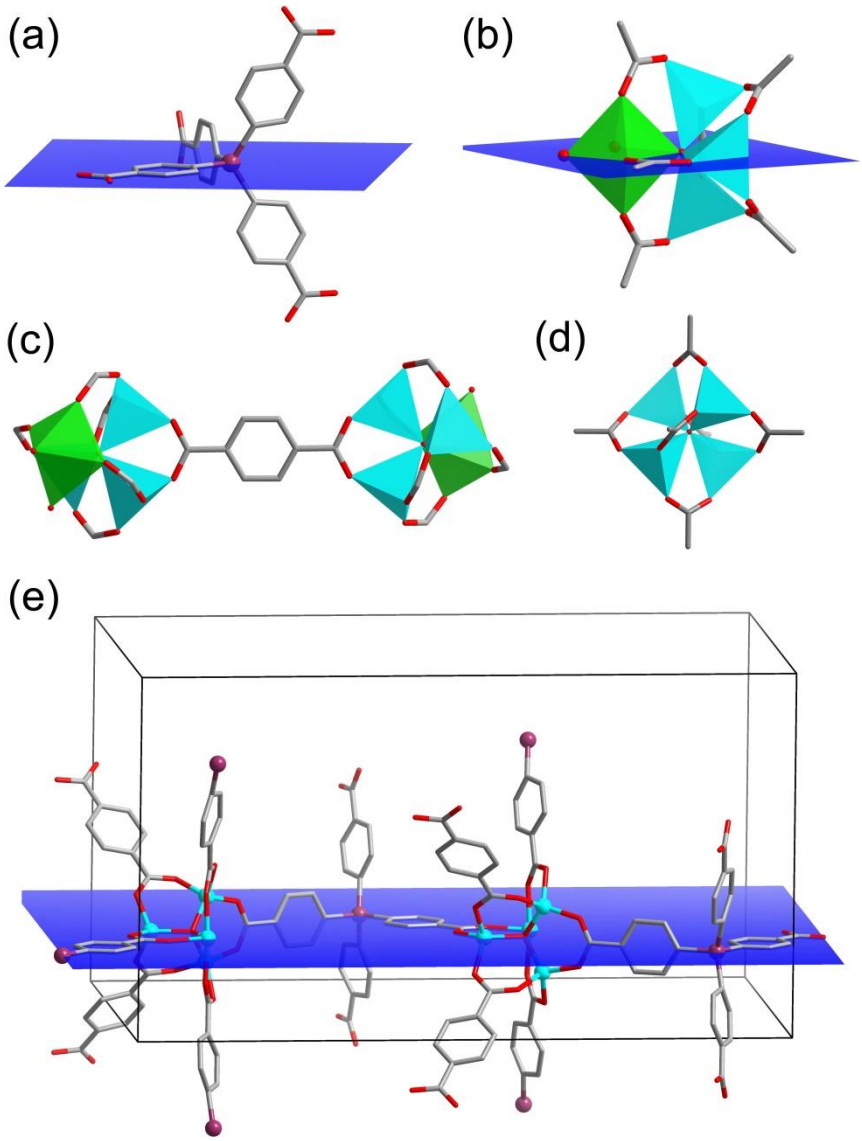

Figure V-3. The crystal structure of PCN-501. (a, b) The **TCPS** ligands and the $Zn_4(\mu_4$-O) clusters have adopted a C_s symmetry. (c) The **BDC** ligands have adopted an inversion symmetry. (d) The commonly-seen $Zn_4(\mu_4$-O) clusters in MOF-5. (e) The **TCPS** ligands and SBUs are located on a mirror plane (hkl=040) in order to meet the Bravais lattice symmetry, while the **BDC** ligands stay at the inversion centers of this lattice. Color Scheme: C: gray; O: red; Si: purple, Zn: cyan. H atoms are omitted for clarity.

Due to the fully extended nature of a tetrahedral ligand, the combination of the **TCPS** ligand, the **BDC** ligand and the SBU has generated two types of cages packing in a 1:1 ratio within the PCN-501 framework, with a large pore size of 13.2 Å and a small pore size of 11.2 Å. (Figure V-4 (a, b)) It should be noted that the symmetry reduction of the tetrahedral ligand (from T_d to C_s) and the SBU (from O_h to C_s) has resulted in a C_s symmetry in both cages. Two linear BDC ligands are necessary for the formation of each cavity. Since the linear ligands exclusively occupy the inversion centers in the MOF Bravais lattice, inversion operation on a particular cage through any inversion center will generate a framework with repetitive identical cages in its lattice. In other words, all the cavities in PCN-501 were packed in a fashion where any of the two adjacent cages that share a BDC ligand are symmetrically correlated with an inversion center. It is this symmetry correlation that has maximized the packing efficiency of the cavities and resulted in the high porosity of this MOF. (Figure V-4(c)) The calculated solvent accessible volume of PCN-501 is 71.60%, a value larger than many other microporous MOFs. Its porous nature can be further confirmed by the subsequent gas sorption measurements.

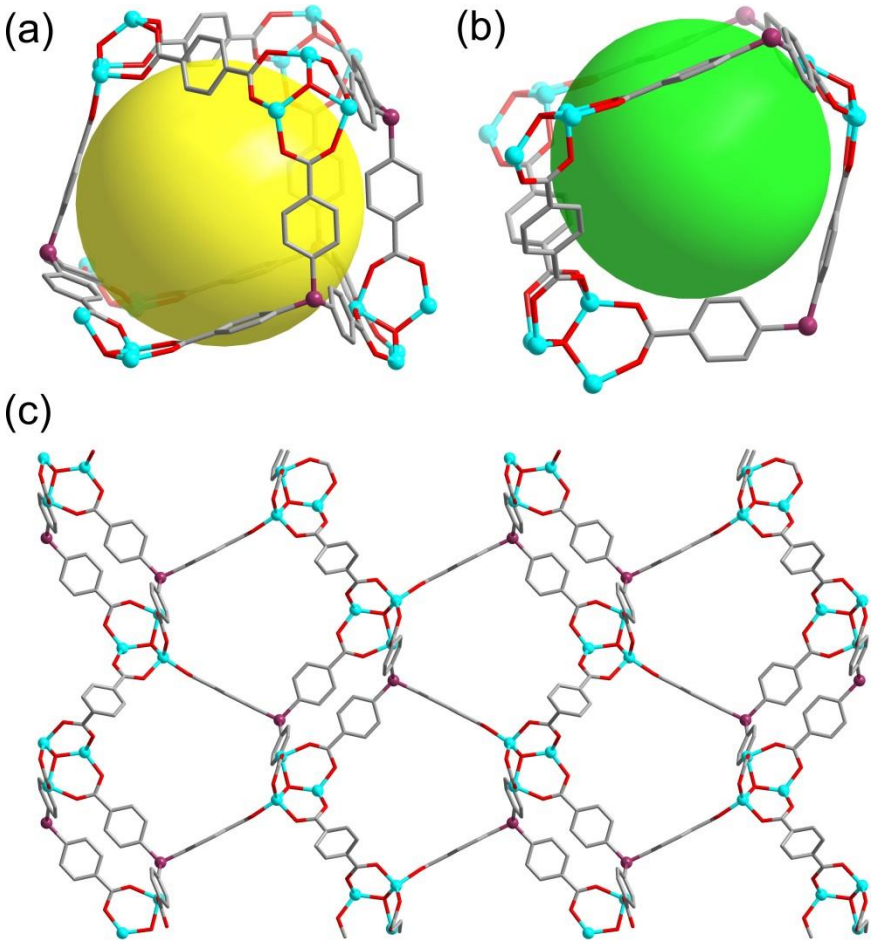

Figure V-4. (a, b) Two different cages in PCN-501. The yellow and green spheres indicate the empty spaces inside these cages. (c) The crystal structure of PCN-501. Color Scheme: C: gray; O: red; Si: purple, Zn: cyan. H atoms are omitted for clarity.

Structure and Porosity of PCN-502. Colorless, blocky, single crystals of PCN-502 ($Zn_7O_2(OH)_4(TCPS)_2$(2,6-NDC)) were obtained by a solvothermal reaction between H_4**TCPS**, H_2**2,6-NDC** (**2,6-NDC**=2,6-Naphthalenedicarboxylate) and $Zn(NO_3)_2 \cdot 6H_2O$ in a mixture of DMA/NMP at 75˚C for 3 days. Single crystal X-ray diffraction reveals that PCN-502 crystallizes in the monoclinic space group $P2_1/m$.

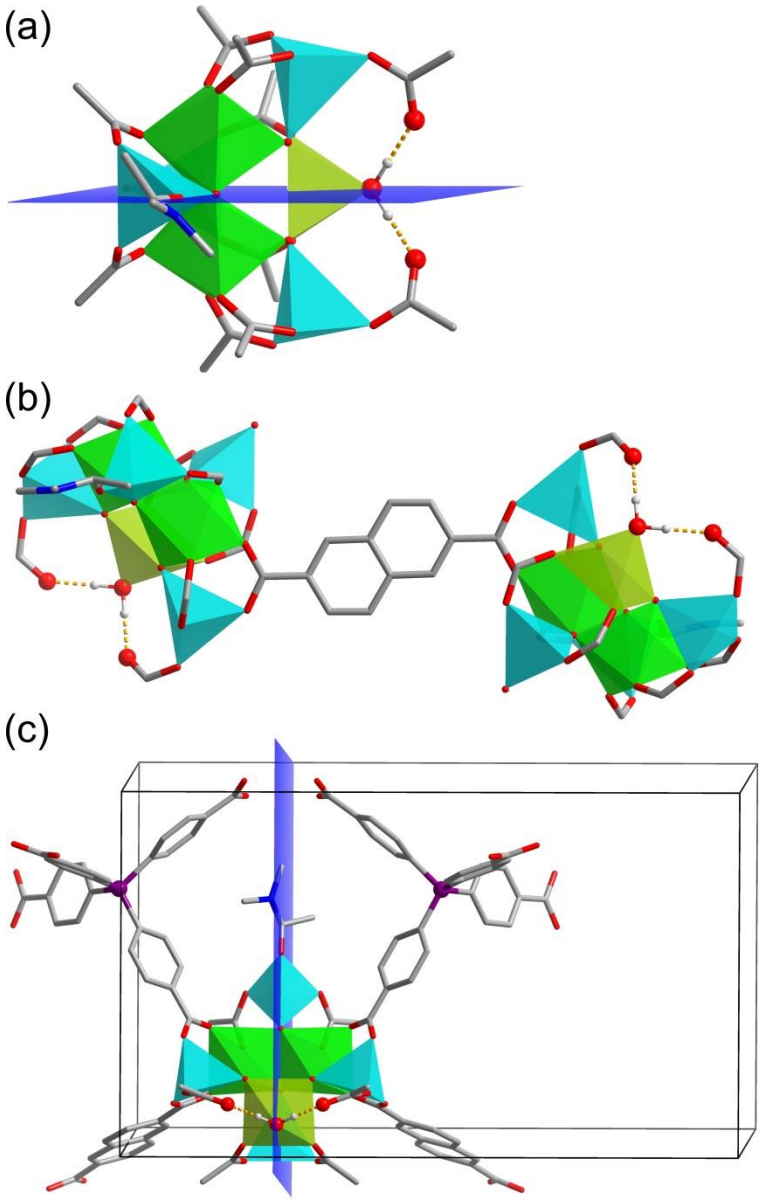

Figure V-5. The crystal structure of PCN-502. (a) The Zn_7 cluster discovered in PCN-502 possesses a C_s symmetry. (b) The **2,6-NDC** ligand exhibits an inversion symmetry. (c) The SBUs are located on a mirror plane (hkl=040), and the **2,6-NDC** ligands are located on inversion centers. Color Scheme: C: gray; O: red; Si: purple, Zn: cyan. H atoms are omitted for clarity.

This MOF consists of a novel Zn_7 cluster with inherent mirror symmetry. This is a rarely seen SBU with inherent hydrogen bonds, where a water molecule residing on a 5-coordinated zinc is connected with two adjacent carboxylates through two hydrogen bonds that are related to a mirror plane. (Figure V-5(a)). The TCPS ligand is located outside this mirror plane, and it possesses a C_1 symmetry in this MOF. Similarly, all the **2,6-NDC** linkers exclusively exhibit an inversion symmetry *i* (Figure V-5(b)) and stay at a position where the inversion center is located in this Bravais lattice (Figure V-5(c)). This MOF possesses a solvent accessible volume of 59.80%. This is a larger value than many MOFs made exclusively from **TCPS** ligands. [52]

Structure and Porosity of PCN-503 and PCN-504. Both PCN-503 ($(Zn_4O)_2(TCPS)_3(BPDC)$) and PCN-504 ($(Zn_4O)_2(TCPS)_3(BDA)$) are identified as blocky, colorless single crystals from solvothermal reactions in DMA between the **TCPS** ligand, $Zn(NO_3)_2{\cdot}6H_2O$, and the corresponding linear ligands: biphenyl-4,4'-dicarboxylate (BPDC) for PCN-503 and 1,4-benzenediacrylate (BDA) for PCN-504. Both of them crystallize in the monoclinic space group *C*2/*c*. Due to the similar length of the **BPDC** and **BDA** linkers, these two MOFs possess extremely similar structures. They consist of 7-connected $Zn_4(\mu_4\text{-}O)$ clusters, where the additional carboxylate has lowered the symmetry of this cluster from O_h to C_1. (Figure V-6(a)) This cluster is also observed in PCN-515. In order to fit in the lattice symmetry, the **TCPS** ligands have to adopt a C_2 symmetry. (Figure V-6(b)) As expected, all the linear linkers exhibit inversion symmetry in their structures. (Figure V-6(c, d)) The calculated solvent accessible volume of PCN-503 and PCN-504 are 69.90% and 71.40%, indicating their significantly

porous nature. Due to the anionic nature of these frameworks, counterions should exist in their cavities in order to balance the negative charge on their frameworks. These counterions cannot be crystallographically identified, but their existence is implied by the discrepancy between the simulated and experimental surface areas.

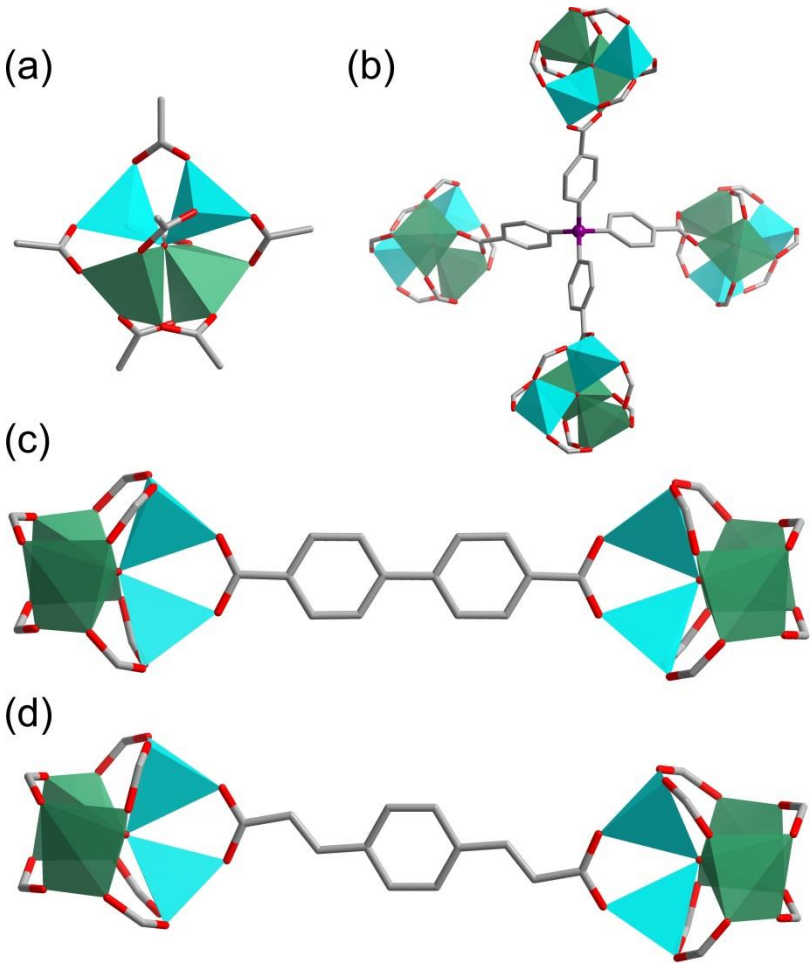

Figure V-6. (a) The 7-connected Zn_4O clusters. (b) The **TCPS** ligands possess a C_2 symmetry. (c, d) The **BPDC** and **BDA** linkers possess inversion symmetry. Color Scheme: C: gray; O: red; Si: purple, Zn: cyan. H atoms are omitted for clarity.

Structure and Porosity of PCN-505 and PCN-506. Single crystals of PCN-505 (Zn_4O_3(TCPS)(1,4-NDC)) and PCN-506 (Zn_4O_3(TCPS)(2-NH_2-BDC)) are obtained from the solvothermal reaction between in DMA between the **TCPS** ligand, $Zn(NO_3)_2 \cdot 6H_2O$, and the corresponding linear ligands: 1,4-naphthalenedicarboxylate (1,4-NDC) for PCN-505 and 2-aminoterephthalate (2-NH_2-BDC) for PCN-506. Both of them crystallize in orthorhombic space group *Pnma*. They are identical structures to PCN-501 except that the original BDC linkers in PCN-501 are replaced by 1,4-NDC or 2-NH_2-BDC. It should be noted the linear coligands in these two MOFs do not possess inherent inversion symmetry. An inversion center was spontaneously created by the crystallographic disorder, where two linear ligands with opposite orientation overlap with each other. This has resulted in a "*pseudo*" inversion symmetry in these linear ligands. (Figure V-7) Since these ligands have the same length as BDC, their combination with the TCPS ligands has generated MOFs isostructural to PCN-501.

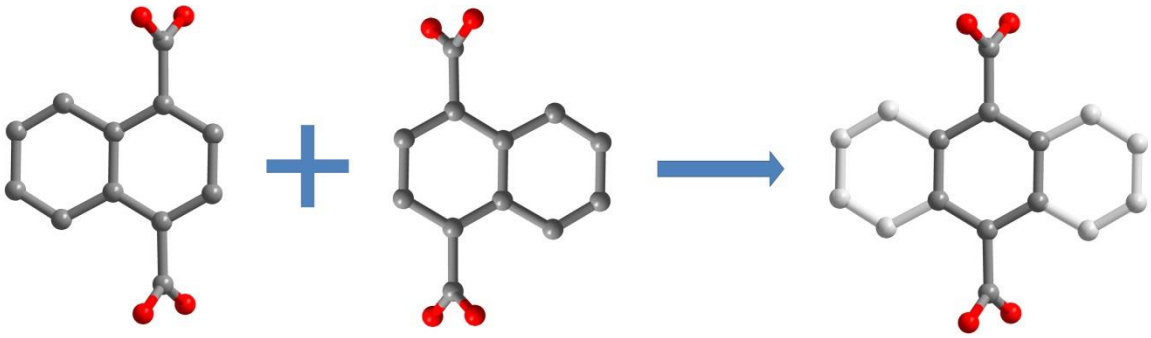

Figure V-7. A "*pseudo*" inversion symmetry can be created by crystallographic disorder when linear ligands without inversion centers are utilized to create mixed-ligand MOFs.

5.3.2 Coordination Copolymerization of Mixed-Ligand MOFs

The coordination copolymerization process that assembles mixed-ligand MOFs are primarily controlled by both a geometric factor and a statistical factor.[168] The geometric factor includes the length ratio between the tetrahedral ligand $\mathbf{L_0}$ and linear ligands $\mathbf{L_x}$ (x=1-6) and the geometry / connectivity of the SBUs. The statistical factor includes the feed ratio of the two linkers and their relative reactivity. Small changes in the $\mathbf{L_0}/\mathbf{L}_x$ length ratio can yield distinct copolymerization structures. As the length of the linear linker is elongated, the feed ratio of $\mathbf{L_0}/\mathbf{L}_x$ that favors the formation of mixed-ligand MOFs is reduced. (Scheme V-3) This means an increased concentration of linear ligands are required for the formation of mixed-ligand MOFs. Nevertheless, in their single crystal structures, the molar ratio of $\mathbf{L_0}/\mathbf{L}_x$ is decreased as a longer linear ligand is utilized. This should probably be attributed to decreased reactivity in elongated ligands. In general, for two ligands with the same symmetry (for example, linear ligands with inversion symmetry), the larger ligand usually possesses a larger degree of freedom. This means it is more likely to suffer from more undesired rotation and distortion during its crystallization process, and thus it is less likely to be crystallized in the same condition than a smaller ligand is. This is consistent with the observation of this experiment: As a longer linear ligand is utilized, an increased concentration of linear ligands should be used in the solvothermal reactions, while a decreased ratio of linear ligands are incorporated into the mixed-ligand MOFs.

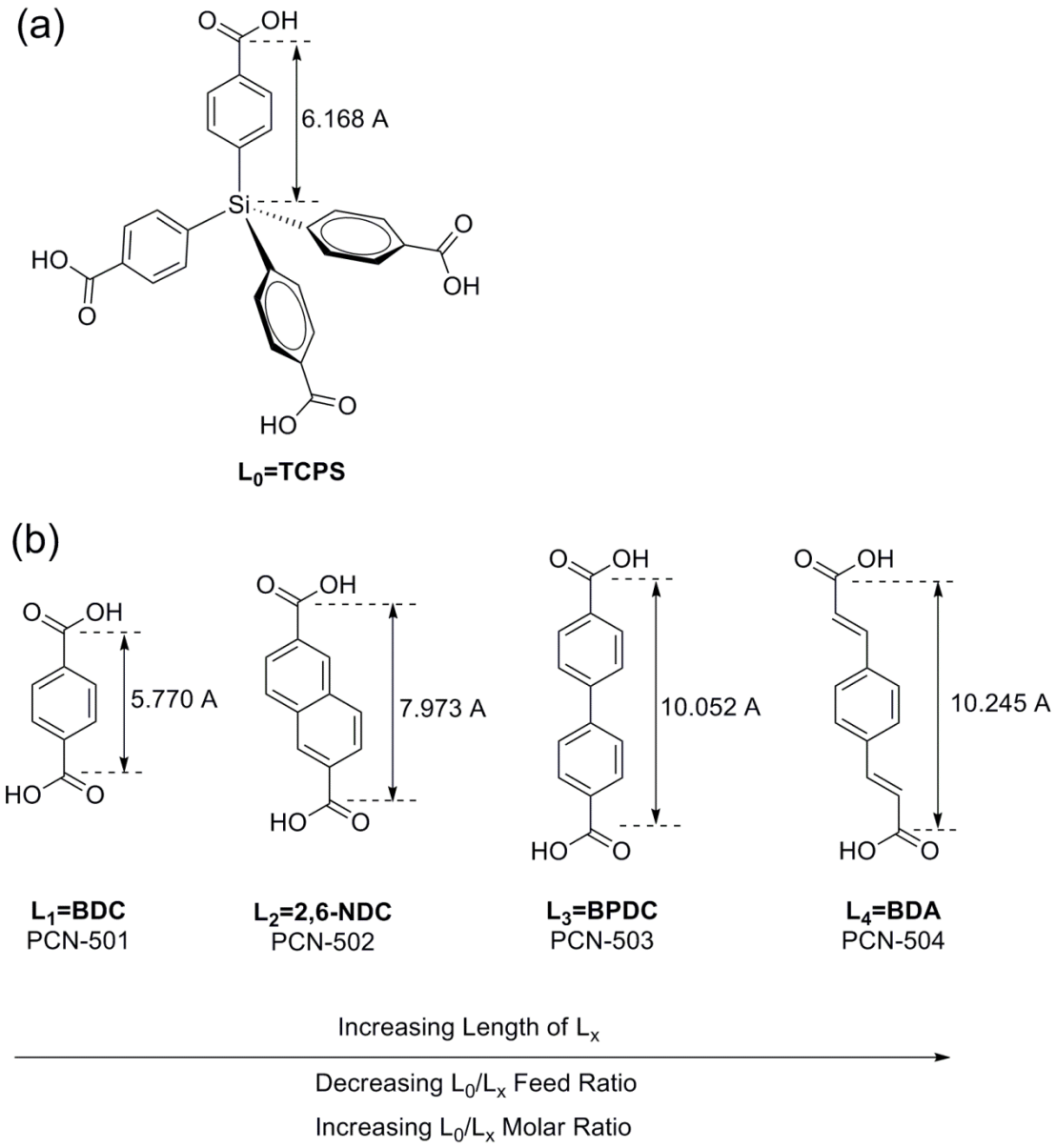

Scheme V-3. The coordination copolymerization process is largely affected by the length ratio of $\mathbf{L_0/L_x}$. Increasing $\mathbf{L_x}$ length will result in a decreased $\mathbf{L_x}$ proportion (and thus an increased $\mathbf{L_0/L_x}$ ratio) in the resulting mixed-ligand MOF structures.

The successful construction of PCN-505 and PCN-506 indicates the same coordination copolymerization process can occur between two ligands without inversion centers. Their structures consist of the overlapping of two crystallographically disordered linear ligands with opposite orientations, resulting in a "*pseudo*" inversion symmetry that is located at the inversion centers in the MOF's Bravais lattice.

Table V-2 lists all the geometrical factors that affect the coordination copolymerization processes of mixed-ligand MOFs.

Table V-2. The geometrical factors that affect the formation of mixed-ligand MOFs

MOF	Co-ligand	Co-ligand Molecular Symmetry	Co-ligand Lattice Symmetry	SBU Lattice Symmetry	TCPS Lattice Symmetry	L_0/L_x Length Ratio [a]	L_0/L_x Feed Ratio [b]	Actual Molar Ratio [c]	Space Group
PCN-501	BDC	D_{2h}	*i*	C_s	C_s	1.069	1 : 1.45	1:1	*Pnma*
PCN-502	2,6-NDC	C_{2h}	*i*	C_s	C_1	0.774	1 : 1.85	2:1	$P2_1/m$
PCN-503	BPDC	D_{2h}	*i*	C_1	C_2	0.614	1 : 2.55	3:1	$C2/c$
PCN-504	BDA	C_{2h}	*i*	C_1	C_2	0.602	1 : 3.26	3:1	$C2/c$
PCN-505	1,4-NDC	C_{2v}	*pseudo i*	C_s	C_s	1.091	1 : 2.35	1:1	*Pnma*
PCN-506	2-NH_2-BDC	C_s	*pseudo i*	C_s	C_s	1.069	1 : 2	1:1	*Pnma*
PCN-511 [d]	N/A	N/A	N/A	*i*	C_1	N/A	N/A	N/A	$C2/c$
PCN-515 [d]	N/A	N/A	N/A	C_1 [e]	C_1 [e]	N/A	N/A	N/A	$P2_1/c$

[a] L_0 = tetrahedral ligand; L_x = linear ligand.

[b] The feed ratio indicates the optimized L_x/L_0 molar ratio in solvothermal reactions.

[c] The actual molar ration indicates the L_x/L_0 molar ratio in their single crystal structures.

[d] PCN-511 and PCN-515, two MOFs made only by the TCPS ligand, are listed for comparison. [52]

[e] PCN-515 consists of three distinct types of SBU and four topologically different TCPS ligands.

5.3.3 Porosity and Gas Sorption Study

Due to the 3D fully-extended nature of the tetrahedral ligand, all the mixed-ligand MOFs are intrinsically porous. Gas adsorption measurements were performed on selected mixed-ligand MOF samples. The fresh samples of PCN-501, PCN-503 and PCN-504 were properly activated according to the aforementioned procedures. PCN-501 exhibits a type-I isotherm of N_2 sorption at 77 K and 1 bar (Figure V-8(a)), implying the existence of the micropores. Its Langmuir surface area, Brunauer−Emmett−Teller (BET) surface area, and pore volume are 3192 $m^2 \cdot g^{-1}$, 3090 $m^2 \cdot g^{-1}$, and 1.13 $cm^3 \cdot g^{-1}$, respectively. When Ar was used, its Langmuir surface area, BET surface area, and pore volume are 3515 $m^2 \cdot g^{-1}$, 3289 $m^2 \cdot g^{-1}$, and 1.18 $cm^3 \cdot g^{-1}$, respectively. (Figure V-8(b))

In particular, this MOF possesses the second largest BET surface area among all the existing MOFs made from tetrahedral ligands. (See Table III-1 in Chapter III) There is a growing interest in surface area per unit volume (volumetric surface area), as it is more relevant for gas storage in mobile applications. The calculated surface area per unit volume for PCN-501 is 2151 $m^2 \cdot cm^{-3}$. Note that PCN-521 has a larger BET surface area than that of PCN-501; however, its volumetric surface area (1617 $m^2 \cdot cm^{-3}$) is significantly smaller than that of PCN-501, owing to its wide open cavities. [48] PCN-501 possesses the largest surface area per volume among all the MOFs made from tetrahedral linkers. In addition, compared to PCN-521, the ligand synthesis of PCN-501 does not involve the utilization of any expensive reagents or complicated chromatographic separation processes. This will make it convenient to scale up the production of PCN-501 for its desirable applications.

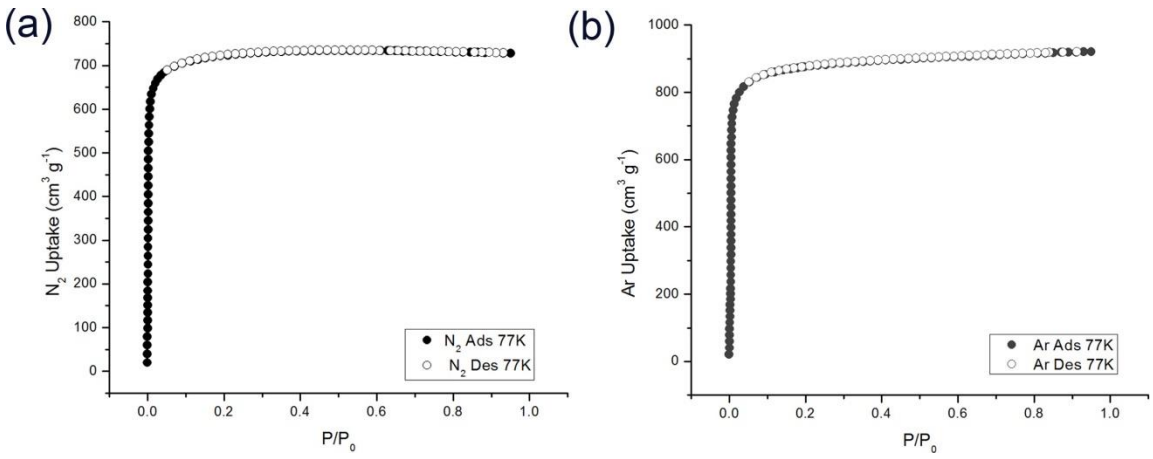

Figure V-8. (a) The N_2 sorption isotherms of PCN-501 at 77 K. (b) The Ar sorption isotherms of PCN-501 at 77 K.

The porosities of PCN-503 and PCN-504 were also investigated by gas adsorption measurements. Despite their ionic nature, their frameworks still possess permanent porosity after proper activation process with considerably large surface areas. Both of them exhibit a type-I isotherm of N_2 sorption at 77K and 1 bar, with the BET surface area of 1808 $m^2 \cdot g^{-1}$ for PCN-503, and 2504 $m^2 \cdot g^{-1}$ for PCN-504. Their volumetric surface areas are 1206 $m^2 \cdot cm^{-3}$ and 1675 $m^2 \cdot cm^{-3}$, respectively.

5.4 Summary

In summary, this work has demonstrated a successful implementation of rational design of mixed-ligand MOFs by unravelling the relationship between a MOF's Bravais lattice symmetry and the point group symmetry of its fundamental building blocks. By judicious selection of two ligands that are symmetrically complementary with each other, mixed-ligand MOFs can be constructed by combining a non-centrosymmetric ligand

(with reflectional symmetry or rotational symmetry) with a centrosymmetric ligand (with an inversion center). This hypothesis was substantiated by successful construction of a series of MOFs from a commercially affordable tetrahedral ligand combined with various linear linkers. All the linear ligands in these mixed-ligand MOFs exclusively exhibit either true or pseudo inversion symmetry, regardless of whether their molecular symmetries possess inversion centers or not. The employment of high throughput-synthesis has significantly improved the experimental efficiency, and greatly facilitated the discovery of these MOFs.

Utilization of this symmetry-guided design strategy yields six mixed-ligand MOFs, PCN-501 – PCN-506, all of which are novel structures with potential high porosity, with solvent accessible volumes up to 71.60%, BET surface areas up to 3090 $m^2 \cdot g^{-1}$, and surface areas per unit volume up to 2151 $m^2 \cdot cm^{-3}$. This is the largest volumetric surface area that is observed among MOFs made from tetrahedral linkers so far. All these MOFs are the first reported mixed-ligand MOFs made from tetrahedral ligands. In particular, the presence of the linear co-ligands has significantly improved their porosities over the MOFs made purely by the corresponding tetrahedral ligand. (Table V-3) This work not only elucidates a general method of rational design of mixed-ligand MOFs from desired geometries, but also sheds light on the rational design of other complicated multicomponent systems, such as co-crystals [180, 181] and co-polymers.[182, 183]

Table V-3. The porosities and surface areas of the mixed-ligand MOFs

MOF	Co-ligand	Space Group	Solvent Accessible Volume %	BET SA Using N_2 ($m^2 \cdot g^{-1}$) [a]	SA per Volume ($m^2 \cdot cm^{-3}$)	BET SA Simulated Using N_2 [b]	BET Simulated Using Ar [b]
PCN-501	BDC	*Pnma*	71.60	3090	2151	3185	3226
PCN-502	2,6-NDC	$P2_1/m$	59.80	N/A	N/A	1699	1748
PCN-503 [c]	BPDC	*C*2/*c*	69.90	1808	1206	3108	3168
PCN-504 [c]	BDA	*C*2/*c*	71.40	2504	1675	3111	3165
PCN-505	1,4-NDC	*Pnma*	65.40	N/A	N/A	2704	2737
PCN-506	2-NH_2-BDC	*Pnma*	67.40	N/A	N/A	3094	3140
PCN-511 [d]	N/A	*C*2/*c*	45.50	703	698	1187	1273

[a] SA = Surface Area.

[b] Calculated by the *Materials Studio* package. All the solvents are removed before the simulation.

[c] The discrepancy between simulated and experimental data for PCN-503 and PCN-504 are resulted from their ionic natures.

[d] PCN-511 is a MOFs made only by the TCPS ligand, and it is listed for comparison. [52]

CHAPTER VI

DESIGN AND SYNTHESIS OF METAL-ORGANIC MATERIALS WITH BIOMIMETIC FEATURES [*†]

6.1 Introduction

Naturally occurring materials are renowned for their combination of a great number of inspirational attributes that have been seldom observed in traditionally-used artificial materials, such as sophistication, miniaturization, hierarchical organization, and hybridization. [184, 185] Evolution has optimized biological materials and biological processes for more than 3.8 billion years since the emergence of unicellular simple cells (*i.e.* prokaryotes), [186] which has resulted in the structural and functional variety of biological molecules on the planet Earth. Researchers have increasingly been looking to nature for inspiration to design novel breakthrough technology and to solve previously long-standing problems. Biomimicry is the study of the structure and function of biological systems, for the purpose of synthesizing materials that mimic natural ones. The goal is to use these observations of nature to create materials that are both more compatible with life and provide functionality that has previously not been seen in artificial materials. Biomimicry is on the forefront of scientific and technological

[*] Reproduced in part with permission from "Design and Synthesis of Nucleobase-Incorporated Metal-Organic Materials", by Zhang, M.; Lu, W.; Li, J.-R.; Bosch, M.; Chen, Y.-P.; Liu, T.-F.; Liu, Y.; Zhou, H.-C., *Inorg. Chem. Front.* **2014**, *1*, 159-162, copyright 2014 by Royal Society of Chemistry.

[†] Reproduced in part with permission from "Biomimicry in Metal-Organic Materials", by Zhang, M.; Gu, Z.-Y.; Bosch, M.; Perry, Z.; Zhou, H.-C., *Coord. Chem. Rev.*, accepted, copyright 2014 by Elsevier B.V.

research, because it brings about novel insights for the synthesis of biologically-compatible, environmentally-friendly and energetically-efficient materials. [187]

Metal-organic materials (MOMs) are discrete or polymeric chemical architectures that consist of both metal units and organic linkers. While the presence of MOMs can be dated back to 1950s, [188] they have gained an increasing amount of attention in recent years due to their intriguing structures and diverse applications. [2, 3] Metal-organic frameworks (MOFs) and metal-organic polyhedra (MOPs) are two important categories of MOMs. In biomimetic chemistry, while many other accomplishments have been achieved in areas such as artificial enzymes, [189-201] artificial bones, [202-215] biomimetic catalysts, [216-223] biomimetic membranes, [224-232] tissue engineering, [233-242] and many other related areas, research on biomimetic MOMs still remains underdeveloped in comparison to the rapid growth of MOF/MOP chemistry.

Nature has evolved a great number of biological molecules which serve as excellent constructional or functional units for MOFs. By taking advantage of the structural and functional diversity of biological molecules, it is suggested that the incorporation of biomimetic units into MOFs will further enrich the variety of MOF architectures and applications, as the exploration of new structures or functions of MOFs is the core activity of MOF research. In a recent highlight review from our group, we have classified the contemporary progress on rational MOF designs into a structural and a functional approach. [49] Similarly, in this chapter, we would like to categorize the recent advances of biomimetic MOFs into those two distinct catalogs as well. The structural approach includes the incorporation of biological molecules into MOFs to explore new

possible structures, while the functional approach involves the incorporation of biological/biomimetic components into MOFs to investigate their new possible applications. (Scheme V-1)

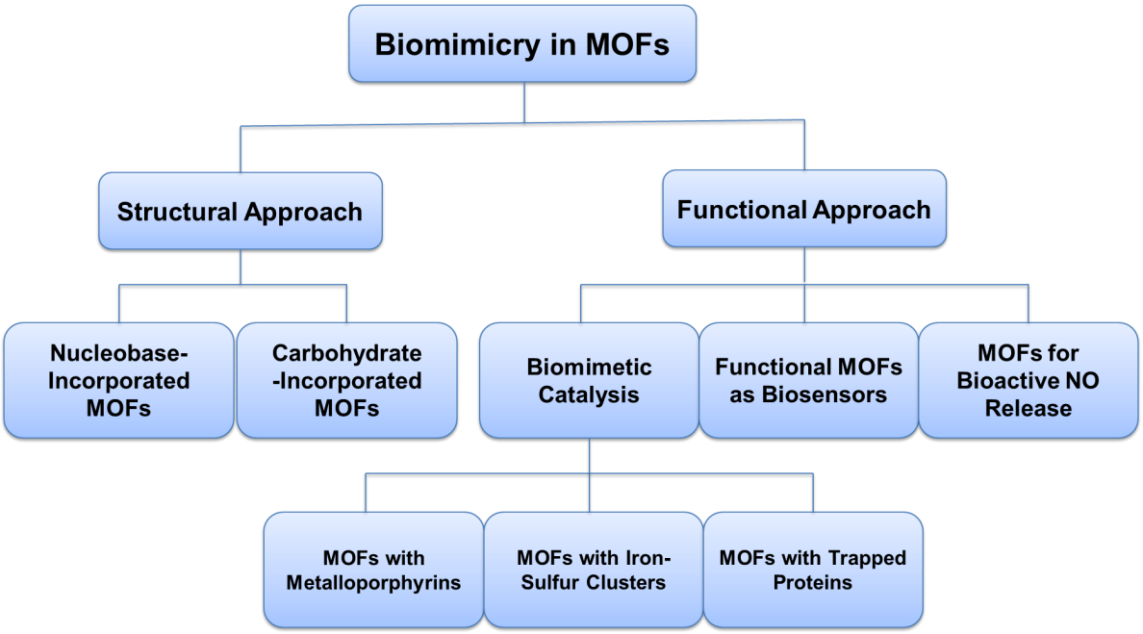

Scheme VI-1. Recent progress on biomimetic MOFs can be catalogued into two different approaches: a structural approach and a functional approach.

Many biomolecules, such as amino acids, oligopeptides, proteins, nucleobases, and saccharides, are naturally good ligands and have already been successfully incorporated into coordination polymers. However, some restrictions generally prevent these biomolecules from being good candidates as MOF constituents. The symmetry deficiency in many biological building blocks makes the synthesis of ordered materials (such as MOMs) much more difficult, where the utilization of high-symmetry

constructional components will significantly facilitate the packing of the repetitive units to form crystalline materials. Additionally, aside from some aromatic molecules and a few cyclic non-aromatic molecules, most biomolecules are too flexible to generate a framework with potential permanent porosity. To overcome this problem, several different strategies were developed by MOF scientists: first, to construct MOFs with highly-symmetric secondary building units (SBUs) from asymmetric biological ligands; second, to introduce a highly-symmetric co-ligand to offset the low-symmetry nature of biomolecules; and third, to utilize a cyclic oligomer consisting of "small molecules" with lower symmetry.

Nucleobases are of central significance of the emergence, maintenance and proliferation of life on the planet Earth. With the selectivity of these base pair interactions, nucleobases are excellent components to construct supramolecular structures. [243] At the same time, nucleobases appear to be good ligands for coordination compounds as well. The presence of accessible nitrogen and oxygen lone pairs has brought about a rich field of nucleobase coordination chemistry. [244] For a single nucleobase, it is possible for metal ions to coordinate with almost any site of the molecules. This coordination versatility has led to the investigation of nucleobase-incorporated MOMs.

Even though much effort has been made in the exploration of their novel structures and diverse applications in the past two decades, the area of nucleobase-incorporated MOMs still remains largely under-developed. However, it is highly desirable to construct nucleobase-incorporated MOMs for the following reasons. First,

materials with nucleobase moieties on its surfaces are promising materials for biological sensors [245] and gene regulators [246]. A traditional way of making nucleobase-incorporated materials typically involves coating DNA/RNA moieties onto the surface of gold nanoparticles. [245-249] However, the majority of these materials cannot be obtained in their crystalline form. By incorporating the DNA/RNA moieties into MOMs, crystalline materials may be obtained [167, 176, 250-252], which should largely simplify their structural characterization and enable us to study their biological interactions. Second, the nucleobases are naturally excellent ligands. They possess multiple metal-binding sites and coordinate to metal units in various fashions. [244] The introduction of nucleobases into the framework can significantly enrich the coordination chemistry in MOMs and bring about intriguing structures. Third, many potential MOM applications require them to be biologically- and environmentally-friendly. [253] The utilization of nucleobases will largely enhance their biological and environmental compatibility. Fourth, production cost is always a primary concern of any industrial application of MOMs with large quantity. [52] Due to their natural abundance and easy production process, the introduction of small biomolecules into MOMs may significantly bring down the production cost.

In this work, two nucleobase-incorporated MOMs were designed, synthesized and structurally characterized. PCN-530 is among the few examples of MOFs that utilize adenine as a constructional unit; while TMOP-1 (TMOP represents Thymine-incorporated Metal-Organic Polyhedron) is the first existing example of crystallographically characterized nucleobase-incorporated metal-organic polyhedron.

This work also offers a general perspective for the design and synthesis of nucleobase-incorporated metal-organic materials.

6.2 Experimental Section

6.2.1 Materials and Instrumentation

The H_3**TATB** (4,4*'*,4*''*-*s*-triazine-2,4,6-triyl-tribenzoic acid) was synthesized by a reported procedure. [254] All commercial chemicals were purchased from VWR and used without further purification unless otherwise mentioned. The dry THF was produced by a THF still. ^{1}H nuclear magnetic resonance (NMR) data were recorded on a Mercury 300 MHz NMR spectrometer at the Center for Chemical Characterization and Analysis (CCCA), Department of Chemistry, Texas A&M University. Fourier transform infrared spectroscopy (FTIR) data were collected using a SHIMADZU IRAffinity-1 FTIR Spectrophotometer.

6.2.2 Ligand Synthesis

The ligand H_2**MDPI** (5-((5-methyl-2,4-dioxo-3,4-dihydropyrimidin-1(2H)-yl) methyl)isophthalic acid) was synthesized from the following route (Scheme VI-2).

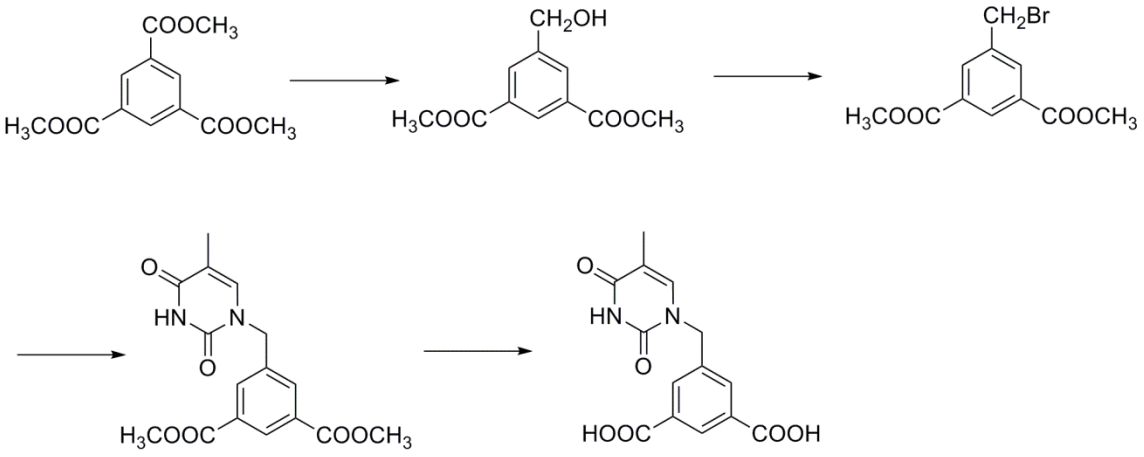

Scheme VI-2. The synthesis of H_2**MDPI** ligand.

Synthesis of dimethyl-5-(hydroxymethyl)isophthalate. Dimethyl-5-(hydroxymethyl)isophthalate was synthesized by a reported procedure with some modifications. [255] Trimethyl-1,3,5-tricarboxybenzoate (10 g, 39.65 mmol), $NaBH_4$ (1.8 g, 47.58 mmol) and 30 mL dry THF were charged in a round bottom flask equipped with a condenser under N_2 atmosphere. The resulting suspension was cooled in ice bath. A mixture of THF/MeOH (25 mL/7.4 mL) was added dropwise while stirring. After the addition, the ice bath was removed, and the reaction mixture was refluxed for 1 h. After cooling down to R. T., the reaction was slowly quenched with 40 mL 1 N HCl. The reaction mixture was then extracted with EtOAc (3 × 50 mL). The organic phase was combined and washed with $NaHCO_3$ (*aq*), brine, and water, and then dried over anhydrous $MgSO_4$. After filtration, the solvent was removed by rotavap, and the crude product was purified by silica gel column chromatography with EtOAc/hexanes (40%) to afford 5.30 g (23.60 mmol, yield 60%) pure product as white solid. Analytical data

were in good agreement with the reported data. ^{1}H NMR (300 MHz, $CDCl_3$): δ = 8.59 (t, J = 1.5 Hz, 1H), 8.23 (d, J = 1.5 Hz, 2H), 4.81 (d, J = 6.0 Hz, 2H), 3.95 (s, 6H), 1.98 (t, J = 6.0 Hz, 1H).

Synthesis of dimethyl-5-(bromomethyl)benzene-1,3-dioate. Dimethyl-5-(bromomethyl)benzene-1,3-dioate was synthesized by a reported procedure with some modifications. [256] To a solution of dimethyl-5-(hydroxymethyl)isophthalate (4.0 g, 17.84 mmol) and carbon tetrabromide (6.1 g, 18.39 mmol) in 50 mL CH_2Cl_2, cooled to 0˚C, was added dropwise a solution of triphenylphosphine (5.0 g, 19.06 mmol) in 30 mL CH_2Cl_2. The reaction was stirred at 0˚C for 1.5 h, diluted with another 50 mL of CH_2Cl_2, washed with water and brine, dried over $MgSO_4$. After filtration, the solvent was removed by rotavap, and the crude product was purified by silica gel column chromatography with CH_2Cl_2 to afford 4.5 g (15.67 mmol, yield 88%) pure product as white solid. Analytical data were in good agreement with the reported data. ^{1}H NMR (300MHz, $CDCl_3$): δ = 8.63 (t, J = 1.5 Hz, 1H), 8.27 (d, J = 1.5 Hz, 2H), 4.56 (s, 2H), 3.98 (s, 6H).

Synthesis of dimethyl 5-((5-methyl-2,4-dioxo-3,4-dihydropyrimidin-1(2H)-yl)methyl) isophthalate. To a mixture of thymine (0.65 g, 5.15 mmol) and K_2CO_3 (0.73 g, 5.29 mmol) in 20 mL DMF, dimethyl-5-(bromomethyl)benzene-l,3-dioate (0.50 g, 1.74 mmol) was added slowly at room temperature in 5 min. The resulting mixture was heated up to 60˚C overnight. After cooling down, 100 mL of water was added, and then extracted with EtOAc (6 × 25 ml). The organic phase was dried over $MgSO_4$. After filtration, the solvent was removed by rotavap, and the crude product was purified by

silica gel column chromatography with EtOAc/CH_2Cl_2 (10 – 40%) to afford 0.48 g (1.44 mmol, yield 83%) pure product as white solid. ^{1}H NMR (300MHz, DMSO-d_6): δ = 11.36 (s, 1H), 8.39 (t, J = 1.5 Hz, 1H), 8.15 (d, J = 1.5 Hz, 2H), 7.73 (d, J = 1.2 Hz, 1H), 4.95 (s, 2H), 3.87 (s, 6H), 1.73 (d, J = 1.2 Hz, 3H).

Synthesis of 5-((5-methyl-2,4-dioxo-3,4-dihydropyrimidin-1(2H)-yl)methyl)isophthalic acid, H_2MDPI. To a mixture of the dimethyl 5-((5-methyl-2,4-dioxo-3,4-dihydropyrimidin-1(2H)-yl)methyl) isophthalate (0.72 g, 2.17 mmol) in MeOH/H_2O (100 mL/40 mL), LiOH (0.60 g, 14.3 mmol) was slowly added. The resulting mixture was stirred at room temperature overnight. After removal of the majority of MeOH *in vacuo*, and the rest part of reaction mixture was acidified with 1 N HCl till pH = 2. Precipitate was collected and washed with water twice, dried to afford pure product (0.45 g, 1.48 mmol, yield 68%) as white solid. ^{1}H NMR (300MHz, DMSO-d_6): δ = 13.37 (s, 2H), 11.39 (s, 1H), 8.39 (t, J = 1.5 Hz, 1H), 8.10 (d, J = 1.5 Hz, 2H), 7.74 (d, J = 1.2 Hz, 1H), 4.96 (s, 2H), 1.76 (d, J = 1.2 Hz, 3H).

6.2.3 Synthesis of Nucleobase-Incorporated MOMs

Synthesis of PCN-530, $Zn_3[Zn_2(\mu_2\text{-}H_2O)]_3(Ad)_6(TATB)_4(DMF)$. Adenine (16.9 mg, 0.125 mmol), H_3TATB (74 mg, 0.17 mmol) and $Zn(OAc)_2{\cdot}2H_2O$ (83 mg, 0.375 mmol) were ultrasonically dissolved in 10 mL of DMF in a 20 mL Pyrex vial and many white precipitates formed instantaneously. A minimal amount of concentrated HBF_4 (48% w/w in water) were added dropwise to dissolve all the precipitate and make it a clear solution before deionized water (1 mL) was added. The mixture was then

heated in a 120 ℃ oven for 48 h. Large, colorless, blocky single crystals of PCN-530 were yielded and harvested (26 mg, 39% based on adenine).

Synthesis of TMOP-1, $Cu_{24}(MDPI)_{24}(DMA)_4(H_2O)_{20}$. The synthesis of TMOP-1 is illustrated in Scheme VI-3.

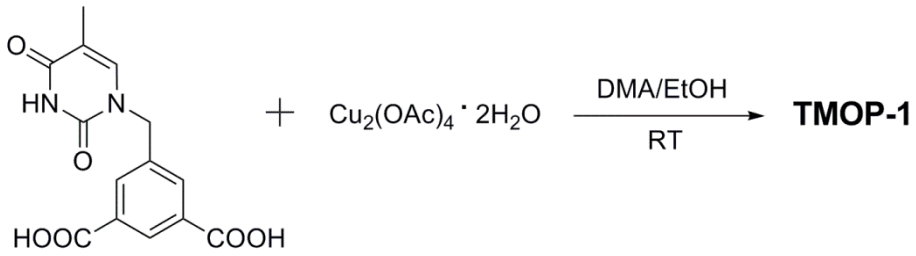

Scheme VI-3. The synthesis of TMOP-1.

An *N, N'*-dimethylacetamide (DMA) solution (1 mL) of H_2MDPI (15 mg, ~0.05 mmol) was mixed with a DMA solution (10 mL) of $Cu_2(OAc)_4 \cdot 2H_2O$ (10 mg, ~0.025 mmol) in a glass vial (4 mL) and stirred for 5 min at room temperature. After stirring, 1.5 mL EtOH was layered upon this solution, and then the vial was allowed to stand at room temperature. After 5 days homogeneous green-blue blocky crystals of $Cu_{24}(MDPI)_{24}(DMA)_4(H_2O)_{20} \cdot x$S (TMOP-1, where S represents non-assignable solvent molecules) were collected and washed with a little EtOH (yield, ~15 mg). The crystals of TMOP-1 slowly lose transparency when solvent molecules evacuated in air for a longer time. This compound is insoluble in DMA, DMSO, MeOH, THF, acetone, and H_2O.

6.2.4 Single Crystal Crystallography of PCN-530 and TMOP-1

The crystals of both PCN-530 and TMOP-1 were taken from the mother solution directly, transferred into oil, and mounted onto a loop for single crystal X-ray data collection. Diffractions were measured on a Bruker Smart Apex diffractometer equipped with a Mo-Kα sealed-tube X-ray source (λ = 0.71073 Å, graphite monochromator) and a cooling device (110 K). The data frames were recorded using APEX2 and processed using *SAINT* within APEX2. The data were corrected for absorption and beam corrections based on the semi-empirical technique as implemented in *SADABS*. The structures were solved by direct methods using *SHELXS* and refined by full-matrix least-squares on F^2 using *SHELXL* in OLEX2.

PCN-530 was integrated and refined in the triclinic crystal system. *XPREP* showed an R(sym) of 0.000 as standard for the Bravais lattice, Triclinic P. There was no more probable reasonable symmetry shown. XPREP listed 2 possible space groups, $P\bar{1}$ and *P*1, for centrosymmetric CFOM 2.14 and noncentrosymmetric CFOM 8.48 respectively. Mean |E*E-1| of 0.986 also indicated a centrosymmetric space group and thus $P\bar{1}$ was chosen. We obtained an R value of 0.0493 and wR_2 of 0.1221 after using the SQUEEZE routine in PLATON for the solution in $P\bar{1}$.

For PCN-530, no disorder modeling or restraints (except for hydrogen) were necessary. Thermal parameters were reasonable for the framework.

The thymine MOP was integrated and refined in the triclinic crystal system. *XPREP* showed an R(sym) of 0.000 as standard for the Bravais lattice, Triclinic P. The next most probable symmetry was Monoclinic C or I, both of which had an R(sym) of

0.621 and were dismissed. XPREP listed 2 possible space groups, $P\bar{1}$ and $P1$, for centrosymmetric CFOM 3.21 and noncentrosymmetric CFOM 7.88 respectively. Mean |E*E-1| of 0.950 also indicated a centrosymmetric space group and thus $P\bar{1}$ was chosen. We obtained an R_1 of 0.0997 for and a wR_2 of 0.2557 after using the SQUEEZE routine in PLATON for the solution in $P\bar{1}$.

For the TMOP-1 refinement, AFIX and DFIX restraints were used on several of the disordered thymine moieties, and PART and SPLIT commands combined with partial occupancy were used to model disorder on these moieties. Several other thymine moieties required no restraints or disorder modeling, and appeared to be in more confined and hydrogen-bonded parts of the structure and thus have a more consistent position.

For both solutions, all non-hydrogen atoms were refined with anisotropic displacement parameters during the final cycles. Organic hydrogen atoms were located in calculated positions with isotropic displacement parameters set to $1.2 \times U_{eq}$ of the attached atoms. The solvent molecules were highly disordered, and attempts to locate and refine the solvent peaks were unsuccessful. Contributions to scattering due to these solvent molecules were removed using the *SQUEEZE* routine of *PLATON*; structures were then refined again using the data generated. The contents of the solvent region are not represented in the unit cell contents in the crystal data.

The detailed information about the solution and refinement of the single crystal structures of PCN-530 and TMOP-1 can be found in the supporting information of this manuscript. [98] The CIF files can be obtained free of charge from the Cambridge

Crystallographic Data Centre via www.ccdc.cam.ac.uk/data_request/cif (CCDC 962335 for PCN-530 and 962336 for TMOP)

6.3 Results and Discussion

6.3.1 Rational Design of nucleobase-incorporated MOMs

Despite these advantages associated with nucleobase-incorporated MOMs, only a limited number of nucleobase-incorporated MOFs [98, 167, 176, 251, 252, 257] were published to date, and no crystalline MOPs with nucleobase moieties have been reported yet. This limitation may have resulted from the lack of intrinsic symmetry of nucleobases and the difficulty of controlling their binding modes to metal ions. Highly symmetric units are typically more favored in MOF construction [43, 44] since they will significantly facilitate the packing of the repetitive units in the formation of crystalline materials. The incorporation of low-symmetry units, such as nucleobases, into MOFs is usually less favorable. Rosi and co-workers have published a few "bio-MOFs" constructed from highly symmetric zinc-adeninate Secondary Building Units (SBUs). [167, 176] The presence of this SBU has increased the framework symmetry and eliminated undesired coordination modes between adenine and metal ions. Apart from their approach, herein we introduce two different strategies to synthesize nucleobase-incorporated MOMs. First, despite the low-symmetry of nucleobase molecules, the introduction of a highly symmetric co-ligand may be an effective way to incorporate nucleobases into MOFs. Second, nucleobase-incorporated MOPs may be constructed by connecting the nucleobase molecules to a commonly seen moiety for MOP construction. The successful

implementation of these two strategies has yielded two MOMs, PCN-530 and TMOP-1. Both of them are novel MOM structures with nucleobase moiety.

6.3.2 Crystal Structure of PCN-530

Colorless, blocky single crystals of PCN-530, $Zn_3[Zn_2(\mu_2\text{-}H_2O)]_3(Ad)_6(TATB)_4(DMF)$, (Ad = adeninate, TATB = 4,4*'*,4*''*-*s*-triazine-2,4,6-triyl-tribenzoate) were obtained via a solvothermal reaction between zinc acetate, adenine and H_3TATB in *N, N'*-dimethylformamide (DMF) in the presence of water. A single-crystal X-ray diffraction (XRD) study reveals that PCN-530 crystallizes in the triclinic space group $P\bar{1}$. Due to multiple metal-binding modes of adenine, two distinctive SBUs, denoted as "SBU 1" and "SBU 2" hereinafter, were identified in the structure (Figure VI-1 (a) and (b)). SBU 1 consists of a four-coordinate Zn(II) that links two adeninates via the 7-N atom on the imidazolate moiety and two carboxylates. SBU 2 consists of a $Zn_2(\mu_2\text{-}H_2O)$ unit, where two adeninates bridge the dizinc center via 3-N and 9-N atoms at the two equatorial positions, while two carboxylates coordinate to the dizinc center at the two axial positions. It should be noted that in each adeninate, all the imino 7-N donors coordinate to SBU 1, and all the 3-N and 9-N atoms coordinate to SBU 2, leaving 1-N and the exocyclic 6-N atoms uncoordinated (Figure VI-1(c)). SBU 1 and SBU 2 were connected by adeninate in a 1:1 ratio, forming one-dimensional zinc-adeninate chains (Figure VI-1(d)).

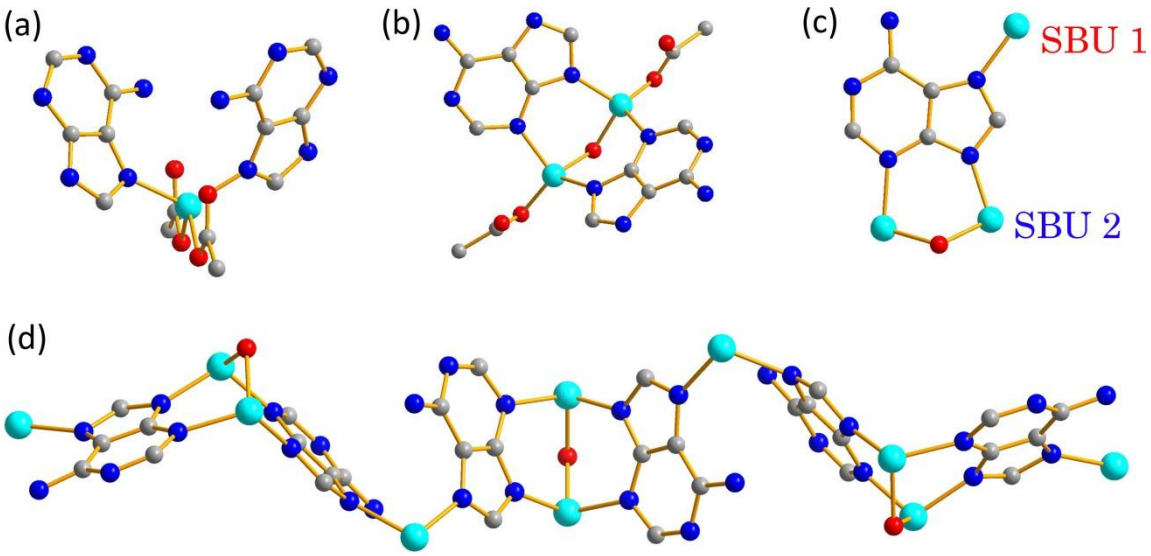

Figure VI-1. The graphic representation of (a) SBU 1, (b) SBU 2, (c) adeninate and its coordination modes, and (d) the one-dimensional zinc-adeninate chain in the framework. Color scheme: gray, C; red, O; blue, N; and cyan, Zn. H atoms were omitted for clarity.

Similar to many other MOFs constructed from the **TATB** ligand, the *s*-triazine ring located in the center allows it to adopt a nearly planar conformation (Figure VI-2(a)). [254, 258, 259] This conformation greatly facilitates the delocalization of the π electrons within a TATB ligand and strengthens the π…π interaction between two adjacent ones. [259] In an *s*-triazine core, the N and C atoms are partially negatively and positively charged, respectively. The adjacent TATB ligands stagger themselves so the N atoms in one ligand are aligned with the C atoms of the other to maximize the π…π interaction. [254, 260] The distance between adjacent s-triazine rings is 3.53 Å (Figure VI-2(a)). The one-dimensional zinc-adeninate chain is connected by TATB ligands, generating a 3,4,4-connected framework denoted as $(6^2 \cdot 8^4)_3(6^3)_2$. The solvent accessible volume of PCN-

530 is 47.80% calculated by using the PLATON routine [125], indicating its porous nature. Indeed, PCN-530 possesses open channels of 7.4 ×11.9 Å along *a* axis (Figure VI-2(b)).

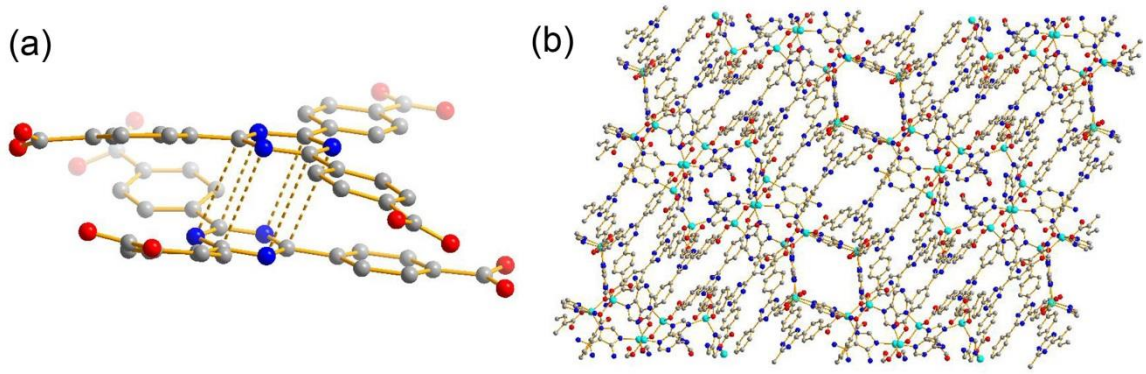

Figure VI-2. (a) The graphic representation of the π…π stacking between two TATB ligands. The dashed lines indicate the interaction between two adjacent s-triazine rings. (b) Packing diagram of PCN-530 along *a* axis.

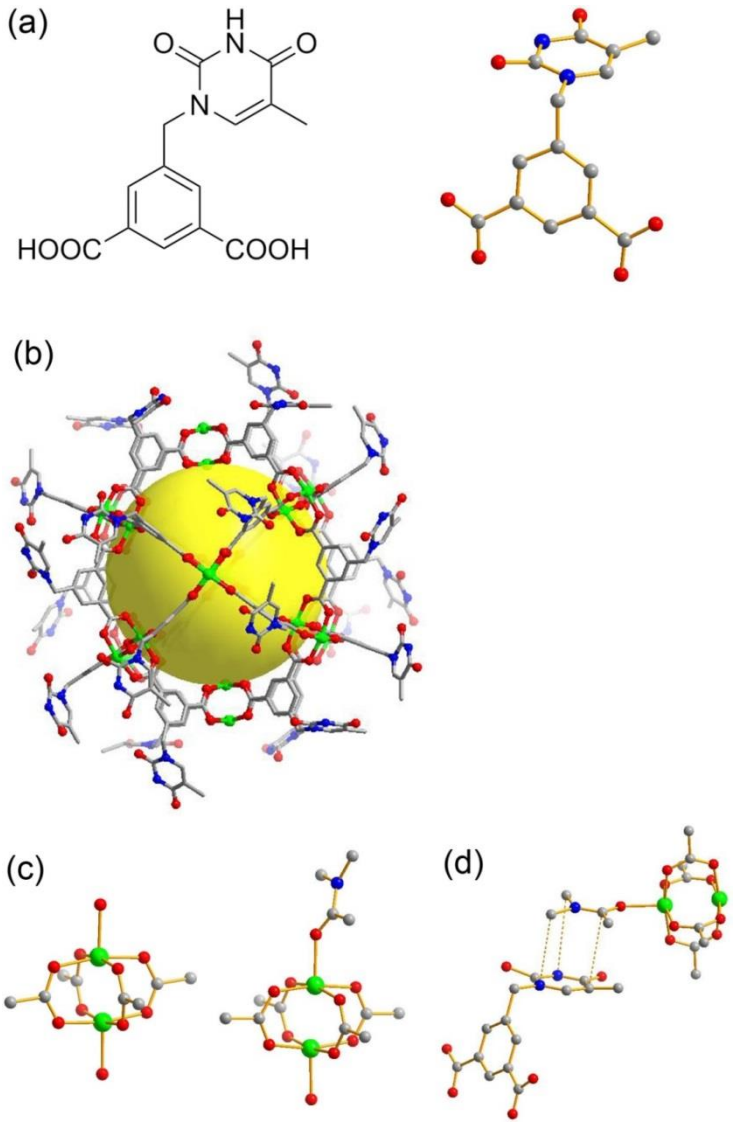

Figure VI-3. The crystal structure of TMOP-1. (a) The thymine-incorporated ligand with isophthalate moiety for MOP construction. (b) The crystal structure of TMOP-1. (c) Two types of dicopper paddlewheel SBUs, the one on the left is coordinated to two H_2O molecules, while the one on the right is coordinated to one H_2O and one DMA molecule. (d) The π…π interaction between the coordinating DMA and a neighboring thymine facilitates the packing of the MOP.

6.3.3 Crystal Structure of TMOP-1

Teal, blocky crystals of TMOP-1, $Cu_{24}(MDPI)_{24}(DMA)_4(H_2O)_{20}$ (MDPI = 5-((5-methyl-2,4-dioxo-3,4-dihydropyrimidin-1(2H)-yl)methyl)isophthate, See Figure VI-3(a)), were obtained by a direct reaction between copper acetate and H_2**MDPI** at room temperature. Isophthalates are one of the important categories of MOP constructional units, [95-97] and many highly porous MOFs based on cuboctahedral cavities were also constructed from ligands with isophthalate moieties. [105, 110] A single-crystal XRD study shows that TMOP-1 crystallizes in the triclinic space group $P\bar{1}$. Unlike the idealized O_h symmetry encountered in many other isophthalate-based MOPs, [95] due to various orientations and disorders of the terminal thymine moieties, TMOP-1 possesses C_i symmetry with an inversion center located at the geometric center (Figure VI-3(b)). Two types of dicopper paddlewheel SBUs were found in this structure (Figure VI-3(c)), which resulted from different coordinating solvents (DMA and H_2O) at the axial positions of the dicopper paddlewheels on the exterior surface of the cage. It is probable that a coordinated DMA molecule may have facilitated the packing of TMOP-1 by forming a π…π interaction pair with a thymine moiety from an adjacent MOP (Figure VI-3(d)). The distance between the coordinated DMA and the neighboring thymine is 3.65 Å. In addition, the hydrogen bonding between two adjacent thymine moieties from two different MOPs may have facilitated the packing of TMOP-1 as well. It should be noted that DNA-coated molecular cages were reported by Fujita and co-workers, providing neither their single crystal structures nor the evidence of their crystallinity, presumably due to the complexity of their system. [261] However, MOPs are usually

regarded as crystalline materials with well-defined structures. [95-97] To the best of our knowledge, this is the first reported case of nucleobase-incorporated MOP that has been structurally characterized by single crystal XRD studies.

6.3.4 Other Representative Examples of MOFs with Biomimetic Features

In addition to nucleobases, many other biological/biomimetic units have been successfully incorporated into MOFs. [187] Yaghi and Stoddart groups have reported a series of CD-MOFs (CD-MOF represents "γ-Cyclodextrin-incorporated Metal-Organic Framework"), which are constructed from oligosaccharides as organic linkers. [262, 263] They are the first example of a metal-saccharide MOFs with permanent porosities. MOFs with biomimetic activities can be rationally designed by incorporating any structures that contain or mimic the enzymatic prosthetic groups into MOF struts or cavities. This has inspired the study of "biomimetic chemistry" [264] or "artificial enzymes" [265] and motivated researchers to imitate the enzymatic activities *in vitro*. So far, MOFs with biomimetic catalytic activities are successfully constructed by incorporating metalloporphyrins, [266] iron-sulfur clusters, [267] and even the entire enzymes [29, 30, 268] into MOFs.

6.4 Summary

In conclusion, we have synthesized and characterized two novel nucleobase-incorporated MOMs, PCN-530 and TMOP-1, based on rational design. PCN-530 was prepared by introducing a highly symmetric linker as the co-ligand during the formation

of MOFs, to compensate the low-symmetry nature of adenine. It possesses two distinctive rarely seen SBUs. TMOP-1 was prepared by incorporating thymine into the isophthalate moiety, which is commonly used for MOP syntheses. It is the first crystallographically confirmed example of a nucleobase-incorporated MOP. It should be noted that in both PCN-530 and TMOP-1, the nucleobase hydrogen bonding sites are open, which makes it possible to incorporate DNA base pair interaction into the MOMs. This work has shown some potential in making DNA-coated biosensors and it is currently in progress in our lab. More importantly, the successful syntheses of PCN-530 and TMOP-1 also provide general guidance for the future design of nucleobase-incorporated MOMs.

In general, the study of biomimetic MOMs is still in its initial phase and there are several key research challenges to be addressed. First, beside the rich functionalities in MOMs, construction of materials with enhanced chemical stability that will stand up to physiological conditions for biomimetic activities still remains problematic. A few representative cases have been successfully reported, but examples of MOMs that exhibit high stability, large porosity and reduced cost are still relatively rare. Nevertheless, this concern has partially been addressed by the use of abundant, high valence metal ions or clusters. Second, development of new synthetic techniques appears to be necessary in order to synthesize and crystallize biocompatible MOMs, where the utilization of biological molecules with low symmetry and limited solubility in common solvents are often unavoidable. Finally, further exploration of MOMs with ultralarge cavities, preferably with a particular shape, polarity, or with protein-anchoring functional

groups, is necessary for study of enzyme immobilization in MOMs. Thanks to the extraordinarily large variety of MOM structures and the exceedingly rapid growth of the MOM field, we believe these challenges can be solved in the near future.

CHAPTER VII

CONCLUSIONS

This dissertation has described the rational design of various advanced porous materials with expected structures, topologies, porosities, and properties. The employment of symmetry-guided design strategy has led to the discovery of a great variety of different APMs. By unravelling their structure-property relationships and utilizing the principles of group theory and topological chemistry, a great variety of MOFs have been successfully constructed and characterized. Several representative examples of rational design of PPNs and MOPs are also presented.

Tetrahedral building units are particularly attractive for the construction of APMs because of their high symmetry and fully extended nature. Chapter II has illustrated that the incorporation of a synthetically-accessible tetrahedral ligand into MOFs has generated a series of novel MOFs. All these MOFs were structurally and topologically characterized, where seven of them possess a new structure, one of them possesses a novel topology, and two of them show properties potentially useful for gas storage applications. In particular, PCN-514 is a rare example of a MOF with metal complexes trapped inside its framework cavities. PCN-515 contains three distinctive rarely-seen SBUs in the same framework, which makes it an unprecedented 4,4,4,4,4,5,7-connected network.

Further elongation of tetrahedral linkers has led to the discovery of two highly porous MOFs, PCN-521 and PCN-523. Chapter III has presented a successful

implementation of the symmetry-guided design strategy. This strategy is based on a close examination of some simple mineral structures. Fluorite topology is especially intriguing for the construction of highly porous MOFs. By augmenting its 4-connected nodes with a rigid tetrahedral ligand, a series of MOFs with the same topology but considerably enlarged interstitial octahedral cavities were generated. Among these MOFs, PCN-521 possesses the largest cavity size, BET surface area, and solvent accessible volume among all the MOF made from tetrahedral ligands. It is the first existing example of a zirconium MOF made from tetrahedral linkers.

Further exploration of this symmetry-guided design strategy using porous organic polymers has led to the discovery of PPN-101. The utilization of a tetrahedral monomer and a linear monomer has generated a porous polymer framework with the desired diamondoid topology. Incorporation of Lewis bases into its framework has significantly improved its CO_2 uptake capacity and CO_2/N_2 selectivity. The low production expense, considerable porosity, and large CO_2/N_2 selectivity have made PPN-101 a promising material for industrial CO_2 sequestration.

Early discoveries of mixed-ligand MOFs have been highly serendipitous, and their rational design has been an exceedingly challenging problem. Nevertheless, the symmetry-guided design strategy has shed light on the rational design of mixed-ligand MOFs. Study of the relationship between Bravais lattice symmetry, in particular, the symmetry elements predominantly found in ordered repeating MOF lattices, and the point group symmetry of a MOF's fundamental building blocks, has led to the discovery of a series of highly porous mixed-ligand MOFs, all of which are novel structures with

their solvent accessible volumes up to 71.60% and BET surface areas up to 3090 $m^2 \cdot g^{-1}$. They are the first reported examples of mixed-ligand MOF made from tetrahedral ligands. In particular, PCN-501 possesses a volumetric surface area of 2151 $m^2 \cdot cm^{-3}$, which is the larger value than any other MOFs made from tetrahedral linkers.

In addition, two nucleobase-incorporated MOMs were also reported. Chapter VI has illustrated their rational design, synthesis, structural characterization, and potential applications. This work also provides general guidance for the future design of MOMs with biomimetic features.

In conclusion, symmetry has played a central role in the rational design of these APMs. Materials with desirable properties can be rationally designed by judicious selection of their basic building blocks with complementary symmetries. This work not only provides a systematic way of designing APMs with desired properties, but also shed light on the bottom-up design strategy of many other complicated multicomponent systems, including co-crystals, co-polymers, and composite materials.

REFERENCES

1. Davis, M. E., *Nature* **2002,** *417*, 813-821.
2. Perry IV, J. J.; Perman, J. A.; Zaworotko, M. J., *Chem. Soc. Rev.* **2009,** *38*, 1400-1417.
3. Carne, A.; Carbonell, C.; Imaz, I.; Maspoch, D., *Chem. Soc. Rev.* **2011,** *40*, 291-305.
4. Trewin, A.; Cooper, A. I., *Angew. Chem. Int. Ed.* **2010,** *49*, 1533-1535.
5. Zhang, Y.; Riduan, S. N., *Chem. Soc. Rev.* **2012,** *41*, 2083-2094.
6. Lee, J.; Kim, J.; Hyeon, T., *Adv. Mater.* **2006,** *18*, 2073-2094.
7. Zhao, D.; Feng, J.; Huo, Q.; Melosh, N.; Fredrickson, G. H.; Chmelka, B. F.; Stucky, G. D., *Science* **1998,** *279*, 548-552.
8. Attard, G. S.; Glyde, J. C.; Goltner, C. G., *Nature* **1995,** *378*, 366-368.
9. Jacobsen, C. J. H.; Madsen, C.; Houzvicka, J.; Schmidt, I.; Carlsson, A., *J. Am. Chem. Soc.* **2000,** *122*, 7116-7117.
10. Wang, N.; Tang, Z. K.; Li, G. D.; Chen, J. S., *Nature* **2000,** *408*, 50-51.
11. Zhou, H.-C.; Long, J. R.; Yaghi, O. M., *Chem. Rev.* **2012,** *112*, 673-674.
12. Long, J. R.; Yaghi, O. M., *Chem. Soc. Rev.* **2009,** *38*, 1213-1214.
13. Batten, S. R.; Champness, N. R.; Chen, X.-M.; Garcia-Martinez, J.; Kitagawa, S.; Öhrström, L.; Michael, O. K.; Suh, M. P.; Reedijk, J., *Pure Appl. Chem.* **2013,** *85*, 1715-1724.
14. Li, H.; Eddaoudi, M.; O'Keeffe, M.; Yaghi, O. M., *Nature* **1999,** *402*, 276-279.

15. Chui, S. S.-Y.; Lo, S. M.-F.; Charmant, J. P. H.; Orpen, A. G.; Williams, I. D., *Science* **1999,** *283*, 1148-1150.

16. Sculley, J.; Yuan, D.; Zhou, H.-C., *Energy Environ. Sci.* **2011,** *4*, 2721-2735.

17. Suh, M. P.; Park, H. J.; Prasad, T. K.; Lim, D.-W., *Chem. Rev.* **2011,** *112*, 782-835.

18. Makal, T. A.; Li, J.-R.; Lu, W.; Zhou, H.-C., *Chem. Soc. Rev.* **2012,** *41*, 7761-7779.

19. Bloch, E. D.; Queen, W. L.; Krishna, R.; Zadrozny, J. M.; Brown, C. M.; Long, J. R., *Science* **2012,** *335*, 1606-1610.

20. Li, J.-R.; Kuppler, R. J.; Zhou, H.-C., *Chem. Soc. Rev.* **2009,** *38*, 1477-1504.

21. Li, J.-R.; Sculley, J.; Zhou, H.-C., *Chem. Rev.* **2011,** *112*, 869-932.

22. McDonald, T. M.; Lee, W. R.; Mason, J. A.; Wiers, B. M.; Hong, C. S.; Long, J. R., *J. Am. Chem. Soc.* **2012,** *134*, 7056-7065.

23. Sumida, K.; Rogow, D. L.; Mason, J. A.; McDonald, T. M.; Bloch, E. D.; Herm, Z. R.; Bae, T.-H.; Long, J. R., *Chem. Rev.* **2011,** *112*, 724-781.

24. Li, J.-R.; Ma, Y.; McCarthy, M. C.; Sculley, J.; Yu, J.; Jeong, H.-K.; Balbuena, P. B.; Zhou, H.-C., *Coord. Chem. Rev.* **2011,** *255*, 1791-1823.

25. Yee, K.-K.; Reimer, N.; Liu, J.; Cheng, S.-Y.; Yiu, S.-M.; Weber, J.; Stock, N.; Xu, Z., *J. Am. Chem. Soc.* **2013,** *135*, 7795-7798.

26. Ke, F.; Qiu, L.-G.; Yuan, Y.-P.; Peng, F.-M.; Jiang, X.; Xie, A.-J.; Shen, Y.-H.; Zhu, J.-F., *J. Hazard. Mater.* **2011,** *196*, 36-43.

27. Ma, L.; Abney, C.; Lin, W., *Chem. Soc. Rev.* **2009,** *38*, 1248-1256.

28. Yoon, M.; Srirambalaji, R.; Kim, K., *Chem. Rev.* **2011,** *112*, 1196-1231.

29. Lykourinou, V.; Chen, Y.; Wang, X.-S.; Meng, L.; Hoang, T.; Ming, L.-J.; Musselman, R. L.; Ma, S., *J. Am. Chem. Soc.* **2011,** *133*, 10382-10385.

30. Chen, Y.; Lykourinou, V.; Vetromile, C.; Hoang, T.; Ming, L.-J.; Larsen, R. W.; Ma, S., *J. Am. Chem. Soc.* **2012,** *134*, 13188-13191.

31. Allendorf, M. D.; Bauer, C. A.; Bhakta, R. K.; Houk, R. J. T., *Chem. Soc. Rev.* **2009,** *38*, 1330-1352.

32. Cui, Y.; Yue, Y.; Qian, G.; Chen, B., *Chem. Rev.* **2011,** *112*, 1126-1162.

33. Wriedt, M.; Yakovenko, A. A.; Halder, G. J.; Prosvirin, A. V.; Dunbar, K. R.; Zhou, H.-C., *J. Am. Chem. Soc.* **2013,** *135*, 4040-4050.

34. Horcajada, P.; Chalati, T.; Serre, C.; Gillet, B.; Sebrie, C.; Baati, T.; Eubank, J. F.; Heurtaux, D.; Clayette, P.; Kreuz, C.; Chang, J.-S.; Hwang, Y. K.; Marsaud, V.; Bories, P.-N.; Cynober, L.; Gil, S.; Ferey, G.; Couvreur, P.; Gref, R., *Nat. Mater.* **2010,** *9*, 172-178.

35. Horcajada, P.; Gref, R.; Baati, T.; Allan, P. K.; Maurin, G.; Couvreur, P.; Férey, G.; Morris, R. E.; Serre, C., *Chem. Rev.* **2011,** *112*, 1232-1268.

36. Furukawa, H.; Cordova, K. E.; O'Keeffe, M.; Yaghi, O. M., *Science* **2013,** *341*, 1230444.

37. Fajula, F.; Galarneau, A.; Renzo, F. D., *Microporous Mesoporous Mater.* **2005,** *82*, 227-239.

38. Kuznicki, S. M.; Bell, V. A.; Nair, S.; Hillhouse, H. W.; Jacubinas, R. M.; Braunbarth, C. M.; Toby, B. H.; Tsapatsis, M., *Nature* **2001,** *412*, 720-724.

39. Chen, B.; Ma, S.; Zapata, F.; Fronczek, F. R.; Lobkovsky, E. B.; Zhou, H.-C., *Inorg. Chem.* **2007,** *46*, 1233-1236.

40. Farha, O. K.; Hupp, J. T., *Acc. Chem. Res.* **2010,** *43*, 1166-1175.

41. Eddaoudi, M.; Kim, J.; Rosi, N.; Vodak, D.; Wachter, J.; O'Keeffe, M.; Yaghi, O. M., *Science* **2002,** *295*, 469-472.

42. Yaghi, O. M.; O'Keeffe, M.; Ockwig, N. W.; Chae, H. K.; Eddaoudi, M.; Kim, J., *Nature* **2003,** *423*, 705-714.

43. Zhao, D.; Timmons, D. J.; Yuan, D.; Zhou, H.-C., *Acc. Chem. Res.* **2010,** *44*, 123-133.

44. Almeida Paz, F. A.; Klinowski, J.; Vilela, S. M. F.; Tome, J. P. C.; Cavaleiro, J. A. S.; Rocha, J., *Chem. Soc. Rev.* **2012,** *41*, 1088-1110.

45. Lu, W.; Wei, Z.; Gu, Z.-Y.; Liu, T.-F.; Park, J.; Park, J.; Tian, J.; Zhang, M.; Zhang, Q.; Gentle, T.; Bosch, M.; Zhou, H.-C., *Chem. Soc. Rev.* **2014,** *43*, 5561-5593.

46. Wang, Z.; Cohen, S. M., *Chem. Soc. Rev.* **2009,** *38*, 1315-1329.

47. Cohen, S. M., *Chem. Rev.* **2011,** *112*, 970-1000.

48. Zhang, M.; Chen, Y.-P.; Bosch, M.; Gentle, T.; Wang, K.; Feng, D.; Wang, Z. U.; Zhou, H.-C., *Angew. Chem. Int. Ed.* **2014,** *53*, 815-818.

49. Zhang, M.; Bosch, M.; Gentle, T.; Zhou, H.-C., *CrystEngComm* **2014,** *16*, 4069-4083.

50. Wang, X.-S.; Ma, S.; Forster, P. M.; Yuan, D.; Eckert, J.; López, J. J.; Murphy, B. J.; Parise, J. B.; Zhou, H.-C., *Angew. Chem. Int. Ed.* **2008,** *47*, 7263-7266.

51. Sun, D.; Ke, Y.; Mattox, T. M.; Ooro, B. A.; Zhou, H.-C., *Chem. Commun.* **2005**, 5447-5449.

52. Zhang, M.; Chen, Y.-P.; Zhou, H.-C., *CrystEngComm* **2013,** *15*, 9544-9552.

53. Morris, W.; Volosskiy, B.; Demir, S.; Gándara, F.; McGrier, P. L.; Furukawa, H.; Cascio, D.; Stoddart, J. F.; Yaghi, O. M., *Inorg. Chem.* **2012,** *51*, 6443-6445.

54. Ma, S.; Sun, D.; Ambrogio, M.; Fillinger, J. A.; Parkin, S.; Zhou, H.-C., *J. Am. Chem. Soc.* **2007,** *129*, 1858-1859.

55. Makal, T. A.; Yakovenko, A. A.; Zhou, H.-C., *J. Phys. Chem. Lett.* **2011,** *2*, 1682-1689.

56. Jiang, H.-L.; Makal, T. A.; Zhou, H.-C., *Coord. Chem. Rev.* **2013,** *257*, 2232-2249.

57. Farha, O. K.; Malliakas, C. D.; Kanatzidis, M. G.; Hupp, J. T., *J. Am. Chem. Soc.* **2009,** *132*, 950-952.

58. O'Keeffe, M.; Yaghi, O. M., *Chem. Rev.* **2011,** *112*, 675-702.

59. Blatov, V. A.; Carlucci, L.; Ciani, G.; Proserpio, D. M., *CrystEngComm* **2004,** *6*, 378-395.

60. Carlucci, L.; Ciani, G.; Proserpio, D. M., *Coord. Chem. Rev.* **2003,** *246*, 247-289.

61. Li, M.; Li, D.; O'Keeffe, M.; Yaghi, O. M., *Chem. Rev.* **2013,** *114*, 1343-1370.

62. Chen, B.; Eddaoudi, M.; Reineke, T. M.; Kampf, J. W.; O'Keeffe, M.; Yaghi, O. M., *J. Am. Chem. Soc.* **2000,** *122*, 11559-11560.

63. Kim, J.; Chen, B.; Reineke, T. M.; Li, H.; Eddaoudi, M.; Moler, D. B.; O'Keeffe, M.; Yaghi, O. M., *J. Am. Chem. Soc.* **2001,** *123*, 8239-8247.

64. Ma, L.; Jin, A.; Xie, Z.; Lin, W., *Angew. Chem. Int. Ed.* **2009,** *48*, 9905-9908.

65. Wen, L.; Cheng, P.; Lin, W., *Chem. Commun.* **2012,** *48*, 2846-2848.

66. Wen, L.; Cheng, P.; Lin, W., *Chem. Sci.* **2012,** *3*, 2288-2292.

67. Liu, D.; Wu, H.; Wang, S.; Xie, Z.; Li, J.; Lin, W., *Chem. Sci.* **2012,** *3*, 3032-3037.

68. Dincă, M.; Dailly, A.; Long, J. R., *Chem. Eur. J.* **2008,** *14*, 10280-10285.

69. Tan, C.; Yang, S.; Champness, N. R.; Lin, X.; Blake, A. J.; Lewis, W.; Schroder, M., *Chem. Commun.* **2011,** *47*, 4487-4489.

70. Chun, H.; Kim, D.; Dybtsev, D. N.; Kim, K., *Angew. Chem. Int. Ed.* **2004,** *43*, 971-974.

71. Cheon, Y. E.; Suh, M. P., *Chem. Commun.* **2009,** *0*, 2296-2298.

72. Taylor, J. M.; Mahmoudkhani, A. H.; Shimizu, G. K. H., *Angew. Chem. Int. Ed.* **2007,** *46*, 795-798.

73. Davies, R. P.; Less, R.; Lickiss, P. D.; Robertson, K.; White, A. J. P., *Cryst. Growth Des.* **2010,** *10*, 4571-4581.

74. Davies, R. P.; Less, R. J.; Lickiss, P. D.; Robertson, K.; White, A. J. P., *Inorg. Chem.* **2008,** *47*, 9958-9964.

75. Davies, R. P.; Lickiss, P. D.; Robertson, K.; White, A. J. P., *Aust. J. Chem.* **2011,** *64*, 1239-1246.

76. Timokhin, I.; Baguna Torres, J.; White, A. J. P.; Lickiss, P. D.; Pettinari, C.; Davies, R. P., *Dalton Trans.* **2013,** *42*, 13806-13808.

77. Lambert, J. B.; Liu, Z.; Liu, C., *Organometallics* **2008,** *27*, 1464-1469.

78. Liu, Z.; Stern, C. L.; Lambert, J. B., *Organometallics* **2008,** *28*, 84-93.

79. Senchyk, G. A.; Lysenko, A. B.; Boldog, I.; Rusanov, E. B.; Chernega, A. N.; Krautscheid, H.; Domasevitch, K. V., *Dalton Trans.* **2012,** *41*, 8675-8689.

80. Xue, Y.-S.; Jin, F.-Y.; Zhou, L.; Liu, M.-P.; Xu, Y.; Du, H.-B.; Fang, M.; You, X.-Z., *Cryst. Growth Des.* **2012,** *12*, 6158-6164.

81. Li, Y.; Xue, M.; Guo, L.; Huang, L.; Chen, S.; Qiu, S., *Inorg. Chem. Commun.* **2013,** *28*, 25-30.

82. Delgado-Friedrichs, O.; O'Keeffe, M.; Yaghi, O. M., *Acta Crystallogr. A* **2006,** *62*, 350-355.

83. Delgado-Friedrichs, O.; O'Keeffe, M.; Yaghi, O. M., *Phys. Chem. Chem. Phys.* **2007,** *9*, 1035-1043.

84. Delgado Friedrichs, O.; O'Keeffe, M.; Yaghi, O. M., *Solid State Sci.* **2003,** *5*, 73-78.

85. Dincă, M.; Dailly, A.; Liu, Y.; Brown, C. M.; Neumann, D. A.; Long, J. R., *J. Am. Chem. Soc.* **2006,** *128*, 16876-16883.

86. Taylor, S. R., *Geochim. Cosmochim. Ac* **1964,** *28*, 1273-1285.

87. Cavka, J. H.; Jakobsen, S.; Olsbye, U.; Guillou, N.; Lamberti, C.; Bordiga, S.; Lillerud, K. P., *J. Am. Chem. Soc.* **2008,** *130*, 13850-13851.

88. O'Keeffe, M.; Peskov, M. A.; Ramsden, S. J.; Yaghi, O. M., *Acc. Chem. Res.* **2008,** *41*, 1782-1789.

89. Hao, H.-Q.; Wang, J.; Liu, W.-T.; Tong, M.-L., *CrystEngComm* **2008,** *10*, 1454-1459.

90. Liu, D.; Xie, Z.; Ma, L.; Lin, W., *Inorg. Chem.* **2010,** *49*, 9107-9109.

91. Murphy, M. J.; D'Alessandro, D. M.; Kepert, C. J., *Dalton Trans.* **2013,** *42*, 13308-13310.

92. Yuan, A.-H.; Lu, R.-Q.; Zhou, H.; Chen, Y.-Y.; Li, Y.-Z., *CrystEngComm* **2010,** *12*, 1382-1384.

93. Xue, M.; Zhu, G.; Li, Y.; Zhao, X.; Jin, Z.; Kang, E.; Qiu, S., *Cryst. Growth Des.* **2008,** *8*, 2478-2483.

94. Zhang, Q.-F.; Luo, J.-H.; Yuan, A.-H., *Z. Anorg. Allg. Chem.* **2013,** *639*, 1804-1807.

95. Eddaoudi, M.; Kim, J.; Wachter, J. B.; Chae, H. K.; O'Keeffe, M.; Yaghi, O. M., *J. Am. Chem. Soc.* **2001,** *123*, 4368-4369.

96. Li, J.-R.; Yakovenko, A. A.; Lu, W.; Timmons, D. J.; Zhuang, W.; Yuan, D.; Zhou, H.-C., *J. Am. Chem. Soc.* **2010,** *132*, 17599-17610.

97. Li, J.-R.; Zhou, H.-C., *Nat. Chem.* **2010,** *2*, 893-898.

98. Zhang, M.; Lu, W.; Li, J.-R.; Bosch, M.; Chen, Y.-P.; Liu, T.-F.; Liu, Y.; Zhou, H.-C., *Inorg. Chem. Front.* **2014,** *1*, 159-162.

99. Caulder, D. L.; Raymond, K. N., *Acc. Chem. Res.* **1999,** *32*, 975-982.

100. Dinolfo, P. H.; Hupp, J. T., *Chem. Mater.* **2001,** *13*, 3113-3125.

101. Nouar, F.; Eubank, J. F.; Bousquet, T.; Wojtas, L.; Zaworotko, M. J.; Eddaoudi, M., *J. Am. Chem. Soc.* **2008,** *130*, 1833-1835.

102. Shimizu, G. K. H., *Nat. Chem.* **2010,** *2*, 909-911.

103. Li, J.-R.; Yu, J.; Lu, W.; Sun, L.-B.; Sculley, J.; Balbuena, P. B.; Zhou, H.-C., *Nat. Commun.* **2013,** *4*, 1538.

104. Zhao, D.; Yuan, D.; Sun, D.; Zhou, H.-C., *J. Am. Chem. Soc.* **2009,** *131*, 9186-9188.

105. Yuan, D.; Zhao, D.; Sun, D.; Zhou, H.-C., *Angew. Chem. Int. Ed.* **2010,** *49*, 5357-5361.

106. Yan, Y.; Lin, X.; Yang, S.; Blake, A. J.; Dailly, A.; Champness, N. R.; Hubberstey, P.; Schroder, M., *Chem. Commun.* **2009**, 1025-1027.

107. Yan, Y.; Telepeni, I.; Yang, S.; Lin, X.; Kockelmann, W.; Dailly, A.; Blake, A. J.; Lewis, W.; Walker, G. S.; Allan, D. R.; Barnett, S. A.; Champness, N. R.; Schröder, M., *J. Am. Chem. Soc.* **2010,** *132*, 4092-4094.

108. Yan, Y.; Yang, S.; Blake, A. J.; Lewis, W.; Poirier, E.; Barnett, S. A.; Champness, N. R.; Schroder, M., *Chem. Commun.* **2011,** *47*, 9995-9997.

109. Farha, O. K.; Özgür Yazaydın, A.; Eryazici, I.; Malliakas, C. D.; Hauser, B. G.; Kanatzidis, M. G.; Nguyen, S. T.; Snurr, R. Q.; Hupp, J. T., *Nat. Chem.* **2010,** *2*, 944-948.

110. Farha, O. K.; Eryazici, I.; Jeong, N. C.; Hauser, B. G.; Wilmer, C. E.; Sarjeant, A. A.; Snurr, R. Q.; Nguyen, S. T.; Yazaydın, A. Ö.; Hupp, J. T., *J. Am. Chem. Soc.* **2012,** *134*, 15016-15021.

111. Lu, W.; Yuan, D.; Zhao, D.; Schilling, C. I.; Plietzsch, O.; Muller, T.; Bräse, S.; Guenther, J.; Blümel, J.; Krishna, R.; Li, Z.; Zhou, H.-C., *Chem. Mater.* **2010,** *22*, 5964-5972.

112. Ben, T.; Ren, H.; Ma, S.; Cao, D.; Lan, J.; Jing, X.; Wang, W.; Xu, J.; Deng, F.; Simmons, J. M.; Qiu, S.; Zhu, G., *Angew. Chem. Int. Ed.* **2009,** *48*, 9457-9460.

113. Yuan, D.; Lu, W.; Zhao, D.; Zhou, H.-C., *Adv. Mater.* **2011,** *23*, 3723-3725.

114. Furukawa, H.; Yaghi, O. M., *J. Am. Chem. Soc.* **2009,** *131*, 8875-8883.

115. Lu, W.; Sculley, J. P.; Yuan, D.; Krishna, R.; Wei, Z.; Zhou, H.-C., *Angew. Chem. Int. Ed.* **2012,** *51*, 7480-7484.

116. Babarao, R.; Jiang, J., *Energy Environ. Sci.* **2008,** *1*, 139-143.

117. Zhang, M.; Perry, Z.; Park, J.; Zhou, H.-C., *Polymer* **2014,** *55*, 335-339.

118. Shultz, A. M.; Farha, O. K.; Hupp, J. T.; Nguyen, S. T., *Chem. Sci.* **2011,** *2*, 686-689.

119. Wang, X.-S.; Chrzanowski, M.; Yuan, D.; Sweeting, B. S.; Ma, S., *Chem. Mater.* **2014,** *26*, 1639-1644.

120. Kaur, P.; Hupp, J. T.; Nguyen, S. T., *ACS Catalysis* **2011,** *1*, 819-835.

121. Côté, A. P.; Benin, A. I.; Ockwig, N. W.; O'Keeffe, M.; Matzger, A. J.; Yaghi, O. M., *Science* **2005,** *310*, 1166-1170.

122. Beaudoin, D.; Maris, T.; Wuest, J. D., *Nat. Chem.* **2013,** *5*, 830-834.

123. Lambert, J. B.; Zhao, Y.; Stern, C. L., *J. Phys. Org. Chem.* **1997,** *10*, 229-232.

124. Lu, W.; Yuan, D.; Makal, T. A.; Wei, Z.; Li, J.-R.; Zhou, H.-C., *Dalton Trans.* **2013,** *42*, 1708-1714.

125. Spek, A., *J. Appl. Crystallogr.* **2003,** *36*, 7-13.

126. Sun, D.; Ke, Y.; Mattox, T. M.; Parkin, S.; Zhou, H.-C., *Inorg. Chem.* **2006,** *45*, 7566-7568.

127. Wei, Z.; Lu, W.; Jiang, H.-L.; Zhou, H.-C., *Inorg. Chem.* **2013,** *52*, 1164-1166.

128. Langmuir, I., *J. Am. Chem. Soc.* **1916,** *38*, 2221-2295.

129. Brunauer, S.; Emmett, P. H.; Teller, E., *J. Am. Chem. Soc.* **1938,** *60*, 309-319.

130. Furukawa, H.; Ko, N.; Go, Y. B.; Aratani, N.; Choi, S. B.; Choi, E.; Yazaydin, A. Ö.; Snurr, R. Q.; O'Keeffe, M.; Kim, J.; Yaghi, O. M., *Science* **2010,** *329*, 424-428.

131. Koh, K.; Wong-Foy, A. G.; Matzger, A. J., *J. Am. Chem. Soc.* **2009,** *131*, 4184-4185.

132. Bloch, E. D.; Murray, L. J.; Queen, W. L.; Chavan, S.; Maximoff, S. N.; Bigi, J. P.; Krishna, R.; Peterson, V. K.; Grandjean, F.; Long, G. J.; Smit, B.; Bordiga, S.; Brown, C. M.; Long, J. R., *J. Am. Chem. Soc.* **2011,** *133*, 14814-14822.

133. Wriedt, M.; Sculley, J. P.; Yakovenko, A. A.; Ma, Y.; Halder, G. J.; Balbuena, P. B.; Zhou, H.-C., *Angew. Chem. Int. Ed.* **2012,** *51*, 9804-9808.

134. Park, J.; Yuan, D.; Pham, K. T.; Li, J.-R.; Yakovenko, A.; Zhou, H.-C., *J. Am. Chem. Soc.* **2011,** *134*, 99-102.

135. APEX2 v2012.2.0 and SAINT v7.68A data collection and data processing programs, respectively. Bruker Analytical X-ray Instruments, Inc., Madison, WI; SADABS v2008/1 semi-empirical absorption and beam correction program. G.M. Sheldrick, University of Göttingen, Germany.

136. G. M. Sheldrick, SHELXTL, Version 6.14, Structure Determination Software Suite, Bruker AXS, Madison, WI, **2003**.

137. Gotthardt, J. M.; White, K. F.; Abrahams, B. F.; Ritchie, C.; Boskovic, C., *Cryst. Growth Des.* **2012,** *12*, 4425-4430.

138. Zhuang, W.; Yuan, D.; Liu, D.; Zhong, C.; Li, J.-R.; Zhou, H.-C., *Chem. Mater.* **2011,** *24*, 18-25.

139. Zhuang, W.; Yuan, D.; Li, J.-R.; Luo, Z.; Zhou, H.-C.; Bashir, S.; Liu, J., *Adv. Healthcare Mater.* **2012,** *1*, 225-238.

140. Chevreau, H.; Devic, T.; Salles, F.; Maurin, G.; Stock, N.; Serre, C., *Angew. Chem. Int. Ed.* **2013,** *52*, 5056-5060.

141. Feng, D.; Gu, Z.-Y.; Li, J.-R.; Jiang, H.-L.; Wei, Z.; Zhou, H.-C., *Angew. Chem. Int. Ed.* **2012,** *51*, 10307-10310.

142. Schaate, A.; Roy, P.; Godt, A.; Lippke, J.; Waltz, F.; Wiebcke, M.; Behrens, P., *Chem. Eur. J.* **2011,** *17*, 6643-6651.

143. Jiang, H.-L.; Feng, D.; Liu, T.-F.; Li, J.-R.; Zhou, H.-C., *J. Am. Chem. Soc.* **2012,** *134*, 14690-14693.

144. Feng, D.; Chung, W.-C.; Wei, Z.; Gu, Z.-Y.; Jiang, H.-L.; Chen, Y.-P.; Darensbourg, D. J.; Zhou, H.-C., *J. Am. Chem. Soc.* **2013,** *135*, 17105-17110.

145. Feng, D.; Jiang, H.-L.; Chen, Y.-P.; Gu, Z.-Y.; Wei, Z.; Zhou, H.-C., *Inorg. Chem.* **2013,** *52*, 12661-12667.

146. Wu, H.; Chua, Y. S.; Krungleviciute, V.; Tyagi, M.; Chen, P.; Yildirim, T.; Zhou, W., *J. Am. Chem. Soc.* **2013,** *135*, 10525-10532.

147. Vermoortele, F.; Bueken, B.; Le Bars, G.; Van de Voorde, B.; Vandichel, M.; Houthoofd, K.; Vimont, A.; Daturi, M.; Waroquier, M.; Van Speybroeck, V.; Kirschhock, C.; De Vos, D. E., *J. Am. Chem. Soc.* **2013,** *135*, 11465-11468.

148. Hu, J.-S.; Shang, Y.-J.; Yao, X.-q.; Qin, L.; Li, Y.-Z.; Guo, Z.-J.; Zheng, H.-G.; Xue, Z.-L., *Cryst. Growth Des.* **2010,** *10*, 2676-2684.

149. Timokhin, I.; White, A. J. P.; Lickiss, P. D.; Pettinari, C.; Davies, R. P., *CrystEngComm* **2014,** *16*, 8094-8097.

150. Pearson, P. N.; Palmer, M. R., *Nature* **2000,** *406*, 695-699.

151. Lu, W.; Yuan, D.; Sculley, J.; Zhao, D.; Krishna, R.; Zhou, H.-C., *J. Am. Chem. Soc.* **2011,** *133*, 18126-18129.

152. Pariya, C.; Marcos, Y. S.; Zhang, Y.; Fronczek, F. R.; Maverick, A. W., *Organometallics* **2008,** *27*, 4318-4324.

153. Rabbani, M. G.; El-Kaderi, H. M., *Chem. Mater.* **2011,** *23*, 1650-1653.

154. Sculley, J. P.; Verdegaal, W. M.; Lu, W.; Wriedt, M.; Zhou, H.-C., *Adv. Mater.* **2013,** *25*, 3957-3961.

155. Simmons, J. M.; Wu, H.; Zhou, W.; Yildirim, T., *Energy Environ. Sci.* **2011,** *4*, 2177-2185.

156. Kou, Y.; Xu, Y.; Guo, Z.; Jiang, D., *Angew. Chem. Int. Ed.* **2011,** *50*, 8753-8757.

157. Zhu, X.; Tian, C.; Mahurin, S. M.; Chai, S.-H.; Wang, C.; Brown, S.; Veith, G. M.; Luo, H.; Liu, H.; Dai, S., *J. Am. Chem. Soc.* **2012,** *134*, 10478-10484.

158. Ren, S.; Bojdys, M. J.; Dawson, R.; Laybourn, A.; Khimyak, Y. Z.; Adams, D. J.; Cooper, A. I., *Adv. Mater.* **2012,** *24*, 2357-2361.

159. Asensio, J. A.; Sanchez, E. M.; Gomez-Romero, P., *Chem. Soc. Rev.* **2010,** *39*, 3210-3239.

160. Fournier, J.-H.; Wang, X.; Wuest, J. D., *Can. J. Chem.* **2003,** *81*, 376-380.

161. Chen, L.; Kim, J.; Ishizuka, T.; Honsho, Y.; Saeki, A.; Seki, S.; Ihee, H.; Jiang, D., *J. Am. Chem. Soc.* **2009,** *131*, 7287-7292.

162. Rabbani, M. G.; Reich, T. E.; Kassab, R. M.; Jackson, K. T.; El-Kaderi, H. M., *Chem. Commun.* **2012,** *48*, 1141-1143.

163. Rabbani, M. G.; Sekizkardes, A. K.; El-Kadri, O. M.; Kaafarani, B. R.; El-Kaderi, H. M., *J. Mater. Chem.* **2012,** *22*, 25409-25417.

164. Rabbani, M. G.; El-Kaderi, H. M., *Chem. Mater.* **2012,** *24*, 1511-1517.

165. Koh, K.; Wong-Foy, A. G.; Matzger, A. J., *Angew. Chem. Int. Ed.* **2008,** *47*, 677-680.

166. Klein, N.; Senkovska, I.; Gedrich, K.; Stoeck, U.; Henschel, A.; Mueller, U.; Kaskel, S., *Angew. Chem. Int. Ed.* **2009,** *48*, 9954-9957.

167. An, J.; Farha, O. K.; Hupp, J. T.; Pohl, E.; Yeh, J. I.; Rosi, N. L., *Nat. Commun.* **2012,** *3*, 604.

168. Koh, K.; Wong-Foy, A. G.; Matzger, A. J., *J. Am. Chem. Soc.* **2010,** *132*, 15005-15010.

169. Furukawa, H.; Cordova, K. E.; O'Keeffe, M.; Yaghi, O. M., *Science* **2013,** *341*.

170. He, W.-W.; Li, S.-L.; Yang, G.-S.; Lan, Y.-Q.; Su, Z.-M.; Fu, Q., *Chem. Commun.* **2012,** *48*, 10001-10003.

171. Han, Z.-B.; Liang, Y.-F.; Zhou, M.; Zhang, Y.-R.; Li, L.; Tong, J., *CrystEngComm* **2012,** *14*, 6952-6956.

172. Grunker, R.; Bon, V.; Muller, P.; Stoeck, U.; Krause, S.; Mueller, U.; Senkovska, I.; Kaskel, S., *Chem. Commun.* **2014,** *50*, 3450-3452.

173. Fang, Q.-R.; Makal, T. A.; Young, M. D.; Zhou, H.-C., *Comment. Inorg. Chem.* **2010,** *31*, 165-195.

174. Stock, N.; Biswas, S., *Chem. Rev.* **2011,** *112*, 933-969.

175. Wang, H.; Yang, W.; Sun, Z.-M., *Chem. Asian J.* **2013,** *8*, 982-989.

176. An, J.; Geib, S. J.; Rosi, N. L., *J. Am. Chem. Soc.* **2009,** *131*, 8376-8377.

177. Banerjee, R.; Phan, A.; Wang, B.; Knobler, C.; Furukawa, H.; O'Keeffe, M.; Yaghi, O. M., *Science* **2008,** *319*, 939-943.

178. Sumida, K.; Horike, S.; Kaye, S. S.; Herm, Z. R.; Queen, W. L.; Brown, C. M.; Grandjean, F.; Long, G. J.; Dailly, A.; Long, J. R., *Chem. Sci.* **2010,** *1*, 184-191.

179. Volkringer, C.; Loiseau, T.; Guillou, N.; Férey, G. r.; Haouas, M.; Taulelle, F.; Elkaim, E.; Stock, N., *Inorg. Chem.* **2010,** *49*, 9852-9862.

180. Bond, A. D., *CrystEngComm* **2007,** *9*, 833-834.

181. Aitipamula, S.; Chow, P. S.; Tan, R. B. H., *CrystEngComm* **2014,** *16*, 3451-3465.

182. Hauser, B. G.; Farha, O. K.; Exley, J.; Hupp, J. T., *Chem. Mater.* **2012,** *25*, 12-16.

183. Weston, M. H.; Peterson, G. W.; Browe, M. A.; Jones, P.; Farha, O. K.; Hupp, J. T.; Nguyen, S. T., *Chem. Commun.* **2013,** *49*, 2995-2997.

184. Sanchez, C.; Arribart, H.; Giraud Guille, M. M., *Nat. Mater.* **2005,** *4*, 277-288.

185. Aizenberg, J.; Fratzl, P., *Adv. Mater.* **2009,** *21*, 387-388.

186. McInerney, J. O.; Cotton, J. A.; Pisani, D., *Trends Ecol. Evol.* **2008,** *23*, 276-281.

187. Zhang, M.; Gu, Z.-Y.; Bosch, M.; Perry, Z.; Zhou, H.-C., *Coord. Chem. Rev.* **2014**, doi: 10.1016/j.ccr.2014.05.031.

188. Rayner, J. H.; Powell, H. M., *J. Chem. Soc.* **1952**, 319-328.

189. Breslow, R.; Overman, L. E., *J. Am. Chem. Soc.* **1970,** *92*, 1075-1077.

190. Breslow, R., *Acc. Chem. Res.* **1980,** *13*, 170-177.

191. Luckarift, H. R.; Spain, J. C.; Naik, R. R.; Stone, M. O., *Nat. Biotech.* **2004,** *22*, 211-213.

192. Breslow, R.; Dong, S. D., *Chem. Rev.* **1998,** *98*, 1997-2012.

193. Breslow, R.; Yang, J.; Yan, J., *Tetrahedron* **2002,** *58*, 653-659.

194. Breslow, R.; Hammond, M.; Lauer, M., *J. Am. Chem. Soc.* **1980,** *102*, 421-422.

195. Wang, Q.; Yang, Z.; Zhang, X.; Xiao, X.; Chang, C. K.; Xu, B., *Angew. Chem. Int. Ed.* **2007,** *46*, 4285-4289.

196. Ye, H.; Tong, W.; D'Souza, V. T., *J. Am. Chem. Soc.* **1992,** *114*, 5470-5472.

197. Marinescu, L. G.; Bols, M., *Angew. Chem. Int. Ed.* **2006,** *45*, 4590-4593.

198. Breslow, R.; Huang, Y.; Zhang, X.; Yang, J., *Proc. Natl. Acad. Sci. U.S.A.* **1997,** *94*, 11156-11158.

199. D'Souza, V. T.; Bender, M. L., *Acc. Chem. Res.* **1987,** *20*, 146-152.

200. Ramsden, J. J., *Biosens. Bioelectron.* **1998,** *13*, 593-598.

201. Li, R.; Dowd, V.; Stewart, D. J.; Burton, S. J.; Lowe, C. R., *Nat. Biotech.* **1998,** *16*, 190-195.

202. Tang, Z.; Kotov, N. A.; Magonov, S.; Ozturk, B., *Nat. Mater.* **2003,** *2*, 413-418.

203. Kikuchi, M.; Ikoma, T.; Itoh, S.; Matsumoto, H. N.; Koyama, Y.; Takakuda, K.; Shinomiya, K.; Tanaka, J., *Compos. Sci. Technol.* **2004,** *64*, 819-825.

204. Daculsi, G., *Biomaterials* **1998,** *19*, 1473-1478.

205. Sopyan, I.; Mel, M.; Ramesh, S.; Khalid, K. A., *Sci. Tech. Adv. Mater.* **2007,** *8*, 116-123.

206. Stupp, S. I.; Ciegler, G. W., *J. Biomed. Mater. Res.* **1992,** *26*, 169-183.

207. Spoerke, E. D.; Anthony, S. G.; Stupp, S. I., *Adv. Mater.* **2009,** *21*, 425-430.

208. Mata, A.; Geng, Y.; Henrikson, K. J.; Aparicio, C.; Stock, S. R.; Satcher, R. L.; Stupp, S. I., *Biomaterials* **2010,** *31*, 6004-6012.

209. Rhee, S.-H.; Tanaka, J., *J. Am. Ceram. Soc.* **1998,** *81*, 3029-3031.

210. Hata, K.; Kokubo, T.; Nakamura, T.; Yamamuro, T., *J. Am. Ceram. Soc.* **1995,** *78*, 1049-1053.

211. Tanahashi, M.; Yao, T.; Kokubo, T.; Minoda, M.; Miyamoto, T.; Nakamura, T.; Yamamura, T., *J. Biomed. Mater. Res.* **1995,** *29*, 349-357.

212. Tampieri, A.; Celotti, G.; Landi, E., *Anal. Bioanal. Chem.* **2005,** *381*, 568-576.

213. Shikinami, Y.; Kotani, Y.; Cunningham, B. W.; Abumi, K.; Kaneda, K., *Adv. Funct. Mater.* **2004,** *14*, 1039-1046.

214. Landi, E.; Logroscino, G.; Proietti, L.; Tampieri, A.; Sandri, M.; Sprio, S., *J. Mater. Sci.: Mater. Med.* **2008,** *19*, 239-247.

215. Song, J.; Malathong, V.; Bertozzi, C. R., *J. Am. Chem. Soc.* **2005,** *127*, 3366-3372.

216. Costas, M.; Chen, K.; Que Jr, L., *Coord. Chem. Rev.* **2000,** *200-202*, 517-544.

217. Crabtree, R. H.; Loch, J. A.; Gruet, K.; Lee, D.-H.; Borgmann, C., *J. Organomet. Chem.* **2000,** *600*, 7-11.

218. Bedioui, F., *Coord. Chem. Rev.* **1995,** *144*, 39-68.

219. Bernadou, J.; Meunier, B., *Adv. Synth. Catal.* **2004,** *346*, 171-184.

220. Stevenson, J. D.; Thomas, N. R., *Nat. Prod. Rep.* **2000,** *17*, 535-577.

221. Kadokawa, J.-i.; Kokubo, A.; Tagaya, H., *Macromol. Biosci.* **2002,** *2*, 257-260.

222. Roth, K. M.; Zhou, Y.; Yang, W.; Morse, D. E., *J. Am. Chem. Soc.* **2004,** *127*, 325-330.

223. Yuan, Y.; Ji, H.; Chen, Y.; Han, Y.; Song, X.; She, Y.; Zhong, R., *Org. Process. Res. Dev.* **2004,** *8*, 418-420.

224. Mecke, A.; Dittrich, C.; Meier, W., *Soft Matter* **2006,** *2*, 751-759.

225. Kolusheva, S.; Kafri, R.; Katz, M.; Jelinek, R., *J. Am. Chem. Soc.* **2001,** *123*, 417-422.

226. Morigaki, K.; Baumgart, T.; Jonas, U.; Offenhausser, A.; Knoll, W., *Langmuir* **2002,** *18*, 4082-4089.

227. Rhee, S. H.; Tanaka, J., *J. Am. Ceram. Soc.* **1998,** *81*, 3029-3031.

228. Vaknin, D.; Krüger, P.; Lösche, M., *Phys. Rev. Lett.* **2003,** *90*, 178102.

229. Kolusheva, S.; Kafri, R.; Katz, M.; Jelinek, R., *J. Am. Chem. Soc.* **2000,** *123*, 417-422.

230. Mecke, A.; Dittrich, C.; Meier, W., *Soft. Matter.* **2006,** *2*, 751-759.

231. Nielsen, C., *Anal. Bioanal. Chem.* **2009,** *395*, 697-718.

232. Plant, A. L.; Gueguetchkeri, M.; Yap, W., *Biophys. J.* **1994,** *67*, 1126-1133.

233. Griffith, L. G.; Naughton, G., *Science* **2002,** *295*, 1009-1014.

234. Langer, R.; Vacanti, J. P., *Science* **1993,** *260*, 920-926.

235. Lee, K. Y.; Mooney, D. J., *Chem. Rev.* **2001,** *101*, 1869-1879.

236. Hollister, S. J., *Nat. Mater.* **2005,** *4*, 518-524.

237. Lutolf, M. P.; Hubbell, J. A., *Nat. Biotechnol.* **2005,** *23*, 47-55.

238. Drury, J. L.; Mooney, D. J., *Biomaterials* **2003,** *24*, 4337-4351.

239. Shin, H.; Jo, S.; Mikos, A. G., *Biomaterials.* **2003,** *24*, 4353-4364.

240. Ma, P. X., *Adv. Drug Deliver. Rev.* **2008,** *60*, 184-198.

241. Liao, S.; Chan, C. K.; Ramakrishna, S., *Mater. Sci. Eng. C* **2008,** *28*, 1189-1202.

242. Tang, Z. Y.; Wang, Y.; Podsiadlo, P.; Kotov, N. A., *Adv. Mater.* **2006,** *18*, 3203-3224.

243. Sivakova, S.; Rowan, S. J., *Chem. Soc. Rev.* **2005,** *34*, 9-21.

244. Patel, D. K.; Domínguez-Martín, A.; Brandi-Blanco, M. d. P.; Choquesillo-Lazarte, D.; Nurchi, V. M.; Niclós-Gutiérrez, J., *Coord. Chem. Rev.* **2012,** *256*, 193-211.

245. Elghanian, R.; Storhoff, J. J.; Mucic, R. C.; Letsinger, R. L.; Mirkin, C. A., *Science* **1997,** *277*, 1078-1081.

246. Giljohann, D. A.; Seferos, D. S.; Prigodich, A. E.; Patel, P. C.; Mirkin, C. A., *J. Am. Chem. Soc.* **2009,** *131*, 2072-2073.

247. Rosi, N. L.; Giljohann, D. A.; Thaxton, C. S.; Lytton-Jean, A. K. R.; Han, M. S.; Mirkin, C. A., *Science* **2006,** *312*, 1027-1030.

248. Taton, T. A.; Mirkin, C. A.; Letsinger, R. L., *Science* **2000,** *289*, 1757-1760.

249. Shan, Y.; Xu, J.-J.; Chen, H.-Y., *Chem. Commun.* **2009**, 905-907.

250. An, J.; Geib, S. J.; Rosi, N. L., *J. Am. Chem. Soc.* **2009,** *132*, 38-39.

251. Li, T.; Kozlowski, M. T.; Doud, E. A.; Blakely, M. N.; Rosi, N. L., *J. Am. Chem. Soc.* **2013,** *135*, 11688-11691.

252. Nugent, P. S.; Rhodus, V. L.; Pham, T.; Forrest, K.; Wojtas, L.; Space, B.; Zaworotko, M. J., *J. Am. Chem. Soc.* **2013,** *135*, 10950-10953.

253. Imaz, I.; Rubio-Martinez, M.; An, J.; Sole-Font, I.; Rosi, N. L.; Maspoch, D., *Chem. Commun.* **2011,** *47*, 7287-7302.

254. Sun, D.; Ma, S.; Ke, Y.; Petersen, T. M.; Zhou, H.-C., *Chem. Commun.* **2005**, 2663-2665.

255. Rochford, J.; Galoppini, E., *Langmuir* **2008,** *24*, 5366-5374.

256. Barrow, J. C.; Coburn, C. A.; Mcgaughey, G. B.; Nantermet, P. G.; Rajapakse, H. A.; Selnick, H. G.; Stauffer, S. R. 1,3,5-substituted phenyl derivative compounds useful as beta-secretase inhibitors for the treatment of alzheimer's disease. WO2005103020 (A1) Nov 3, **2005**.

257. An, J.; Geib, S. J.; Rosi, N. L., *J. Am. Chem. Soc.* **2010,** *132*, 38-39.

258. Ma, S.; Zhou, H.-C., *J. Am. Chem. Soc.* **2006,** *128*, 11734-11735.

259. Sun, D.; Ma, S.; Ke, Y.; Collins, D. J.; Zhou, H.-C., *J. Am. Chem. Soc.* **2006,** *128*, 3896-3897.

260. R. Thalladi, V.; Boese, R.; Brasselet, S.; Ledoux, I.; Zyss, J.; K. R. Jetti, R.; R. Desiraju, G., *Chem. Commun.* **1999**, 1639-1640.

261. Kikuchi, T.; Sato, S.; Fujita, M., *J. Am. Chem. Soc.* **2010,** *132*, 15930-15932.

262. Smaldone, R. A.; Forgan, R. S.; Furukawa, H.; Gassensmith, J. J.; Slawin, A. M. Z.; Yaghi, O. M.; Stoddart, J. F., *Angew. Chem. Int. Ed.* **2010,** *49*, 8630-8634.

263. Forgan, R. S.; Smaldone, R. A.; Gassensmith, J. J.; Furukawa, H.; Cordes, D. B.; Li, Q.; Wilmer, C. E.; Botros, Y. Y.; Snurr, R. Q.; Slawin, A. M. Z.; Stoddart, J. F., *J. Am. Chem. Soc.* **2012,** *134*, 406-417.

264. Breslow, R., *Acc. Chem. Res.* **1995,** *28*, 146-153.

265. Hupp, J. T., *Nat. Chem.* **2010,** *2*, 432-433.

266. Shultz, A. M.; Farha, O. K.; Hupp, J. T.; Nguyen, S. T., *J. Am. Chem. Soc.* **2009,** *131*, 4204-4205.

267. Pullen, S.; Fei, H.; Orthaber, A.; Cohen, S. M.; Ott, S., *J. Am. Chem. Soc.* **2013,** *135*, 16997-17003.

268. Chen, Y.; Lykourinou, V.; Hoang, T.; Ming, L.-J.; Ma, S., *Inorg. Chem.* **2012,** *51*, 9156-9158.

APPENDIX

CRYSTALLOGRAPHIC TABLES OF SELECTED STRUCTURES

Crystallographic Tables for PCN-501

PCN-501	
CCDC	to be submitted
Formula	$Zn_4C_{36}H_{20}O_{16}Si$
	Zn_4O_3(TCPS)(BDC)
M. w.	998.09
Crystal Shape	blocky
Crystal System	Orthorhombic
Space Group	*Pnma*
a (Å)	30.221(2)
b (Å)	17.0148(13)
c (Å)	18.5245(14)
α ( )	90.00
β ( )	90.00
γ ( )	90.00
V (Å^3)	9525.4(12)
Z	4
$d_{calcd.}$ (g/cm^3)	0.696
μ(mm^{-1})	1.037
F(000)	1992
θ_{max} [deg]	26.00
Completeness	100.0%
Collected reflections	97938
Unique reflections	9688
Parameters	220
Restraints	0
R_{int}	0.0588
*R*1 [I > 2σ(I)]	0.0683
*wR*2 [I > 2σ(I)]	0.1493
*R*1 (all data)	0.0911
*wR*2 (all data)	0.1559
GOF on F^2	1.004
$\Delta\rho_{max}/\Delta\rho_{min}$ [e·Å^{-3}]	1.628 / -0.974

Crystallographic Tables for PCN-502

PCN-502	
CCDC	to be submitted
Formula	$Zn_7C_{80}H_{69}N_3O_{29}Si_2$
	$Zn_7O_2(OH)_4(TCPS)_2(2,6\text{-}NDC)(DMA)_3$
M. w.	2050.15
Crystal Shape	blocky
Crystal System	Monoclinic
Space Group	$P2_1/m$
a (Å)	15.1552(15)
b (Å)	25.651(3)
c (Å)	17.7497(17)
α (°)	90.00
β (°)	96.9920(10)
γ (°)	90.00
V (Å^3)	6848.7(12)
Z	2
$d_{calcd.}$ (g/cm^3)	0.994
μ(mm^{-1})	1.273
F(000)	2080
θ_{max} [deg]	26.00
Completeness	99.9%
Collected reflections	73184
Unique reflections	13778
Parameters	534
Restraints	18
R_{int}	0.0460
$R1$ [I > 2σ(I)]	0.0634
$wR2$ [I > 2σ(I)]	0.1547
$R1$ (all data)	0.0756
$wR2$ (all data)	0.1601
GOF on F^2	1.003
$\Delta\rho_{max}/\Delta\rho_{min}$ [e·Å^{-3}]	3.342 / -2.130

Crystallographic Tables for PCN-503

PCN-503	
CCDC	to be submitted
Formula	$Zn_8C_{98}H_{56}O_{30}Si_3$
	$(Zn_4O)_2(TCPS)_3(4,4'\text{-BPDC})$
M. w.	2320.66
Crystal Shape	blocky
Crystal System	Monoclinic
Space Group	*C*2/*c*
a (Å)	49.885(6)
b (Å)	22.169(3)
c (Å)	23.134(3)
α ( )	90.00
β ( )	115.287(2)
γ ( )	90.00
V (Å^3)	23132(5)
Z	4
$d_{calcd.}$ (g/cm^3)	0.667
μ(mm^{-1})	0.864
F(000)	4664
θ_{max} [deg]	26.00
Completeness	100.0%
Collected reflections	118410
Unique reflections	22748
Parameters	591
Restraints	0
R_{int}	0.0660
*R*1 [I > 2σ(I)]	0.0391
*wR*2 [I > 2σ(I)]	0.1031
*R*1 (all data)	0.0707
*wR*2 (all data)	0.1079
GOF on F^2	1.004
$\Delta\rho_{max}/\Delta\rho_{min}$ [e·Å^{-3}]	0.865 / -0.675

Crystallographic Tables for PCN-504

PCN-504	
CCDC	to be submitted
Formula	$Zn_8C_{96}H_{56}O_{30}Si_3$
	$(Zn_4O)_2(TCPS)_3(BDA)$
M. w.	2296.64
Crystal Shape	blocky
Crystal System	Monoclinic
Space Group	*C*2/*c*
a (Å)	48.325(7)
b (Å)	22.682(3)
c (Å)	22.800(3)
α (°)	90.00
β (°)	114.083(2)
γ (°)	90.00
V (Å^3)	22816(5)
Z	4
$d_{calcd.}$ (g/cm^3)	0.669
μ(mm^{-1})	0.875
F(000)	4616
θ_{max} [deg]	26.00
Completeness	100.0%
Collected reflections	119380
Unique reflections	22433
Parameters	456
Restraints	21
R_{int}	0.0682
*R*1 [I > 2σ(I)]	0.0622
*wR*2 [I > 2σ(I)]	0.1383
*R*1 (all data)	0.1217
*wR*2 (all data)	0.1473
GOF on F^2	1.004
$\Delta\rho_{max}/\Delta\rho_{min}$ [e·Å^{-3}]	1.047 / -0.692

Crystallographic Tables for PCN-505

PCN-505	
CCDC	to be submitted
Formula	$Zn_4C_{40}H_{22}O_{15}Si$
	Zn_4O_3(TCPS)(1,4-NDC)
M. w.	1032.15
Crystal Shape	blocky
Crystal System	Orthorhombic
Space Group	*Pnma*
a (Å)	30.533(5)
b (Å)	17.059(3)
c (Å)	18.351(3)
α ( )	90.00
β ( )	90.00
γ ( )	90.00
V (Å^3)	9559(3)
Z	4
$d_{calcd.}$ (g/cm^3)	0.717
μ(mm^{-1})	1.034
F(000)	2064
θ_{max} [deg]	23.97
Completeness	99.4%
Collected reflections	83529
Unique reflections	7718
Parameters	280
Restraints	31
R_{int}	0.0579
*R*1 [I > 2σ(I)]	0.0633
*wR*2 [I > 2σ(I)]	0.1980
*R*1 (all data)	0.0839
*wR*2 (all data)	0.2034
GOF on F^2	1.004
$\Delta\rho_{max}/\Delta\rho_{min}$ [e·Å^{-3}]	0.965 / -0.369

Crystallographic Tables for PCN-506

PCN-506	
CCDC	to be submitted
Formula	$Zn_4C_{36}H_{18}NO_{15}Si$
	Zn_4O_3(TCPS)(2-NH_2-BDC)
M. w.	994.08
Crystal Shape	blocky
Crystal System	Orthorhombic
Space Group	*Pnma*
a (Å)	30.330(4)
b (Å)	16.992(2)
c (Å)	18.479(3)
α ( )	90.00
β ( )	90.00
γ ( )	90.00
V (Å^3)	9524(2)
Z	4
$d_{calcd.}$ (g/cm^3)	0.693
μ(mm^{-1})	1.037
F(000)	1980
θ_{max} [deg]	22.73
Completeness	99.8%
Collected reflections	74083
Unique reflections	6657
Parameters	186
Restraints	25
R_{int}	0.0992
*R*1 [I > 2σ(I)]	0.0552
*wR*2 [I > 2σ(I)]	0.1136
*R*1 (all data)	0.0937
*wR*2 (all data)	0.1218
GOF on F^2	1.006
$\Delta\rho_{max}/\Delta\rho_{min}$ [e·Å^{-3}]	0.668 / -0.543

Crystallographic Tables for PCN-511

PCN-511	
CCDC	942372
Formula	$Zn_3C_{56}H_{34}O_{16}Si_2$
	$Zn_3(HTCPS)_2$
M. w.	1215.12
Crystal Shape	Blocky
Crystal System	Monoclinic
Space Group	*C*2/*c*
a (Å)	25.622(2)
b (Å)	13.844(1)
c (Å)	25.612(4)
α ( )	90.000
β ( )	116.582(1)
γ ( )	90.000
V (Å^3)	8124.7(16)
Z	4
$d_{calcd.}$ (g/cm^3)	0.993
μ(mm^{-1})	0.954
F(000)	2464
θ_{max} [deg]	26.00
Completeness	100.0%
Collected reflections	42016
Unique reflections	7982
Parameters	380
Restraints	20
R_{int}	0.0366
*R*1 [I > 2σ(I)]	0.0536
*wR*2 [I > 2σ(I)]	0.1259
*R*1 (all data)	0.0595
*wR*2 (all data)	0.1282
GOF on F^2	1.006
$\Delta\rho_{max}/\Delta\rho_{min}$ [e·Å^{-3}]	1.999 / -2.008

Crystallographic Tables for PCN-513

PCN-513	
CCDC	942373
Formula	$Zn_5C_{82}H_{84}N_6O_{24}Si_2$
	$Zn_5(OH)_2(TCPS)_2(NMP)_4(DMF)_2$
M. w.	1920.58
Crystal Shape	Blocky
Crystal System	Triclinic
Space Group	$P\bar{1}$
a (Å)	13.935(2)
b (Å)	14.196(3)
c (Å)	14.671(2)
α (°)	107.988(2)
β (°)	113.735(1)
γ (°)	100.298(2)
V (Å^3)	2368.9(6)
Z	1
$d_{calcd.}$ (g/cm^3)	1.346
μ(mm^{-1})	1.343
F(000)	988
θ_{max} [deg]	26.00
Completeness	99.5%
Collected reflections	24912
Unique reflections	9284
Parameters	470
Restraints	26
R_{int}	0.0481
*R*1 [I > 2σ(I)]	0.0777
*wR*2 [I > 2σ(I)]	0.2562
*R*1 (all data)	0.0963
*wR*2 (all data)	0.2693
GOF on F^2	1.000
$\Delta\rho_{max}/\Delta\rho_{min}$ [e·Å^{-3}]	2.606 / -1.566

Crystallographic Tables for PCN-514·DMA·NMP

PCN-514·DMA·NMP	
CCDC	942374
Formula	$Cd_4C_{82}H_{90}N_6O_{24}Si_2$ $[Cd_3(TCPS)_2][Cd(NMP)_2(DMA)_2(H_2O)_2](DMA)_2$
M. w.	2049.38
Crystal Shape	Blocky
Crystal System	Triclinic
Space Group	$P\bar{1}$
a (Å)	13.982(2)
b (Å)	14.182(2)
c (Å)	14.270(3)
α (°)	115.922(2)
β (°)	113.196(2)
γ (°)	97.144(1)
V (Å^3)	2183.5(7)
Z	1
$d_{calcd.}$ (g/cm^3)	1.559
μ(mm^{-1})	1.064
F(000)	1036
θ_{max} [deg]	26.00
Completeness	99.5%
Collected reflections	22910
Unique reflections	8546
Parameters	542
Restraints	8
R_{int}	0.0186
$R1$ [I > 2σ(I)]	0.0326
$wR2$ [I > 2σ(I)]	0.0805
$R1$ (all data)	0.0340
$wR2$ (all data)	0.0813
GOF on F^2	1.007
$\Delta\rho_{max}/\Delta\rho_{min}$ [e·Å^{-3}]	3.133 / -2.367

Crystallographic Tables for PCN-514·DMF

PCN-514·DMF	
CCDC	942375
Formula	$Cd_4C_{80}H_{88}N_8O_{24}Si_2$
	$[Cd_3(TCPS)_2][Cd(DMF)_6](DMF)_2$
M. w.	2051.36
Crystal Shape	Blocky
Crystal System	Triclinic
Space Group	$P\bar{1}$
a (Å)	13.875(7)
b (Å)	14.072(7)
c (Å)	14.208(7)
α (°)	116.300(5)
β (°)	109.724(5)
γ (°)	101.428(5)
V (Å^3)	2133.1(18)
Z	1
$d_{calcd.}$ (g/cm^3)	1.597
μ(mm^{-1})	1.090
F(000)	1036
θ_{max} [deg]	27.00
Completeness	98.7 %
Collected reflections	23787
Unique reflections	9199
Parameters	459
Restraints	0
R_{int}	0.0246
$R1$ [I > 2σ(I)]	0.0491
$wR2$ [I > 2σ(I)]	0.1170
$R1$ (all data)	0.0549
$wR2$ (all data)	0.1213
GOF on F^2	1.001
$\Delta\rho_{max}/\Delta\rho_{min}$ [e·Å^{-3}]	2.280 / -2.316

Crystallographic Tables for PCN-515

PCN-515	
CCDC	942376
Formula	$Zn_9C_{112}H_{66}O_{39}Si_4$
	Zn_4O_2 Zn_3O_4 $Zn_2O(TCPS)_2(HTCPS)_2$
M. w.	2736.34
Crystal Shape	Blocky
Crystal System	Monoclinic
Space Group	$P2_1/c$
a (Å)	38.22(2)
b (Å)	29.788(19)
c (Å)	25.377(16)
α (°)	90.000
β (°)	99.005(8)
γ (°)	90.000
V (Å^3)	28536(30)
Z	4
$d_{calcd.}$ (g/cm^3)	0.637
μ(mm^{-1})	0.793
F(000)	5504
θ_{max} [deg]	28.56
Completeness	99.0%
Collected reflections	346308
Unique reflections	72070
Parameters	613
Restraints	17
R_{int}	0.1245
$R1$ [I > 2σ(I)]	0.0803
$wR2$ [I > 2σ(I)]	0.1782
$R1$ (all data)	0.2487
$wR2$ (all data)	0.1895
GOF on F^2	1.001
$\Delta\rho_{max}/\Delta\rho_{min}$ [e·Å^{-3}]	1.125 / -0.924

Crystallographic Tables for PCN-516

PCN-516	
CCDC	942377
Formula	$Zn_2C_{28}H_{16}O_{10}Si$
	Zn_2O_2(TCPS)
M. w.	671.24
Crystal Shape	Columnar
Crystal System	Tetragonal
Space Group	$P4_2/mmc$
a (Å)	12.706(4)
b (Å)	12.706(4)
c (Å)	23.817(8)
α (°)	90.000
β (°)	90.000
γ (°)	90.000
V (Å^3)	3845(2)
Z	2
$d_{calcd.}$ (g/cm^3)	0.580
μ(mm^{-1})	0.660
F(000)	676
θ_{max} [deg]	28.26
Completeness	99.8%
Collected reflections	43156
Unique reflections	2645
Parameters	56
Restraints	0
R_{int}	0.0719
$R1$ [I > 2σ(I)]	0.0537
$wR2$ [I > 2σ(I)]	0.1166
$R1$ (all data)	0.1014
$wR2$ (all data)	0.1270
GOF on F^2	1.008
$\Delta\rho_{max}/\Delta\rho_{min}$ [e·Å^{-3}]	0.410 / -0.282

Crystallographic Tables for PCN-517

PCN-517	
CCDC	942378
Formula	$Cd_4C_{56}H_{32}O_{20}Si_2$
	$[Cd_3(TCPS)_2][CdO_4]$
M. w.	1530.60
Crystal Shape	Blocky
Crystal System	Triclinic
Space Group	$P\bar{1}$
a (Å)	13.775(4)
b (Å)	14.507(4)
c (Å)	24.244(7)
α (°)	83.217(3)
β (°)	81.797(3)
γ (°)	65.572(3)
V (Å^3)	4357(2)
Z	2
$d_{calcd.}$ (g/cm^3)	1.167
μ(mm^{-1})	1.040
F(000)	1496
θ_{max} [deg]	26.00
Completeness	99.5%
Collected reflections	45816
Unique reflections	17024
Parameters	480
Restraints	154
R_{int}	0.0405
$R1$ [I > 2σ(I)]	0.1254
$wR2$ [I > 2σ(I)]	0.2771
$R1$ (all data)	0.1520
$wR2$ (all data)	0.2893
GOF on F^2	1.008
$\Delta\rho_{max}/\Delta\rho_{min}$ [e·Å^{-3}]	2.433 / -3.848

Crystallographic Tables for PCN-521

PCN-521	
CCDC	956577
Formula	$Zr_6C_{106}H_{64}O_{32}$
	Zr_6O_{16} $(MTBC)_2$
M. w.	2396.89
Crystal Shape	Distorted Octahedron
Crystal System	Tetragonal
Space Group	*I*4/*m*
a (Å)	19.936(4)
b (Å)	19.936(4)
c (Å)	42.251(8)
α ( )	90.00
β ( )	90.00
γ ( )	90.00
V (Å^3)	16792(6)
Z	2
$d_{calcd.}$ (g/cm^3)	0.474
μ(mm^{-1})	0.204
F(000)	2392
θ_{max} [deg]	26.00
Completeness	99.9%
Collected reflections	87257
Unique reflections	8387
Parameters	70
Restraints	4
R_{int}	0.1048
*R*1 [I > 2σ(I)]	0.1002
*wR*2 [I > 2σ(I)]	0.2282
*R*1 (all data)	0.2058
*wR*2 (all data)	0.2489
GOF on F^2	1.003
$\Delta\rho_{max}/\Delta\rho_{min}$ [e·Å^{-3}]	0.788 / -0.759

Crystallographic Tables for PCN-523

PCN-523	
CCDC	956576
Formula	$Hf_6C_{106}H_{64}O_{32}$
	Hf_6O_{16} $(MTBC)_2$
M. w.	2920.51
Crystal Shape	Distorted Octahedron
Crystal System	Tetragonal
Space Group	*I*4/*m*
a (Å)	21.04(2)
b (Å)	21.04(2)
c (Å)	40.18(4)
α ( )	90.00
β ( )	90.00
γ ( )	90.00
V ($Å^3$)	17784(31)
Z	2
$d_{calcd.}$ (g/cm^3)	0.545
μ(mm^{-1})	1.767
F(000)	2776
θ_{max} [deg]	26.00
Completeness	100.0%
Collected reflections	94860
Unique reflections	8873
Parameters	121
Restraints	33
R_{int}	0.0705
*R*1 [$I > 2\sigma(I)$]	0.0777
*wR*2 [$I > 2\sigma(I)$]	0.1692
*R*1 (all data)	0.0904
*wR*2 (all data)	0.1740
GOF on F^2	1.004
$\Delta\rho_{max}/\Delta\rho_{min}$ [$e \cdot Å^{-3}$]	1.122 / -3.119

Crystallographic Tables for PCN-530

PCN-530	
CCDC	962335
Formula	$C_{129}H_{79}N_{43}O_{28}Zn_9$
	$Zn_9O_3(Adenine)_6(TATB)_4(DMF)$
M. w.	3267.68
Crystal Shape	Blocky
Crystal System	Triclinic
Space Group	*P*$\bar{1}$
a (Å)	19.801(7)
b (Å)	20.162(7)
c (Å)	27.225(9)
α (°)	97.544(5)
β (°)	100.609(5)
γ (°)	111.627(5)
V (Å^3)	9692(6)Å^3
Z	2
$d_{calcd.}$ (g/cm^3)	1.120
μ(mm^{-1})	1.156
F(000)	3296
θ_{max} [deg]	22.62
Completeness	0.991
Collected reflections	56718
Unique reflections	25509
Parameters	1882
Restraints	0
R_{int}	0.0615
*R*1 [I > 2σ(I)]	0.0492
*wR*2 [I > 2σ(I)]	0.1221
*R*1 (all data)	0.0836
*wR*2 (all data)	0.1321
GOF on F^2	1.003
$\Delta\rho_{max}/\Delta\rho_{min}$ [e·Å^{-3}]	1.44/-0.44

Crystallographic Tables for TMOP-1

TMOP-1	
CCDC	962336
Formula	$C_{184}H_{156}N_{28}O_{84}Cu_{12}$ $Cu_{24}(MDPI)_{24}(DMA)_4(H_2O)_{20}$
M. w.	4865.85
Crystal Shape	Blocky
Crystal System	Triclinic
Space Group	$P\bar{1}$
a (Å)	27.990(3)
b (Å)	28.102(3)
c (Å)	28.303(5)
α (°)	109.319(2)
β (°)	106.426(2)
γ (°)	107.182(1)
V (Å^3)	18196(4)
Z	2
$d_{calcd.}$ (g/cm^3)	0.888
μ(mm^{-1})	0.744
F(000)	4952
θ_{max} [deg]	26.00
Completeness	0.995
Collected reflections	190892
Unique reflections	71236
Parameters	2158
Restraints	171
R_{int}	0.0761
$R1$ [I > 2σ(I)]	0.1014
$wR2$ [I > 2σ(I)]	0.2622
$R1$ (all data)	0.1691
$wR2$ (all data)	0.2841
GOF on F^2	1.006
$\Delta\rho_{max}/\Delta\rho_{min}$ [e·Å^{-3}]	2.22/-1.62